AD-A253 437

DTIC
ELECTE
JUL 2 4 1992

Final Report

DEFORMATION AND DAMAGE MECHANISMS
IN HIGH TEMPERATURE COMPOSITES
WITH DUCTILE MATRICES

by

George J. Dvorak and Yehia A. Bahei–El–Din

Department of Civil and Environmental Engineering
and
Center for Composite Materials and Structures
Rensselaer Polytechnic Institute
Troy, New York 12180–3590

Submitted to

June 1992

92-19911

92 7 2 059

REPORT DOCUMENTATION PAGE

Public reporting burden for this collection of information is estimated to average 1 hour per response, including the time for reviewing instructions, searching existing data sources, gathering and maintaining the data needed, and completing and reviewing the collection of information. Send comments regarding this burden estimate or any other aspect of this collection of information, including suggestions for reducing this burden, to Washington Headquarters Services, Directorate for Information Operations and Reports, 1215 Jefferson Davis Highway, Suite 1204, Arlington, VA 22202-4302, and to the Office of Management and Budget, Paperwork Reduction Project (0704-0188), Washington, DC 20503.

1. AGENCY USE ONLY (Leave blank)	2. REPORT DATE	3. REPORT TYPE AND DATES COVERED FINAL

4. TITLE AND SUBTITLE	5. FUNDING NUMBERS
Deformation and Damage Mechanisms in High Temperature Composites with Ductile Matrices (u)	C - AFOSR-88-0150

6. AUTHOR(S)

George J. Dvorak and Yehia A. Bahei-El-Din

7. PERFORMING ORGANIZATION NAME(S) AND ADDRESS(ES)	8. PERFORMING ORGANIZATION REPORT NUMBER
Department of Civil and Environmental Engineering and Center for Composite Materials and Structures Rensselaer Polytechnic Institute Troy, New York 12180-3590 AFOSR-TR-	2 0674

9. SPONSORING/MONITORING AGENCY NAME(S) AND ADDRESS(ES)	10. SPONSORING/MONITORING AGENCY REPORT NUMBER
Dr. Walter Jones Air Force Office of Scientific Research Bolling Air Force Base, Washington DC 20332 NA	

11. SUPPLEMENTARY NOTES

12a. DISTRIBUTION/AVAILABILITY STATEMENT	12b. DISTRIBUTION CODE
Approved for public release. Distribution unlimited.	

13. ABSTRACT (Maximum 200 words)

This resport presents a summary of the theoretical and experimental work performed in our research program on deformation and damage of high temperature composites. The theoretical part focused on two areas; modeling of fatigue damage in metal matrix composite and laminates by shakedown and nonlinear optimization, and refinement of the unified viscoplasticity theory formulated last year for homogeneous materials, in order to model certain phenomena observed in high temperature experiments of unreinforced metals. Implementation of the new viscoplasticity theory for the phases in the Periodic Hexagonal Array model for unidirectional composites was an important part of the research. Progress in these theoretical aspects of the program is summarized. The report also describes achievements in the experimental program.

14. SUBJECT TERMS		15. NUMBER OF PAGES
Composite materials, damage accumulation, viscoplasticity theory		57
		16. PRICE CODE

17. SECURITY CLASSIFICATION OF REPORT	18. SECURITY CLASSIFICATION OF THIS PAGE	19. SECURITY CLASSIFICATION OF ABSTRACT	20. LIMITATION OF ABSTRACT
Unclassified	Unclassified	Unclassified	SAR

GENERAL INSTRUCTIONS FOR COMPLETING SF 298

The Report Documentation Page (RDP) is used in announcing and cataloging reports. It is important that this information be consistent with the rest of the report, particularly the cover and title page. Instructions for filling in each block of the form follow. It is important to *stay within the lines* to meet *optical scanning requirements.*

Block 1. Agency Use Only (Leave blank).

Block 2. Report Date. Full publication date including day, month, and year, if available (e.g. 1 Jan 88). Must cite at least the year.

Block 3. Type of Report and Dates Covered. State whether report is interim, final, etc. If applicable, enter inclusive report dates (e.g. 10 Jun 87 - 30 Jun 88).

Block 4. Title and Subtitle. A title is taken from the part of the report that provides the most meaningful and complete information. When a report is prepared in more than one volume, repeat the primary title, add volume number, and include subtitle for the specific volume. On classified documents enter the title classification in parentheses.

Block 5. Funding Numbers. To include contract and grant numbers; may include program element number(s), project number(s), task number(s), and work unit number(s). Use the following labels:

C	- Contract	PR	- Project
G	- Grant	TA	- Task
PE	- Program Element	WU	- Work Unit Accession No.

Block 6. Author(s). Name(s) of person(s) responsible for writing the report, performing the research, or credited with the content of the report. If editor or compiler, this should follow the name(s).

Block 7. Performing Organization Name(s) and Address(es). Self-explanatory.

Block 8. Performing Organization Report Number. Enter the unique alphanumeric report number(s) assigned by the organization performing the report.

Block 9. Sponsoring/Monitoring Agency Name(s) and Address(es). Self-explanatory.

Block 10. Sponsoring/Monitoring Agency Report Number. *(If known)*

Block 11. Supplementary Notes. Enter information not included elsewhere such as: Prepared in cooperation with...; Trans. of...; To be published in.... When a report is revised, include a statement whether the new report supersedes or supplements the older report.

Block 12a. Distribution/Availability Statement. Denotes public availability or limitations. Cite any availability to the public. Enter additional limitations or special markings in all capitals (e.g. NOFORN, REL, ITAR).

DOD - See DoDD 5230.24, "Distribution Statements on Technical Documents."
DOE - See authorities.
NASA - See Handbook NHB 2200.2.
NTIS - Leave blank.

Block 12b. Distribution Code.

DOD - Leave blank.
DOE - Enter DOE distribution categories from the Standard Distribution for Unclassified Scientific and Technical Reports.
NASA - Leave blank.
NTIS - Leave blank.

Block 13. Abstract. Include a brief *(Maximum 200 words)* factual summary of the most significant information contained in the report.

Block 14. Subject Terms. Keywords or phrases identifying major subjects in the report.

Block 15. Number of Pages. Enter the total number of pages.

Block 16. Price Code. Enter appropriate price code *(NTIS only).*

Blocks 17. - 19. Security Classifications. Self-explanatory. Enter U.S. Security Classification in accordance with U.S. Security Regulations (i.e., UNCLASSIFIED). If form contains classified information, stamp classification on the top and bottom of the page.

Block 20. Limitation of Abstract. This block must be completed to assign a limitation to the abstract. Enter either UL (unlimited) or SAR (same as report). An entry in this block is necessary if the abstract is to be limited. If blank, the abstract is assumed to be unlimited.

TABLE OF CONTENTS

ii

ABSTRACT

This report presents a summary of the theoretical and experimental work performed in our research program on deformation and damage of high temperature composites. The theoretical part focused on two areas; modeling of fatigue damage in metal matrix composite and laminates by shakedown and nonlinear optimization, and refinement of the unified viscoplasticity theory formulated last year for homogeneous materials, in order to model certain phenomena observed in high temperature experiments of unreinforced metals. Implementation of the new viscoplasticity theory for the phase sin the Periodic Hexagonal Array model for unidirectional composites was an important part of the research. Progress in these theoretical aspects of the program is summarized. The report also describes achievements in the experimental program.

1. INTRODUCTION

The main goal of this research is to understand and evaluate the deformation and damage mechanisms evolving in high temperature composites under thermomechanical service loads. The research program aims at examining a specific composite system with a ductile matrix which has the potential of providing a better material for jet engine parts and other high–temperature applications. In past progress reports, we described a new unified thermoviscoplasticity theory based on overstress for homogeneous materials to represent the matrix and fiber phases. This theory can be applied to the phases of any micromechanical model to obtain the local stresses and overall response of unidirectionally reinforced composites. A complete discussion of the theory is given by Shah (1991). Moreover, a new model for fatigue damage in metal matrix composites and laminates based on shakedown and nonlinear optimization has been developed. In parallel, our efforts concentrated on assembling the high–temperature facilities and procurement of the specimens in preparation for the experiments. The following major accomplishments were achieved:

- Development of a thermoviscoplasticity theory with time recovery effects for homogeneous materials.

- Implementation of the rate–dependent constitutive equations of the phases in the Periodic Hexagonal Array model and the ABAQUS finite element program.

- Modeling of fatigue damage in metal matrix composites and laminates with regard to experimental observations and a bimodal damage theory.

- Assembling the high temperature equipment.

- Fabrication of tubular samples of a fiber–reinforced superalloy composite.

A summary of these developments is presented in the sequel.

1

2. THEORETICAL WORK

2.1   Thermoviscoplasticity of Fibrous Composites

2.1.1 Micromechanical Models

Evaluation of overall properties of composite materials is best done with appropriate micromechanical models which can incorporate the inelastic constitutive relations that describe phase behavior, and which reflect the dominant deformation mechanisms in the microstructure. The selection of models which satisfy these requirements was motivated by our past experience with modeling of experimentally observed elastic–plastic behavior of fibrous B/Al composite systems (Dvorak et al., 1988, 1990). In particular, the periodic hexagonal array (PHA) model (Dvorak and Teply 1985, Teply and Dvorak, 1988), and the bimodal plasticity theory (Dvorak and Bahei–El–Din, 1987) were chosen and adapted for this purpose.

In the PHA model, the centers of the aligned fibers are assumed to be arranged in a periodic hexagonal array in the transverse plane. The circular cross sections of the fibers are approximated by $(6 \times n)$ polygonal cross sections, which tend to converge rapidly when the integer $n \geq 1$ increases. The hexagonal array is divided into identical unit cells. Appropriate periodic boundary conditions are prescribed for these cells such that the solution for a single cell can be used to generate the deformation field in a fibrous composite subjected to uniform overall strains or stresses, and to a uniform thermal change. Figure 1 illustrates the PHA model for two subdivisions of the unit cell. Coarser subdivisions are adequate if overall response alone is of interest, whereas more refined meshes are used in evaluation of local fields in the phases and at the fiber–matrix interface. Models of this kind have the ability to approximate the variable local fields, which determine many aspects of the overall response, and are therefore preferable to the models which rely on averages of local fields, such as the self–consistent or Mori–Tanaka

2

approximations. Typically, the solution is found with the ABAQUS finite element program. However, in the present research the problem was reformulated as described below, hence the solution can be now found in a more efficient manner, without inelastic finite element routines.

The bimodal plasticity theory was originally deduced, in part, from experimental observations of elastic–plastic behavior of unidirectional B/Al systems. More recently, it was applied to several high–temperature systems, and extended to accommodate viscoplastic behavior of the matrix phase (Hall 1989). The theory recognizes two distinct deformation modes, the fiber dominated (FDM) and the matrix–dominated (MDM) mode. In the fiber mode, the local fields in the composite are assumed to be approximately uniform, and the overall response is evaluated from an averaging model. In the matrix mode, the dominant mode of deformation is approximated by smooth shearing on planes parallel to the fiber axis. Each of the two modes has a separate branch of the overall yield surface, and is activated according to the current position of the loading vector. Figure 2 shows examples of the surfaces in the plane stress space. The size and shape of the MDM yield surface does not depend on fiber properties and volume fraction, but these parameters do affect the FDM surface. In systems reinforced with fibers of high longitudinal shear modulus, such as boron, silicon carbide, or tungsten, the FDM surface contains a large part of the MDM surface which in turn controls the onset of yielding, and subsequent plastic flow. In contrast, systems reinforced with carbon fibers of low shear modulus may have a FDM surface which lies entirely within the MDM branch. The matrix mode is not present in such systems, but the FDM model assumptions may no longer hold and the PHA model is again indicated.

2.1.2 Uniform Fields and Phase Eigenstrains in Heterogeneous Media

In a series of recent papers, Dvorak (1983, 1986, 1987, 1990a) examined the consequences of his discovery of the existence of uniform strain fields in heterogeneous media. The recent papers (1990, 1992a, 1992b), and a related review paper (Dvorak 1991), establish connections between mechanical and eigenstrain–induced local fields, and regard plastic strains as phase eigenstrains. A solution scheme for the PHA and FDM models was developed as a result of this investigation.

The new method may be summarized as follows. Consider a representative volume of the composite aggregate under uniform overall stress $\bar{\sigma}$ or strain $\bar{\epsilon}$, and a uniform thermal change $d\theta$. A subdivision of the RVE is made such that in each subelement $r = 1, 2,...N$, the actual local field is approximated by uniform stress, and the stress field in the entire domain becomes piecewise uniform. Some initial loading has taken place in the elastic and inelastic deformation ranges. Then, an increment of overall uniform strain $d\bar{\epsilon}$ or stress $d\bar{\sigma}$ is applied from the current state. The total strain increment $d\epsilon_r$ in each subelement is decomposed into elastic strains $A_r d\bar{\epsilon}$ caused by external loads, and total strains which incorporate the local (uniform) inelastic strains together with the elastic strains transmitted from all other subelements. The same decomposition is applied to the local stresses:

$$d\epsilon_r = A_r\, d\bar{\epsilon} + a_r\, d\theta + \sum_{s=1}^{N} D_{rs}\, d\epsilon_s^p \,, \tag{1}$$

$$d\sigma_r = B_r\, d\bar{\sigma} + b_r\, d\theta + \sum_{s=1}^{N} F_{rs}\, d\sigma_s^\lambda \,, \tag{2}$$

$$d\sigma_s^\lambda = L_s\, d\epsilon_s^p \,,$$

where A_r is strain concentration factor, a_r is thermal strain vector, and L_s is the elastic

stiffness. The tensors D_{rs} and F_{rs} are eigenstrain and eigenstress concentration factors which evaluate the average strain or stress in subelement r due to a single uniform unit eigenstrain or eigenstress in subelement s, while the composite is fully constrained but not otherwise loaded. This is combined with the phase constitutive equation, evaluated in each subelement at the current local stress. In particular, the total strain increment is additively decomposed, $d\epsilon_r = d\epsilon_r^e + d\epsilon_r^p$, and the inelastic part takes the form

$$d\epsilon_s^p = (\mathcal{M}_r - M_r)\, d\sigma_r + (\boldsymbol{m}_r - m_r)\, d\theta,$$

$$d\epsilon_s^p = G_r\, d\sigma_r + g_r\, d\theta,$$

(3)

where $\mathcal{M}$ denotes the instantaneous compliance, M the elastic compliance, $\boldsymbol{m}$ the instantaneous coefficient of thermal expansion, and m_r the elastic coefficient of thermal expansion. Local stresses in the subelements are then expressed as

$$d\sigma_r + \sum_{s=1}^{N} F_{rs}\, L_s\, (G_s\, d\sigma_s + g_r\, d\theta) = B_r\, d\overline{\sigma} + b_r\, d\theta.$$

(4)

This is a system of N equations for the unknown local stresses. Note that the transformation concentration factors are constant for a given RVE, and easily evaluated by elastic analysis. The solution of (4) can be readily utilized in evaluation of local and overall strains as follows:

$$d\epsilon_r = (M_r + G_r)\, d\sigma_r,$$

$$d\overline{\epsilon}_r = \sum_{s=1}^{N} c_r\, d\epsilon_r, \quad d\overline{\epsilon}^p = d\overline{\epsilon} - M\, d\overline{\sigma},$$

(5)

5

which gives the overall plastic strain increment under $d\bar{\sigma}$. Particularly simple forms of the above procedure follow for two–phase systems, which are of interest in implementations of the FDM model.

Additional applications of the uniform field concept have been made in development of general relations between mechanical and eigenstrain concentration factors, and of universal connections between overall and phase moduli, and also between coefficients of the concentration factors themselves (Dvorak 1990). Of particular interest in the present work is an exact analysis of the effect of thermal hardening in two–phase systems (Dvorak 1991).

2.1.3 Constitutive Equations of the Phases

To reflect the particular inelastic behavior of ductile high–temperature composites, it is necessary to introduce into the analysis the appropriate viscoplastic constitutive relations of the constituent phases. We assume the phases to be homogeneous, the matrix elastically isotropic, and the fiber transversely isotropic. Either phase may exhibit nonlinear response under thermomechanical loads which exceed the elastic limit of the material. In this case, however, the present theory requires the material to be elastically isotropic.

The total strain rate, $\dot{\epsilon}_{ij}$, is divided into elastic, thermal and inelastic components:

$$\dot{\epsilon}_{ij} = \dot{\epsilon}^e_{ij} + \dot{\epsilon}^t_{ij} + \dot{\epsilon}^p_{ij} .\tag{6}$$

Considering isotropic materials and assuming the thermoelastic properties to be temperature–dependent, the elastic and thermal strain rates are given by

$$\dot{\epsilon}^e_{ij} = M^e_{ijkl}(\theta)\,\dot{\sigma}_{kl} ,\tag{7}$$

6

$$\dot{\epsilon}^t_{ij} = [(d\ M^e_{ijkl}(\theta)/d\theta)\ \sigma_{kl} + m_{ij}(\theta)]\ \dot{\theta}\ , \tag{8}$$

$$m_{ij}(\theta) = \delta_{ij}\ \alpha^t(\theta)\ , \tag{9}$$

where θ is the current temperature, $M^e_{ijkl}(\theta)$ is the elastic compliance, and $\alpha^t(\theta)$ is the coefficient of thermal expansion.

The inelastic part of the strain is found with the help of a viscoplasticity theory which incorporates the isothermal formulation by Eisenberg and Yen (1981). Our research in the past year concentrated on modifying the theory to include thermal loads, temperature–dependent properties, and thermal time recovery. In what follows, we summarize the constitutive equations developed for rate–dependent deformation.

We assume the existence of an equilibrium yield surface which is the locus of all stress states that can be reached form the current state by purely elastic deformation. Inelastic deformation develops only when the stress point lies outside the equilibrium yield surface. In the presence of kinematic and isotropic hardening, a Mises form of the current equilibrium yield surface can be written as

$$f = \frac{1}{2}(s_{ij} - \alpha_{ij})(s_{ij} - \alpha_{ij}) - (Y + Q)^2/3 = 0\ , \tag{10}$$

where s_{ij} is the deviatoric stress, α_{ij} denotes the center of the yield surface, $Y = Y(\theta)$ is the yield stress in tension, which is independent of the loading rate, and Q is an isotropic hardening function. The latter can be written as a function of the accumulated inelastic strain as

$$Q = Q(\theta, \bar{\epsilon}^P) = Q_a(\theta)\ [1 - e^{-q(\theta)\ \bar{p}}]\ , \tag{11}$$

$$\bar{p} = \int_0^{\epsilon} d\bar{\epsilon}^P = \frac{2}{3}\int_0^{\epsilon} d\epsilon^P_{ij}\ d\epsilon^P_{ij};\ d\epsilon^P_{kk} = 0\ . \tag{12}$$

7

The functions $Q_a(\theta)$ and $q(\theta)$ are material parameters and $d\bar{\epsilon}^p$ is effective inelastic strain increment.

The equilibrium stress, $s^\dagger_{ij}$, which lies on the yield surface, is found from (10) as

$$s^\dagger_{ij} = \left[\frac{2[Y(\theta) + Q(\theta)]^2}{3(s_{kl} - \alpha_{kl})(s_{kl} - \alpha_{kl})}\right](s_{ij} - \alpha_{ij}) + \alpha_{ij} . \tag{13}$$

The effective overstress, R, is a measure of the distance between the actual stress point, s_{ij}, and the equilibrium stress point, $s^\dagger_{ij}$. It vanishes if the stress point lies on or inside the yield surface. In particular

$$R = [\tfrac{3}{2}(s_{ij} - s^\dagger_{ij})(s_{ij} - s^\dagger_{ij})]^{\frac{1}{2}} \qquad\qquad \text{if } f > 0 , \tag{14}$$

$$R = 0 \qquad\qquad\qquad\qquad\qquad\qquad\qquad \text{if } f \leq 0 . \tag{15}$$

The inelastic strain rate is assumed in the form of a power law of the overstress:

$$\dot{\epsilon}^{in}_{ij} = \sqrt{\tfrac{3}{2}}\, k(\theta)\, R^{p(\theta)}\, n_{ij}(s^\dagger_{ij}) , \tag{16}$$

where the functions $k(\theta)$ and $p(\theta)$ are assumed to be material parameters and n_{ij} is the unit normal to the equilibrium yield surface (10) at the current equilibrium stress point.

The rate of translation of the center of the yield surface, $\dot{\alpha}_{ij}$, is expressed as

$$\dot{\alpha}_{ij} = \sqrt{\tfrac{3}{2}}\, \frac{1}{n_{kl}\nu_{kl}}\left\{[H(\theta) - \partial Q/\partial\bar{\epsilon}^{in}]\, k(\theta)\, R^{p(\theta)} - \partial Q/\partial\theta\right\}\nu_{ij}$$
$$- c_r(\theta)\,\bar{\alpha}^{-m_r(\theta)}(\alpha_{ij}/\bar{\alpha}) , \tag{17}$$

$$\overline{\alpha} = (\alpha_{kl}\alpha_{kl})^{\frac{1}{2}} .$$ (18)

Here, $H(\theta)$ is the tangent modulus of the inelastic stress–strain curve, and ν_{ij} specifies the direction of translation of the yield surface in the absence of static time recovery. This recovery is given by the second term in (17) and may be active even when the material is elastic. It is caused by rearrangement of dislocations by climb and recrystallization from annealing and is more pronounced at high temperatures. The functions $c_r(\theta)$ and $m_r(\theta)$ are material parameters. Thermal recovery effects on the isotropic hardening rate $\dot{Q}$ (see eq. (11)) can be also considered in the model; Shah (1991). This is omitted here for brevity, we note, however, that description of this effect require four additional material parameters which may depend on temperature.

A bounding surface is used to establish the instantaneous tangent modulus H and to describe accurately the cyclic behavior of the material, Fig. 3. This surface is derived as an isotropic expansion of the equilibrium yield surface. During inelastic deformation, the bounding surface translates in the stress space and exhibits isotropic changes as well. Translation of the bounding surface is dictated by the requirement that the yield surface and the bounding surface have a common normal when they become in contact. Details of this kinematic hardening rule are given by Dafalias and Popov (1976). In analogy with the equilibrium yield surface, thermal time recovery of isotropic as well as kinematic hardening of the bounding surface can be included in the model.

The instantaneous tangent modulus, H, is found as a function of the distance, δ, between the equilibrium stress, s^*_{ij}, and a corresponding point on the bounding surface, $\overline{s}_{ij}$, with unit normal $\overline{n}_{ij}(\overline{s}_{ij}) = n_{ij}(s^*_{ij})$:

$$H(\theta) = H_0(\theta) + h(\theta)\left[\delta/(\delta_{in} - \delta)\right] ,$$ (19)

$$\delta = \left[\frac{3}{2}(\bar{s}_{ij} - s^{t}_{ij})(\bar{s}_{ij} - s^{t}_{ij})\right]^{\frac{1}{2}}. \tag{20}$$

The parameters $H_0(\theta)$ and $h(\theta)$ need to be determined experimentally.

2.1.4 Comparison with Experiments

The preceding theory was used to computed the response of unreinforced Ti–15–3 under uniaxial tension which was tested by Tuttle, Rogacki and Johnson (1990). The tests were conducted at room temperature, 482°C, and 649°C. At each temperature, two tension tests were performed, one under stress–controlled loading at stress rate of 2.6 MPa/s, the other under strain–controlled loading at strain rate of 10^{-4}/s. The strain–controlled test consisted of a number of loading and relaxation periods. The objective of this test was to determine the inelastic equilibrium stress–strain curve.

The parameters of the model found by matching the stress–controlled experiments and the equilibrium response are shown in Table 1. The parameters with top bar correspond to the bounding surface and have the same meaning of their yield surface counterparts. For example, $\overline{Y}$ is the 'radius' of the bounding surface, and $\overline{Q}_a$, $\bar{q}$ are material parameters related to the bounding surface isotropic hardening function $\overline{Q}$ which is similar in form to the yield surface isotropic hardening function Q given in eq. (11).

The measured and computed responses are shown in Figs. 4–6 for the stress–controlled tests and Figs. 7–9 for the strain–controlled tests. The agreement is remarkably satisfactory. In particular, the theory replicates the descending portions of the stress–strain curves under strain–controlled loading when the specimen is reloaded following each relaxation period, Figs. 7–9.

2.1.5 Rate Dependent Analysis of Metal Matrix Composite Systems

The elastic deformation region of fibrous composites with metallic matrices is reduced considerably at high temperatures. The individual phases, and hence the composite aggregate become sensitive to the rate at which the overall temperature or mechanical loads are applied and to other time dependent processes. Under sustained loads, the response of these materials is also time dependent.

The local fields arising in the composite during thermomechanical loading are highly nonuniform. As a result, stress and strain rates may vary from point to point in the material, with the steepest gradients occurring at the interface between the fiber and the matrix. These nonuniformities and gradients in local stress rates affect the overall loading of the composite, those regions with very high stress or strain rates remain stiff as a result of the dependence of instantaneous properties on the loading rates. This may cause even higher stress concentrations in these areas, which are usually close to the interface of the fiber and matrix, and may result in debonding or matrix cracking. Again, during overall relaxation or creep, high inelastic strain rates will exist in the same regions due to effect of prior loading history. This results in a redistribution of stresses within the phases which is then bound to have an effect on the subsequent overall behavior.

All these aspects of high temperature deformation of metal matrix composites must be considered in structural analysis. The only recourse in this case is the use of micromechanics and in particular those models which assume nonuniform or at most piecewise uniform local fields. The response of silicon carbide–titanium 15–3 unidirectional composites, at high temperatures, was analyzed using the periodic hexagonal array (PHA) model outlined in Fig. 1. The thermoviscoplastic constitutive theory for the deformation of the matrix phase recovery developed and tested in §2.1.3, was extended by Shah (1991) to include thermal time. The temperature dependent material properties required for the theory were evaluated in *op. cit.* from experiments on unreinforced titanium 15–3.

The thermoviscoplastic constitutive equations were implemented in a subroutine to be interfaced with the ABAQUS finite element code. The purpose of this subroutine was to compute the material stiffness and stress increment for a given strain increment. The purpose was to compute the material stiffness and stress increment for a given strain increment. The subroutine would be called by the ABAQUS main program at each integration point in the finite element mesh and for every loading increment. The actual assembling of element stiffnesses, computation of displacements from the applied nodal forces and conversion of these into strain increments was performed by the ABAQUS program. Integration of the overall solution was performed in the main program using the Newton–Raphson method.

The following information is provided to ABAQUS via UMAT at each material integration point: Given the stress, total elapsed time, strain increment, time interval in which the strain increment is applied, temperature at the start of the increment, temperature increment, and all user defined solution dependent variables at the start of the increment, the UMAT subroutine must return the stress, and the instantaneous stiffness at the end of the increment as well as update all solution dependent variables. Solution dependent variables are those which change with time and affect the computations in the next increment. Examples are the location and size of the yield and bounding surfaces and the accumulated inelastic strain.

A flowchart of the overall iteration scheme of ABAQUS is provided in Fig. 10, and the corresponding overall stress–strain diagram of the Newton–Raphson procedure is shown in Fig. 11. The steps involved in the entire procedure for computing the overall response are outlined below:

Step 1: Input material properties, one set at each temperature, mechanical and thermal loading history, initial temperature, initial time step for global integration and initial time step for local integration.

<u>Step 2</u>: At the start of a global time increment ABAQUS passes a zero strain increment to UMAT, with all current solution dependent variables and current stress. UMAT computes the instantaneous stiffness at the current temperature and returns it to ABAQUS.

<u>Step 3</u>: ABAQUS assembles the global stiffness matrix and solves for the unknown nodal displacements, Δu_k, due to the loads applied in that increment. The strain increments at integration points, $\Delta \epsilon_{ij}^r$, are computed from the displacements using the element shape functions, and passed into UMAT together with the current solution dependent variables and current stress.

<u>Step 4</u>: UMAT calculates the strain rate from the strain increment and time step. It then integrates the constitutive equations based on this strain rate. The stress increment is found by integrating $\dot{\sigma}_{ij} = L_{ijkl}^e(\dot{\epsilon}_{kl} - \dot{\epsilon}_{kl}^{in} - \dot{\epsilon}_{kl}^t)$. The solution dependent variables are updated and the instantaneous stiffness is computed and returned to ABAQUS.

<u>Step 5</u>: ABAQUS computes the off–balance or residual forces, $\Delta \hat{F}_k$, from the stresses returned by UMAT. The global stiffness is reassembled with the instantaneous local stiffnesses supplied by UMAT. Displacement, and hence strain increments are computed from the residual loads. These are added to the strain increment in Step 3, Fig. 11, and returned to UMAT with the solution dependent variables and total stress that were current at beginning of Step 3.

<u>Step 6</u>: Step 4 and 5 are repeated until the off–balance forces are less than predefined tolerance, TOL^G, which is set by the user. If the tolerance is not met, the strain increments computed in Step 5 are added to those computed previously in the same time

increment. If the tolerance is met, all variables are updated and Steps 2 through 6 are repeated for the next time increment.

Two numerical integration schemes for systems of first order ordinary differential equations of the form $\dot{y}_i = f(y_1,...y_n,t)$, were used in Step 4 above. One was the explicit fourth order Rung–Kutta–Fehlberg scheme (Burden and Faires, 1985). The other was a predictor–corrector method for stiff ODEs (Kumar, et al, 1980). A one step Euler method was used as the predictor and the two step Adam–Bashforth method as the corrector. Both integration schemes showed no instabilities and provided comparable accuracy on the overall solution. The fourth order method required six function evaluations per step, compared to two required for the corrector–predictor scheme. However, the former allowed for larger time steps for the same accuracy. Yet, in most cases solution time using the latter was 20–30 percent less.

Figure 12 shows a flow chart for the computations performed by UMAT. The steps involved are briefly explained below.

Step 1: ABAQUS passes to UMAT the increments of strain, temperature and time, the current values of stress and other solution dependent variable and the initial time step for local integration. From this information the strain rate is calculated. If the strain rate is zero the current instantaneous stiffness is returned, this indicates the beginning of a step. If the strain rate is non–zero then UMAT proceeds to perform the numerical integration.

Step 2: The yield condition is checked, if it is not violated then an elastic analysis is performed, Step 3, otherwise the inelastic equations are integrated Step 4.

Step 3: Elastic analysis. The new stress and other solution dependent variables are computed, the time step, Δt, is increased, and all variables updated. Step 2 is repeated

14

until the entire time increment, ΔT, is covered.

Step 4: Inelastic analysis. Computation of the overstress, unit normal, equilibrium stress, plastic tangent modulus, inelastic strain rate, stress rate, translation rates of the yield and bounding surfaces and the rate of isotropic hardening is performed in this order.

For the Runge–Kutta–Fehlberg method the local truncation error, in the effective inelastic strain rate is divided by the effective inelastic strain rate and compared against a present tolerance,

$$e = \frac{\text{l.t.e } \dot{\bar{\epsilon}}^{in}}{\dot{\bar{\epsilon}}^{in}} \leq \text{ TOL} .$$

In the case of the predictor–corrector scheme the error is defined as

$$e = \frac{|\dot{\bar{\epsilon}}^{in}_{corrector} - \dot{\bar{\epsilon}}^{in}_{predictor}|}{|\dot{\bar{\epsilon}}^{in}_{corrector}|} \leq \text{ TOL} .$$

If the tolerance is met the variables are updated and the time step increased. Step 2 is then repeated till the entire time increment is covered. If the error is larger than the tolerance, the time step is suitably reduced and Step 4 is repeated.

Step 5: At the end of the time increment, ΔT, the instantaneous stiffness is computed and returned to ABAQUS with the updated stress and solution dependent variable.

A description and listing of the UMAT subroutine which implements the above algorithm is presented in Shah (1991).

15

2.1.6 Numerical and Experimental Results

The periodic array finite element model, together with the thermoviscoplastic constitutive equations, were used to predict the rate dependent behavior of a unidirectional SCS6/Ti–15–3 composite at high temperatures. Experimental data for comparison was provided by Tuttle et al. (1990). Test specimens were manufactured by hot–pressing Ti–15–3 foils between unidirectional tapes of silicon carbide fibers. The diameter of the fibers was 0.14 mm, and the fiber volume content of the composite was 32 percent. Material properties of titanium, for the numerical analysis, were evaluated by fitting experimental data obtained at elevated temperatures from unreinforced specimens. These neat matrix specimens were manufactured by the same process as the composite and so are expected to represent the in situ properties of the matrix in the reinforced specimens. The SCS6 fibers were found to remain elastic in the temperature range considered here. The finite element mesh used for the analysis is shown in Fig. 1.

The first specimen was subjected to a multistep creep test at a temperature of 566°C. Loading was in the direction of the fiber. Figure 13 shows the loading history of axial stress against time in hours. The specimen was allowed to creep at stress levels of 49 MPa, 97 MPa, 167 MPa and 262 MPa with hold time of 1.35, 1.42, 17.20 and 5.11 hours respectively. The computed strain in the axial direction is compared to the experimental record in Fig. 14. The onset of the creep strain is marked in the figure each stress level. For each stress level, the axial strain computed immediately after application of the sustained stress magnitude was drawn to match the strain found in the experiment. In this way, any errors that might have accumulated during application of the overall stress have been subtracted.

Almost no creep strain was measured at the lowest stress of 49 MPa. As expected, both experiment and calculations show an increase in creep rate with increase in the overall stress increment. In general, the numerical model predicted higher rates in the early stages of each step compared to those measured experimentally, however the total creep strains in

16

each step were comparable. Some noise in the experimental data appears in the figure and is attributed to equipment limitations.

In the second experiment, a cyclic strain controlled test was performed at 650°C. The specimen was loaded in the fiber direction at a rate of 10^{-4}/sec to a total strain of 6500×10^{-6}, unloaded at the same rate to 2600×10^{-6} and then reloaded at a higher rate of 10^{-3}/sec to 6500×10^{-6}. A comparison of the measured and computed stress–strain response is shown in Fig. 15. Qualitatively, there is a good agreement between the two, however a stiffer response in predicted from the simulation. Both the experimental data and calculations reach a higher stress at the end of the second cycle as compared to the first, for the same strain level. This is obviously due to the increase in strain rate.

From the limited available experimental data, at elevated temperatures, for the SCS6/Ti–15–3 composite system, it appears that the thermoviscoplastic composite model developed here does predict the actual response fairly well.

2.2   Fatigue Damage in Metal Matrix Composites

Experiments suggest that cyclic loading of metal matrix composites may not lead to fracture, but it results in a substantial reduction of laminate elastic stiffness depending on the applied stress amplitude. The two major causes of stiffness reduction consist of matrix cracks parallel to the fibers and matrix cracks transverse to the fibers. The observed loss of stiffness associated with the matrix cracks transverse to the fibers. The observed loss of stiffness associated with the matrix cracking in unidirectional B/Al composites and laminates cycled under constant amplitude (Dvorak and Johnson 1980) indicates that damage develops only if the load amplitude reaches a certain magnitude in a given laminate, and that the stiffness loss terminates in a saturation damage stat after a certain number of cycles.

Our research developed a failure damage theory with regard to the aforementioned experimental observations. The model recognizes the relation between cyclic plastic straining and damage growth in metal matrix composites, which was described in our previous work (Dvorak and Wung 1988), and focuses on evaluation of the type and extent of damage in individual plies of the laminate, required to reach a shakedown state under a prescribed program of variable cyclic loading. Our choice of micromechanical models is motivated, in part, by experimental observations of the crack systems in individual plies of fatigued laminates. Of course, a detailed description of the actual damage geometry would be quite difficult. Instead, for modeling purposes, the mode of damage that is expected to develop in a given ply is derived from a bimodal damage theory that identifies crack systems associated with the fiber–dominated (FDM) or matrix–dominated (MDM) modes of the analogous bimodal plasticity theory of plastic deformation of fibrous plies, proposed by Dvorak and Bahei–El–Din (1987). An examination of the plastic straining and crack growth processes leads to the conclusion that the actual saturation damage state corresponds to a minimum amount of damage required for shakedown of the laminate. Appropriate crack density measure are introduced, and the total crack density in the laminate is identified with an objective function that is minimized with an optimization scheme that involves physically based nonlinear constraints in a general loading domain (Dvorak, Lagoudas and Huang 1990b). The analysis evaluates stiffness changes in the saturation state and also yields estimates of the average stresses in fibers of the damaged composite.

A comparison of the theoretical predictions indicated by the present optimization procedure, with experiments conducted by Dvorak and Johnson (1980) is given in Fig. 16 for a $(0/90)_{2s}$ laminate and in Fig. 17 for a $(0/\pm45/90/0/\pm45/\frac{1}{4}90)_{2s}$ laminate. The correlation is quite good for the whole range of stress amplitudes applied in the optimization scheme, as it can be seen from the figures. We note that the optimization scheme may be come unstable if the applied stress amplitude becomes too large. Moreover,

the analysis itself may not be applicable if the maximum stress approaches about 90% of the endurance limit, due to the experimentally detected frequency of fiber breaks.

As the composite's endurance limit is approached, damage development in the matrix almost unloads completely the matrix and transfers the applied loading to the fibers. The composite will eventually fail when the endurance limit of the fibers in the 0° plies as a function of the maximum applied overall stress for the $(0/90)_{2s}$, $(0/\pm45/90/0/\pm45/\frac{1}{2}90)_{2s}$ laminates and a 0_8 unidirectional in Fig. 18. The maximum applied stress ranges from zero up to the endurance limit of the laminate as reported by Dvorak and Johnson (1980) (the endurance limit of the 0_8 is taken to be 800 MPa, of the $(0/90)_{2s}$ is 500 MPa and of the $(0/\pm45/90/0/\pm45/\frac{1}{2}90)_{2s}$ laminate indicates extrapolation from the last computed point that corresponds to 325 MPa. Taking into consideration the scattering in the experimental data for the endurance limit of the various laminates, the maximum fiber stress (fiber endurance limit) may be approximated by the average of the maximum fiber stresses in the three cases of Fig. 18.

3. EXPERIMENTAL WORK

3.1 Equipment

Under partial support from this grant, we have acquired a new high temperature testing facility for biaxial loading of composite thin–walled tube specimens. Mechanical loads are applied by a MTS axial–torsion servohydraulic machine. The maximum loads are ± 225 KN axial, and 2.8 KN–m in torsion. An IBM 386 microcomputer is connected to the testing system for data acquisition and load control.

Test temperatures are provided and controlled by a resistive furnace manufactured by CM Furnaces, Inc. This is a vertical tube furnace which splits open along a vertical axis to wrap around the specimen. The unit consists of three independent heating zones placed on top of each other. The center zone is 2" long and the top and bottom zones are each 1" long. The resistive heaters are made of platinum rhodium 60/40 0.020" diameter wire. The inner diameter of the furnace is 2" and the outer diameter about 10" which enables the furnace to be accommodated in the existing MTS machine frame. The overall height of the furnace is approximately 6". The maximum operating temperature of the furnace is 1400° C. The temperature gradient along the length of the center zone, where the strain measurements are usually made, was evaluated by heating a steel tube with thermocouples connected to its inner and outer surfaces. At 1000° C, the temperature in the gage area was 1000 ± 2° C.

Strain measurements are made with a biaxial MTS extensometer. The extensometer is water cooled and can be used in conjunction with quartz connecting rods which make it possible to operate at 1000° C or with ceramic rods that can operate at 1200° C. The extensometer rod ends contact single points on the tubular specimen wall and pivot on them to measure extension and rotation. The contact points require small dimples be imprinted on the specimen to avoid any slippage during test. To prevent

20

damaging the composite specimen, the required dimples will be imprinted on small tabs made of ceramic cement and affixed to the specimen. The gage length of the extensometer is 1" and the operating ranges are ± 0.1" in the axial direction and ± 5° in the torsional direction. However, the maximum windup at the contact points is ± 10° which dictates on the torsional range which we can measure with our tubular specimen. The strain ranges computed from the above values are ± 10% for the normal strain in the axial direction, and ± 1.5% for the longitudinal shear strain.

3.2   Specimens

The composite system selected for this project is a nickel base Waspaloy matrix reinforced by GE 218 tungsten wire. This system was selected based on experience gained during fabrication of flat specimens of the same system by Westinghouse. Last year, we contracted Westinghouse for fabrication of thin wall tubular specimens for this project. Fiber volume fraction was specified as 0.35 and the number of plies as 5. The specimen diameter (1.25") and length (15") were selected to conform with the equipment described above and with gripping outside the furnace. Delivery of the specimen was delayed several times due to inability of General Electric to provide 3D tungsten wire, and due to the lack of a standard procedure for making superalloy matrix composite tubes. The tubes were finally delivered in early 1992. The report by Blankenship (1992) in the enclosure describes the manufacturing procedure. The tubes will be tested under the forthcoming AFOSR grant, in the summer–fall period of 1992.

ACKNOWLEDGMENT

REFERENCES

Blankenship, W.P. and Przywaarty, F.L., (1992), "Fabrication of Metal Matrix Composite Tubes for Rensselaer Polytechnic Institute," Report by Westinghouse Electric Corporation, Advanced Energy Systems Department, Pittsburgh, PA

Burden, R.L. and Faires, J.D., (1985), <u>Numerical Analysis</u>, third edition, Prindle, Weber and Schmidt Publishers, Boston.

Dafalias, Y.F. and Popov, E.P., (1976), "Plastic Internal Variable Formalism of Cyclic Plasticity," <u>ASME J. Appl. Mech.</u>, Vol. 43, p. 645.

Dvorak, G.J. and Johnson, W.S., (1980), "Fatigue of Metal Matrix Composites," <u>Int. J. of Fracture</u>, Vol. 16, p. 585.

Dvorak, G.J., (1983), "Metal Matrix Composites: Plasticity and Fatigue," in <u>Mechanics of Composite Materials: Recent Advances</u>, Z. Hashin and C.T. Herakovich, editors, Pergamon Press, pp. 73–91.

Dvorak, G.J. and Teply, J.L., (1985), "Periodic Hexagonal Array Models for Plasticity of Composite Materials," <u>Plasticity Today: Modeling, Methods and Application</u>, W. Olszak Memorial Vol., A. Sawczuk and V. Blanchi, Editors, Elsevier, p. 623.

Dvorak, G.J., (1986), "Thermal Expansion of Elastic–Plastic Composite Materials," <u>J. Appl. Mech.</u>, Vol. 53, pp. 737–743.

Dvorak, G.J., (1937), "Thermomechanical Deformation and Coupling in Elastic–Plastic Composite Materials," in <u>Thermomechanical Couplings in Solids</u>, H.D. Bui, and Q.S. Nguyen, editors, North–Holland, pp. 43–54.

Dvorak, G.J. and Bahei–El–Din, Y.A., (1987), "A Bimodal Plasticity Theory of Fibrous Composite Materials," <u>Acta Mechanica</u>, Vol. 69, p. 219.

Dvorak, G.J., Bahei–El–Din, Y.A., Macheret, Y., and Liu, C.H., (1988), "An Experimental Study of Elastic–Plastic Behavior of a Fibrous Boron–Aluminum Composite," <u>J. Mech. Phys. Solids</u>, Vol. 36, p. 655.

Dvorak, G.J. and Wung, E.C.J., (1988), "Fatigue Damage Mechanics of Metal Matrix Composite Laminates," in <u>Strain Localization and Size Effect Due to Cracking and Damage</u>, J. Mazars and Z.P. Bazant, eds., Elsevier, London.

Dvorak, G.J., (1990) "On Uniform Fields in Heterogeneous Media," <u>Proceedings of the Royal Society</u>, London, A 431, pp. 89–110.

Dvorak, G.J. Bahei–El–Din, Y.A., Shah, R.S., Nigam, H., (1990), "Experiments and Modeling in Plasticity of Fibrous Composites," in <u>Inelastic Deformation of Composite Materials</u>, G.J. Dvorak, editor, Springer–Verlag, New York, Inc., pp. 270–293.

Dvorak, G.J., Lagoudas, D. and C. Huang, (1990), "Fatigue Damage of Metal Matrix Composites: Optimization and Shakedown Analysis," <u>AMD – Vol. 11/MD – Vol. 22</u>, American Society of Mechanical Engineers, New York, pp. 41–54.

Dvorak, G.J., (1991), "Plasticity Theories for Fibrous Composite Materials," Metal Matrix Composites, Vol. 2, R.K. Everett and R.J. Arsenault, Editors, Academic Press, Boston, pp. 1–77.

Dvorak, G.J., (1992b), "Transformation Field Analysis of Inelastic Composite Materials," Proceedings of the Royal Society, London, A437, pp. 311–327.

Dvorak, G.J. and Benveniste, Y., (1992a), "On Transformation Strains and Uniform Fields in Multiphase Elastic Media, Proceedings of the Royal Society, London, A 437, pp. 291–310.

Eisenberg, M.A., and Yen, C.F., (1981), "A Theory of Multiaxial Anisotropic Viscoplasticity," ASME J. Appl. Mech., Vol. 48, p. 276.

Hall, R., (1990), Ph.D. Dissertation, Rensselaer Polytechnic Institute.

Kumar, V., Morjaria, M. and Mukherjee, S., (1980) "Numerical Integration of Some Stiff Constitutive Models of Inelastic Deformation," J. Eng. Matls. Tech., v. 102, pp. 92–96.

Shah, R.S., Bahei–El–Din, Y.A., and Dvorak, G.J., (1990), "A Numerical Study of the Rate–Dependent Behavior of High Temperature Fibrous Composite Systems," IUTAM Symposium on Inelastic Deformations of Composite Materials, Rensselaer Polytechnic Institute.

Shah, R.S., (1991), "Modeling and Analysis of High–Temperature Inelastic Deformation in Metal–Matrix Composites," Ph.D. Thesis, Rensselaer Polytechnic Institute.

Teply, J.L. and Dvorak, G.J., (1988), "Bounds on Overall Instantaneous Properties of Elastic–Plastic Composites," J. Mech. Phys. Solids, Vol. 36, p. 29.

Tuttle, M., Rogacki, J. and Johnson, W.S., (1990), Private Communication.

Table 1 Parameters used in prediction of Ti–15–3 behavior

Material Property	Units	27°C	482°C	649°C
E	GPa	92.4	72.2	55.0
ν		0.351	0.351	0.351
Y	MPa	810	250	52.5
H_0	MPa	1400	60	50
h	GPa	40	90	52
$\bar{Y}$	MPa	930	870	278
p		9.95	2.45	1.43
k	$(MPa)^{-p}/s$	7.6×10^{-20}	4.2×10^{-7}	3.2×10^{-6}
Q_a	MPa	−120	−220	−30
$\bar{Q}_a$	MPa	50	1700	95
q		920	7.5	2.61
$\bar{q}$		920	7.5	2.61
m_r		1.2	1.29	1.35
c_r	$(MPa)^{-m_r+1}/s$	1.0×10^{-4}	7.0×10^{-4}	2.0×10^{-4}
$\bar{c}_r$	$(MPa)^{-\bar{m}_r+1}/s$	1.0×10^{-4}	7.0×10^{-4}	2.0×10^{-4}

FIGURES

Fig. 1   Finite element subdivisions of the PHA representative volume element.

Fig. 2   Examples of bimodal yield surfaces.

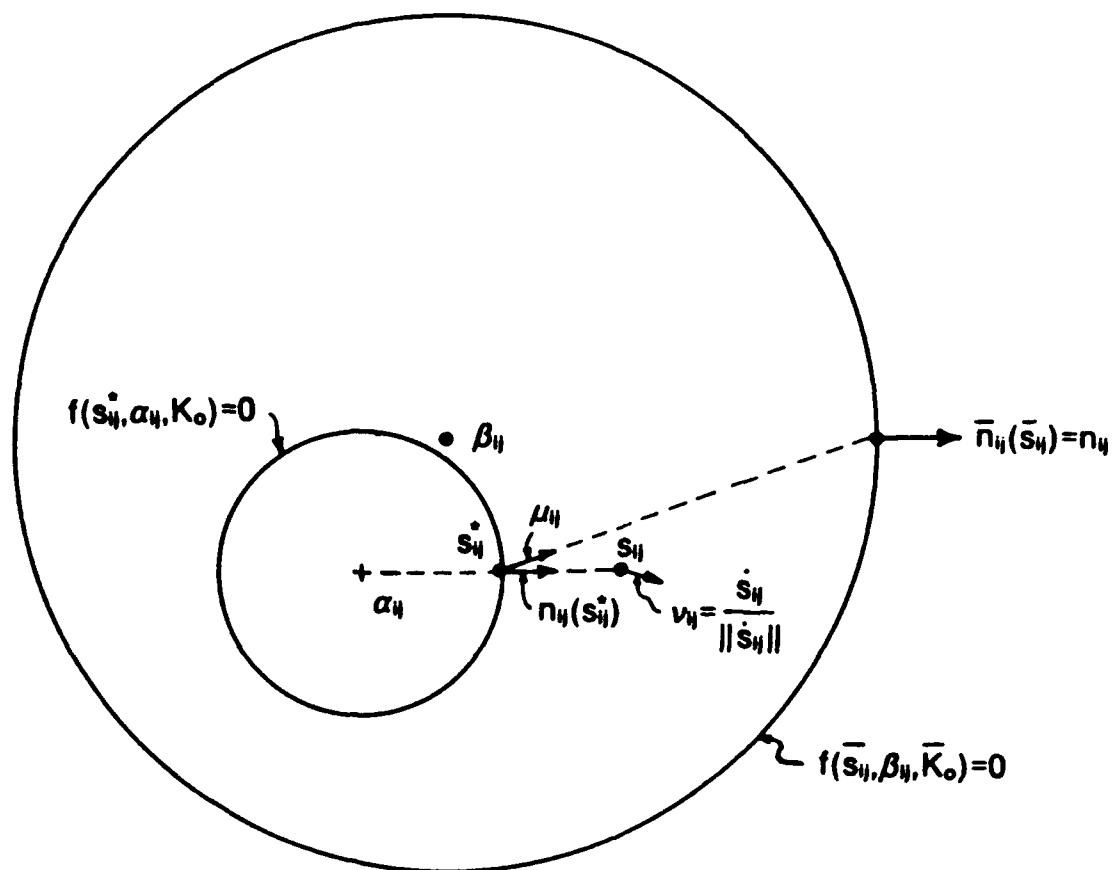$f(\overset{*}{s}_{ij}, \alpha_{ij}, K_o) = 0$

β_{ij}

$\overline{n}_{ij}(\overline{s}_{ij}) = n_{ij}$

μ_{ij}

$\overset{*}{s}_{ij}$

s_{ij}

α_{ij}

$+$

$n_{ij}(\overset{*}{s}_{ij})$

$\nu_{ij} = \dfrac{\dot{s}_{ij}}{\|\dot{s}_{ij}\|}$

$f(\overline{s}_{ij}, \beta_{ij}, \overline{K}_o) = 0$

Fig. 3   Schematic of equilibrium yield surface and bounding surface in the stress space of an elastically isotropic material.

Fig. 4   Comparison of measured and computed response of a Ti–15–3 specimen at room temperature and stress rate of 2.6 MPa/s.

Fig. 5   Comparison of measured and computed response of a Ti–15–3 specimen at 482°C and stress rate of 2.6 MPa/s.
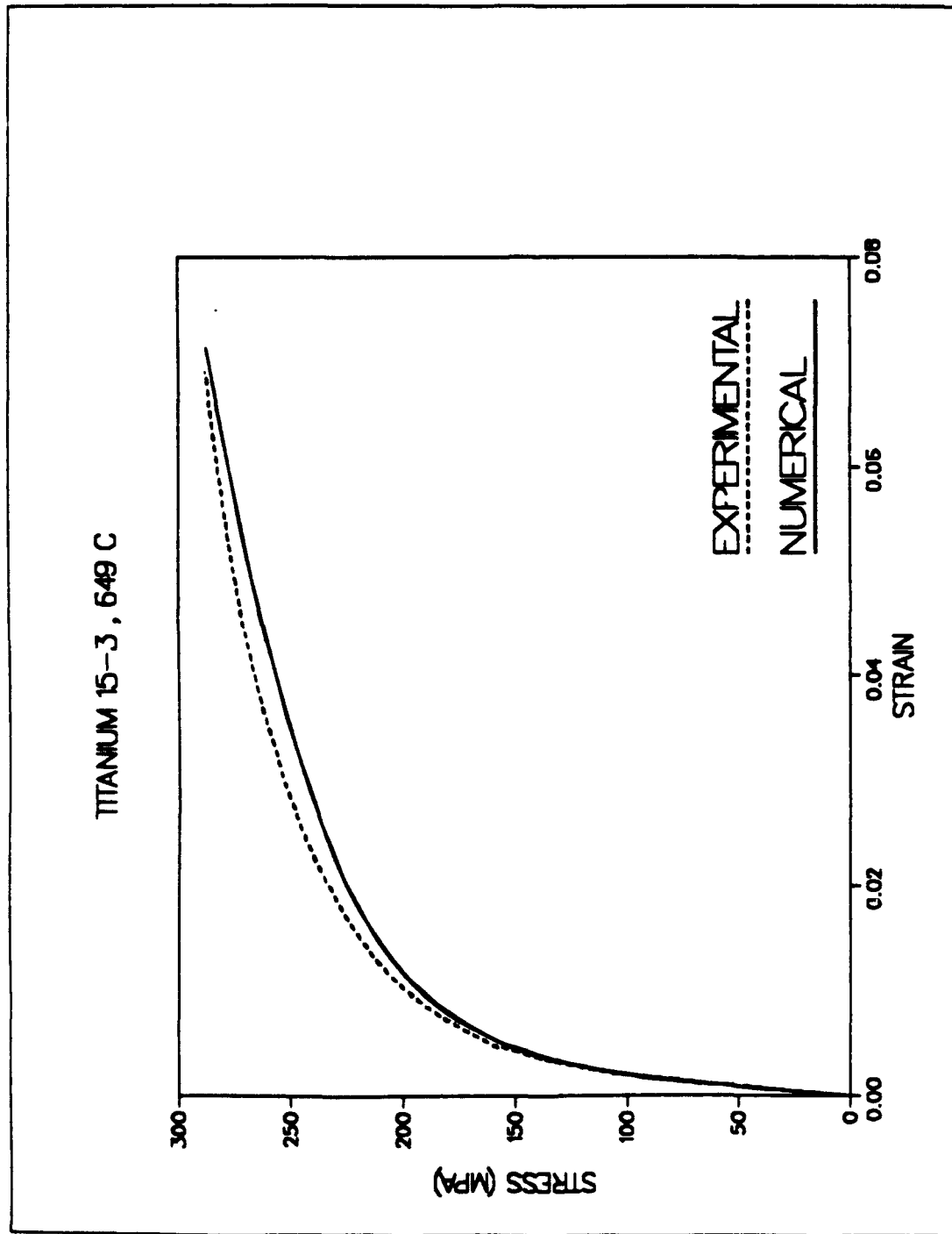
Fig. 6   Comparison of measured and computed response of a Ti–15–3 specimen at 649°C and stress rate of 2.6 MPa/s.
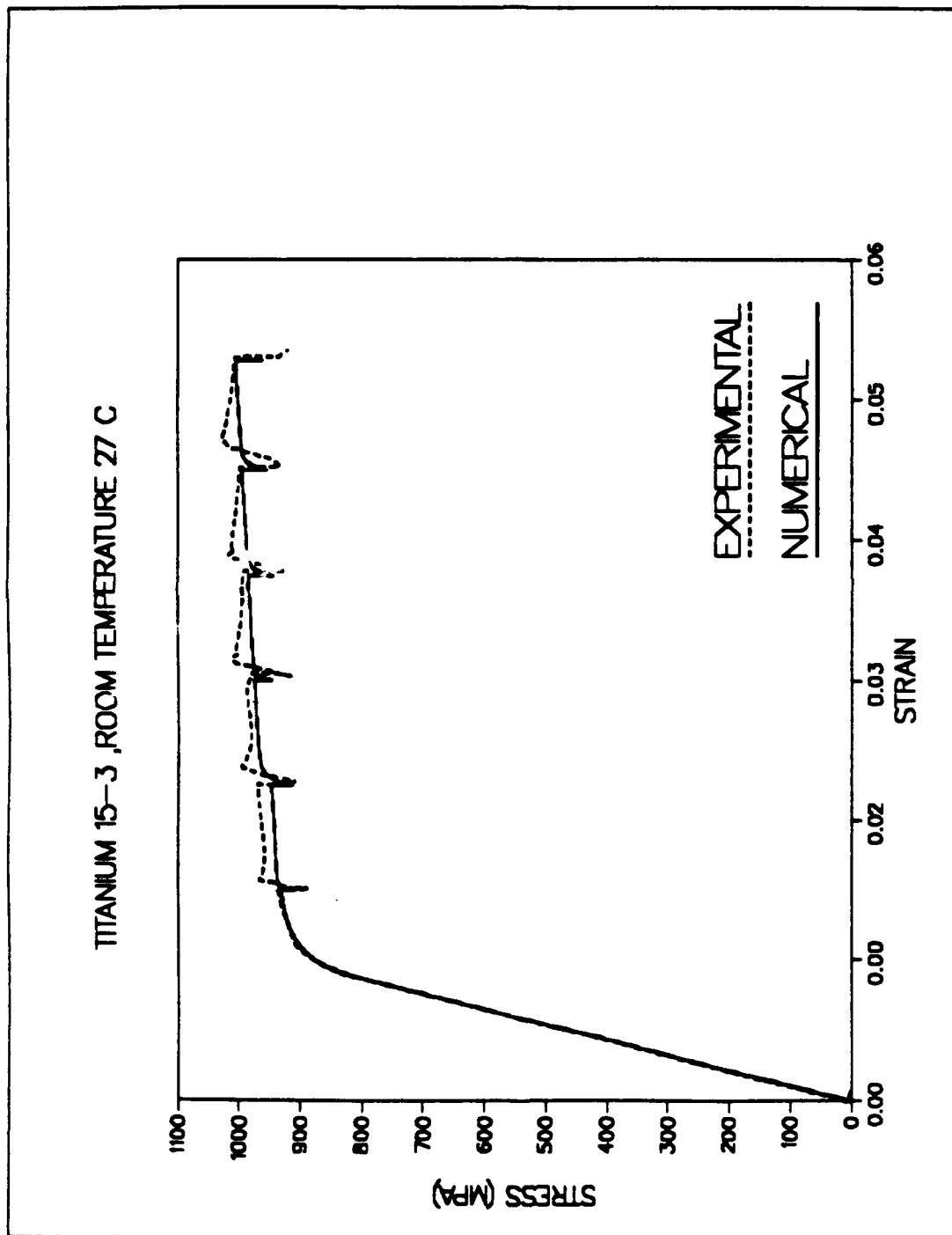
Fig. 7   Comparison of measured and computed response of a Ti–15–3 specimen at room temperature and strain rate of $10^{-4}/s$.
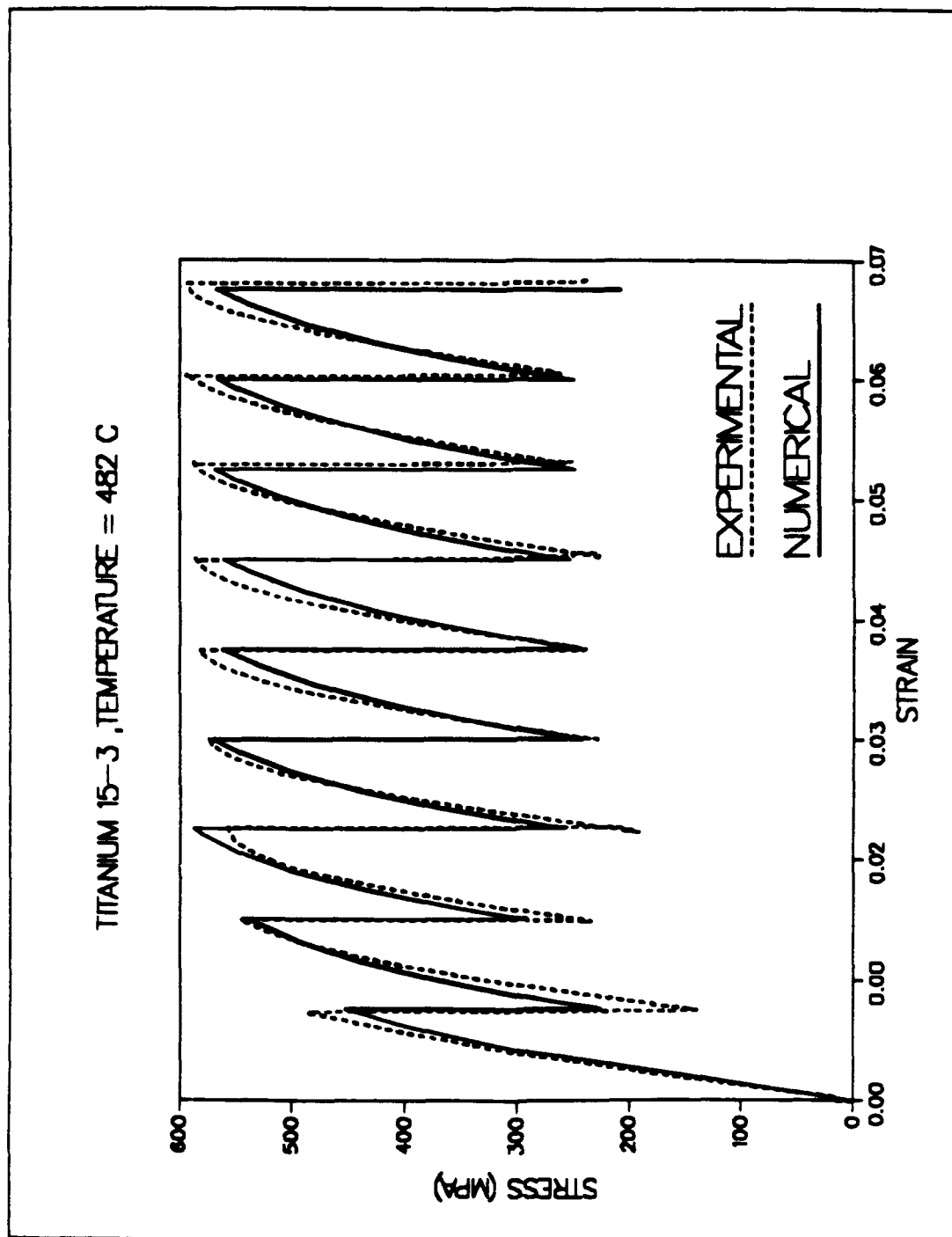
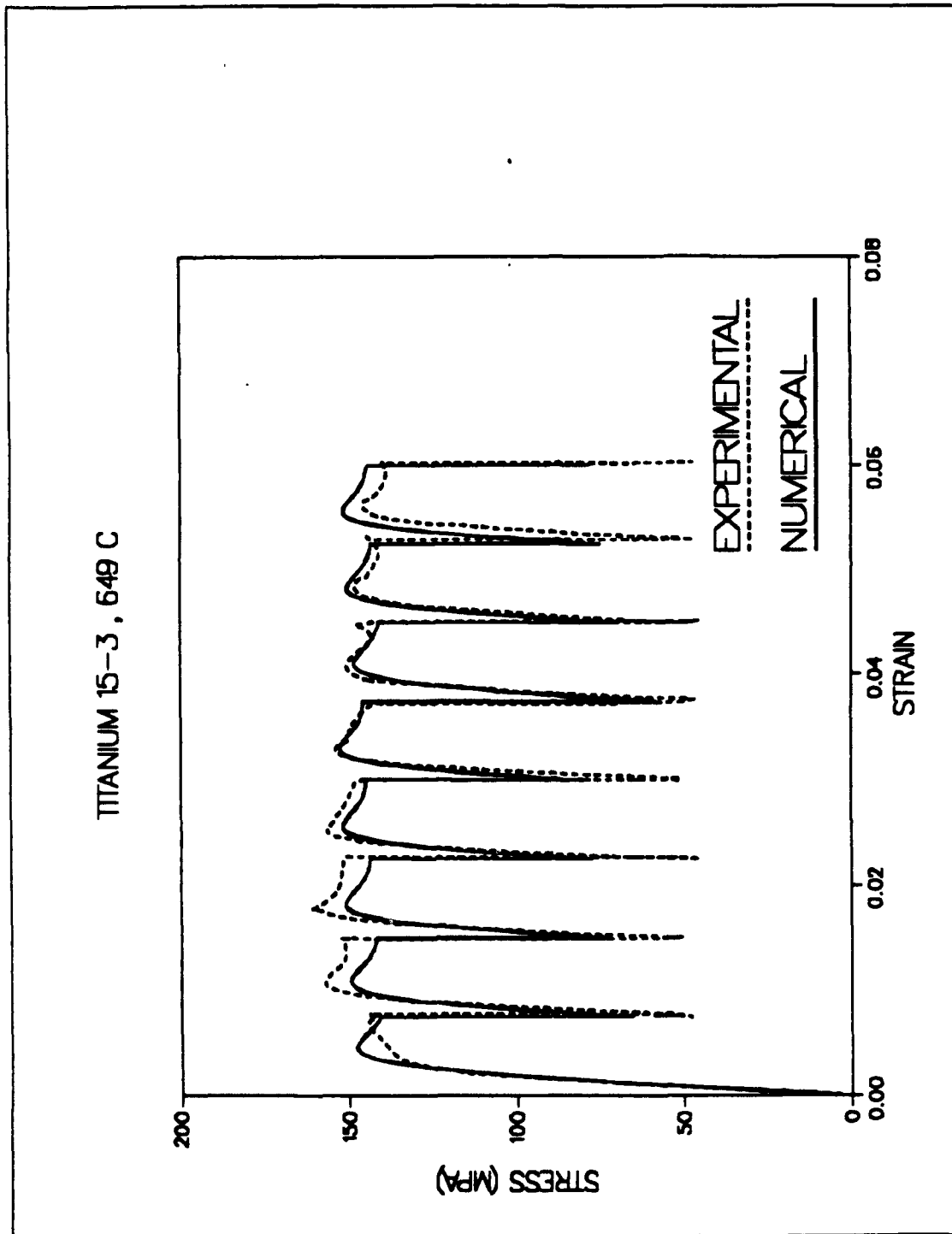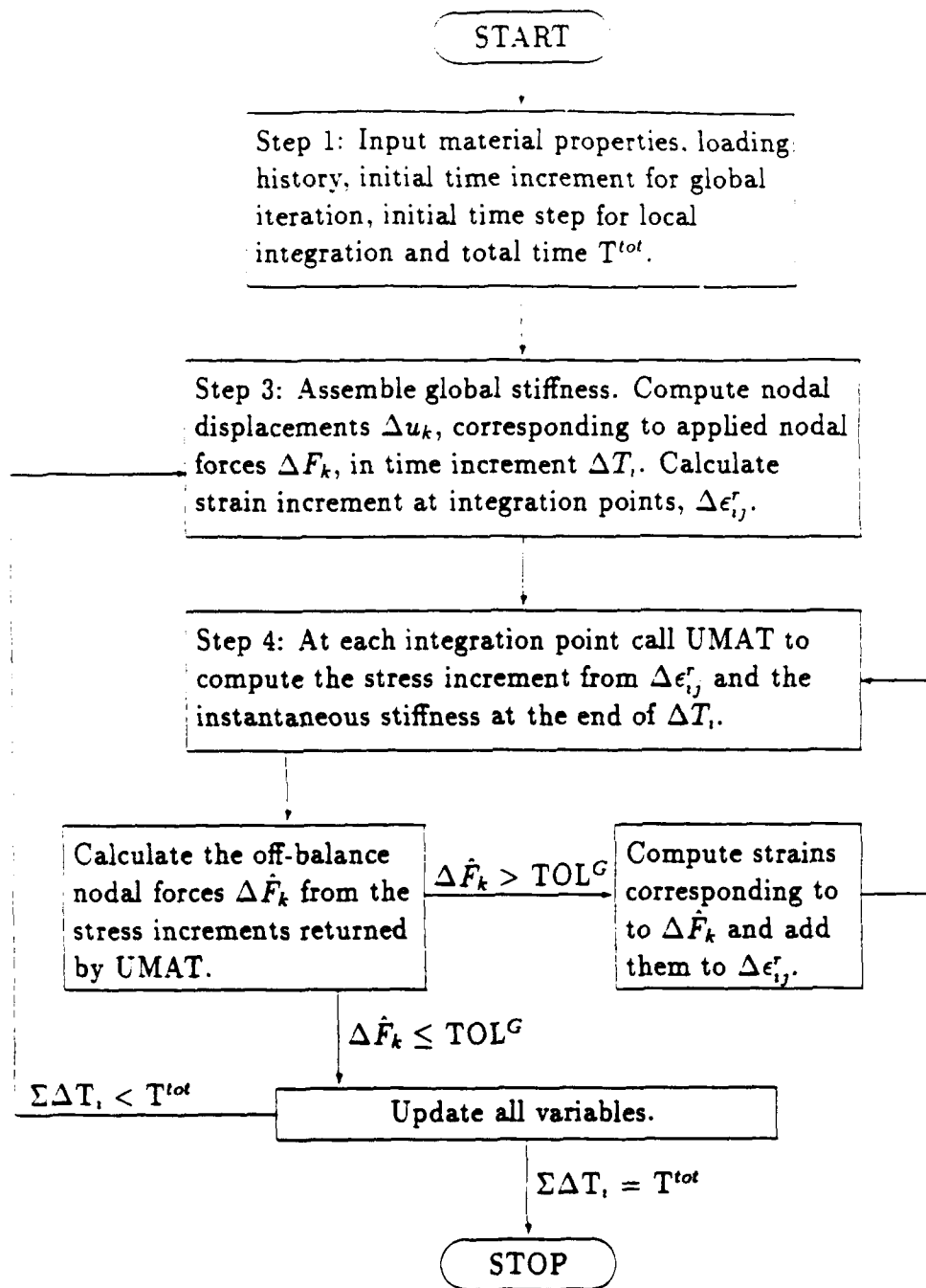Fig. 8   Comparison of measured and computed response of a Ti–15–3 specimen at 482°C and strain rate of 10^{-4}/s.

Fig. 9   Comparison of measured and computed response of a Ti–15–3 specimen at 649°C and strain rate of 10⁻⁴/s.

START

Step 1: Input material properties. loading
history, initial time increment for global
iteration, initial time step for local
integration and total time T^{tot}.

Step 3: Assemble global stiffness. Compute nodal
displacements Δu_k, corresponding to applied nodal
forces ΔF_k, in time increment ΔT_i. Calculate
strain increment at integration points, $\Delta \epsilon_{ij}^r$.

Step 4: At each integration point call UMAT to
compute the stress increment from $\Delta \epsilon_{ij}^r$ and the
instantaneous stiffness at the end of ΔT_i.

Calculate the off-balance
nodal forces $\Delta \hat{F}_k$ from the
stress increments returned
by UMAT.

$\Delta \hat{F}_k > TOL^G$

Compute strains
corresponding to
to $\Delta \hat{F}_k$ and add
them to $\Delta \epsilon_{ij}^r$.

$\Delta \hat{F}_k \leq TOL^G$

$\Sigma \Delta T_i < T^{tot}$

Update all variables.

$\Sigma \Delta T_i = T^{tot}$

STOP

Fig. 10   Flowchart of global iteration scheme for the ABAQUS finite element
program.
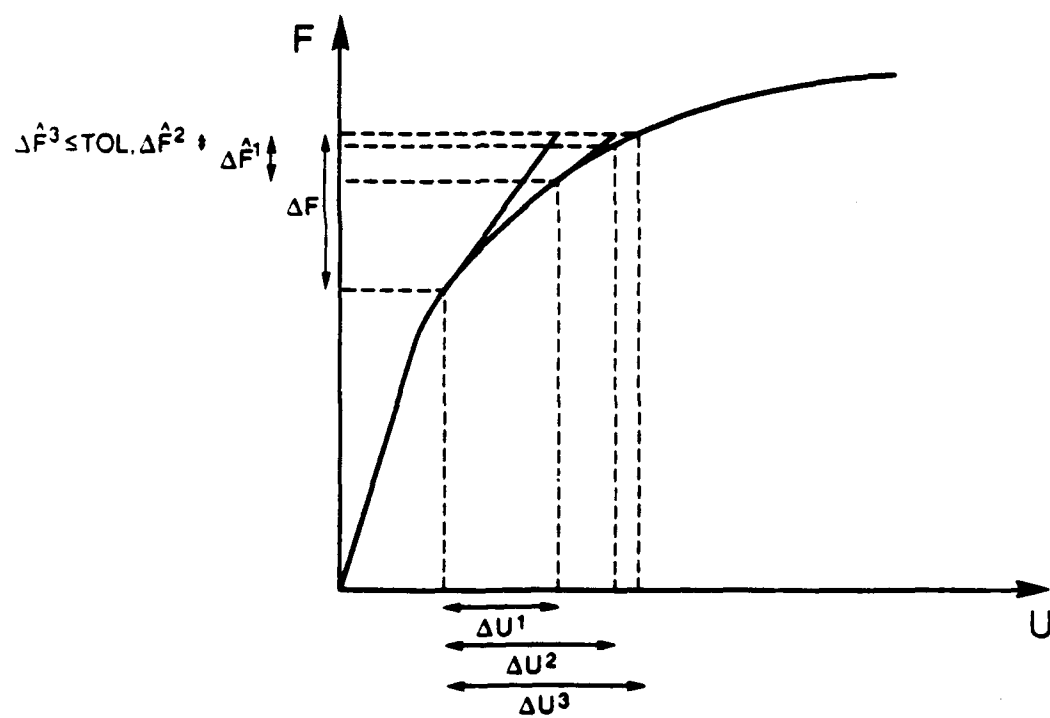
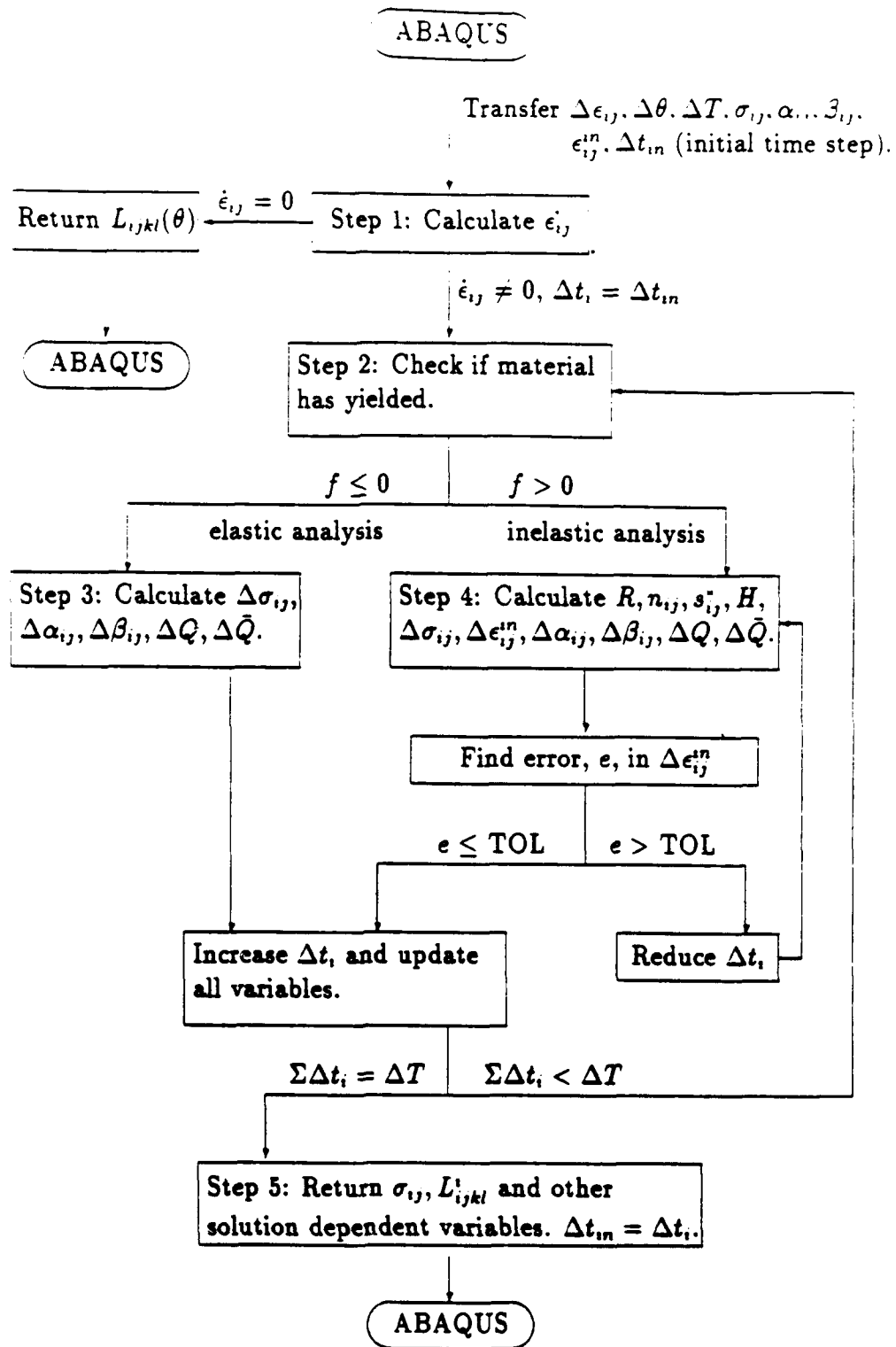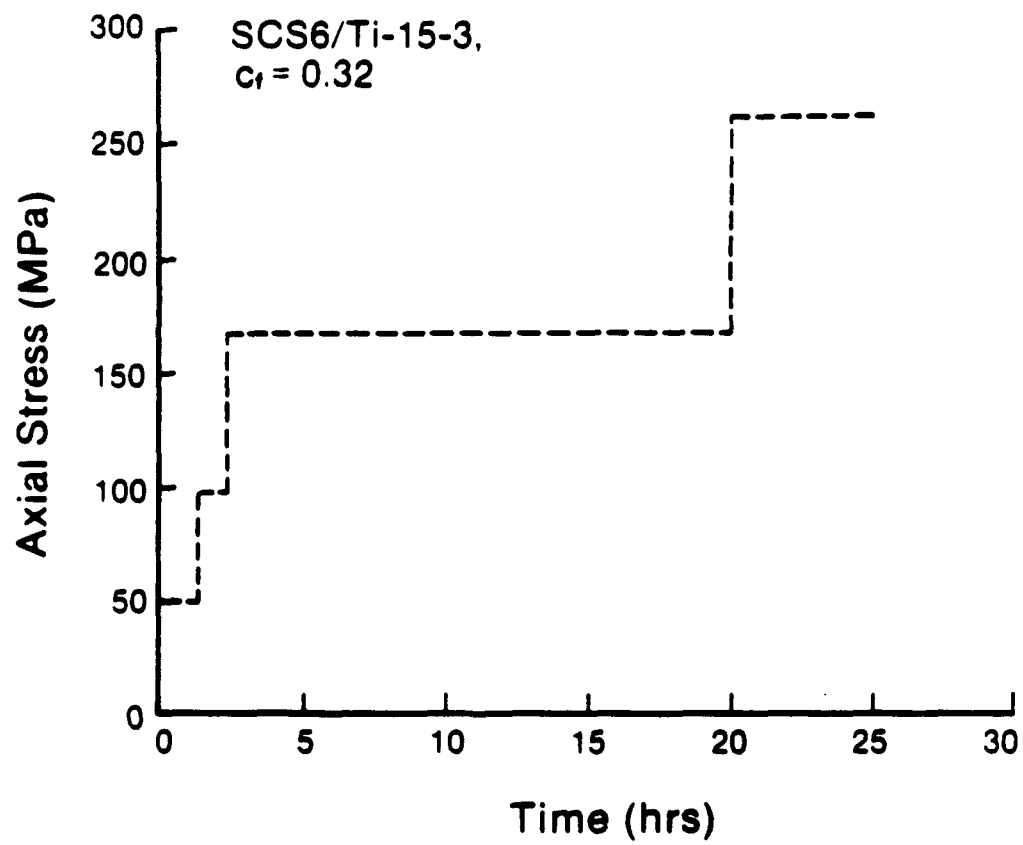Fig. 11   Newton–Raphson procedure for global iteration.

ABAQUS

Transfer $\Delta\epsilon_{ij}, \Delta\theta, \Delta T, \sigma_{ij}, \alpha \ldots \beta_{ij},$
$\epsilon_{ij}^{in}, \Delta t_{in}$ (initial time step).

Return $L_{ijkl}(\theta)$ $\xleftarrow{\quad \dot\epsilon_{ij}=0 \quad}$ Step 1: Calculate $\dot\epsilon_{ij}$

$\dot\epsilon_{ij} \neq 0, \Delta t_i = \Delta t_{in}$

ABAQUS

Step 2: Check if material has yielded.

$f \leq 0$ $f > 0$

elastic analysis   inelastic analysis

Step 3: Calculate $\Delta\sigma_{ij}$, $\Delta\alpha_{ij}, \Delta\beta_{ij}, \Delta Q, \Delta\bar{Q}$.

Step 4: Calculate $R, n_{ij}, s_{ij}^-, H,$ $\Delta\sigma_{ij}, \Delta\epsilon_{ij}^{in}, \Delta\alpha_{ij}, \Delta\beta_{ij}, \Delta Q, \Delta\bar{Q}$.

Find error, e, in $\Delta\epsilon_{ij}^{in}$

$e \leq$ TOL $e >$ TOL

Increase Δt_i and update all variables.

Reduce Δt_i

$\Sigma\Delta t_i = \Delta T$ $\Sigma\Delta t_i < \Delta T$

Step 5: Return σ_{ij}, L_{ijkl}^t and other solution dependent variables. $\Delta t_{in} = \Delta t_i$.

ABAQUS

Fig. 12   Flowchart of UMAT procedure.

Fig. 13   Stress history applied in multistep creep test of a SCS6/Ti—15—3 composite.
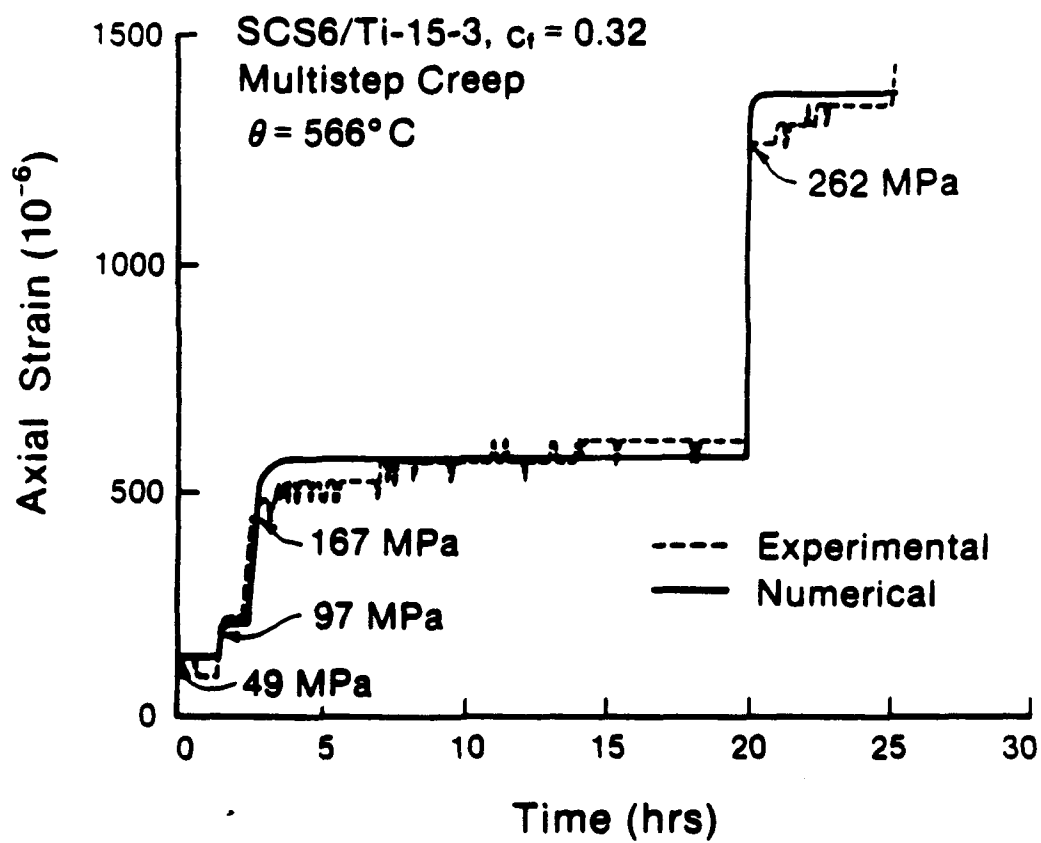
Fig. 14   Comparison of computed and measured strain found in a multistep creep test on a SCS6/Ti–15–3 composite.
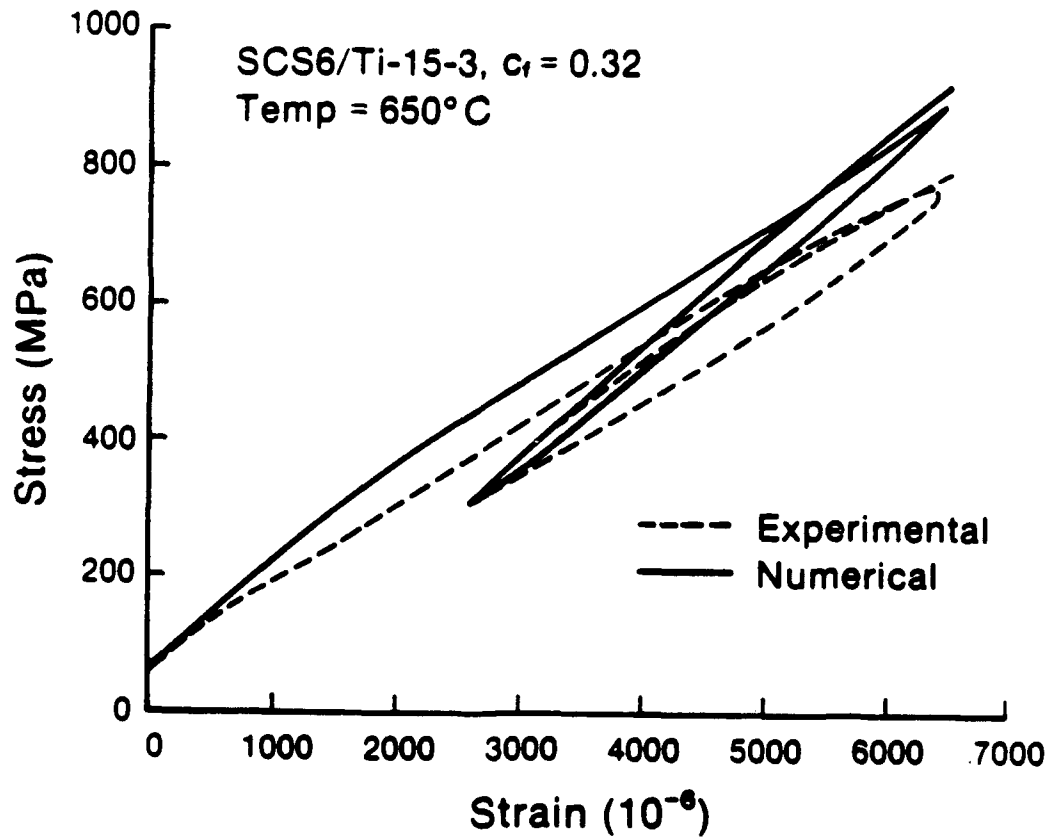
Fig. 15   Comparison of computed and measured response for a cyclic strain controlled test.
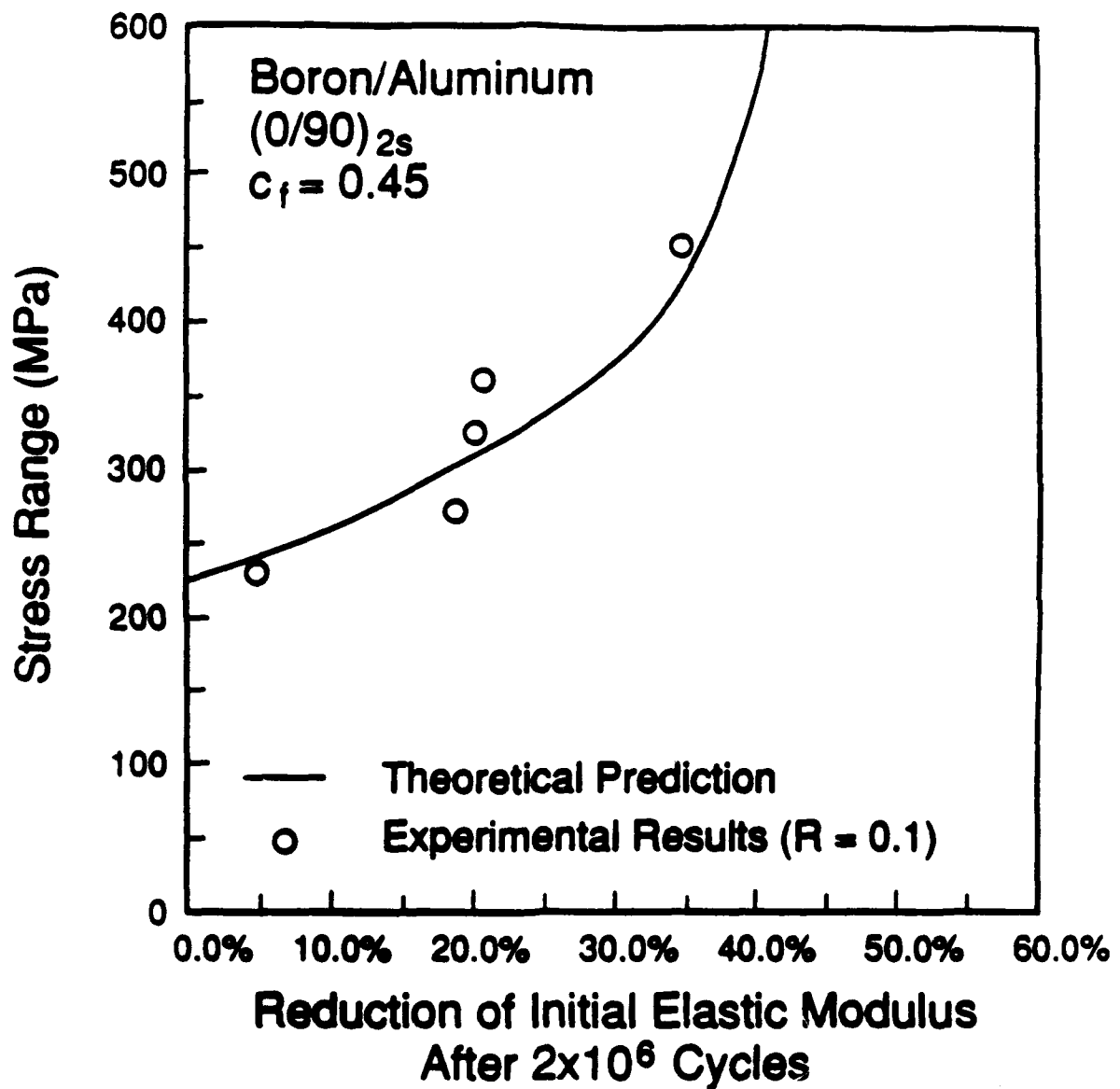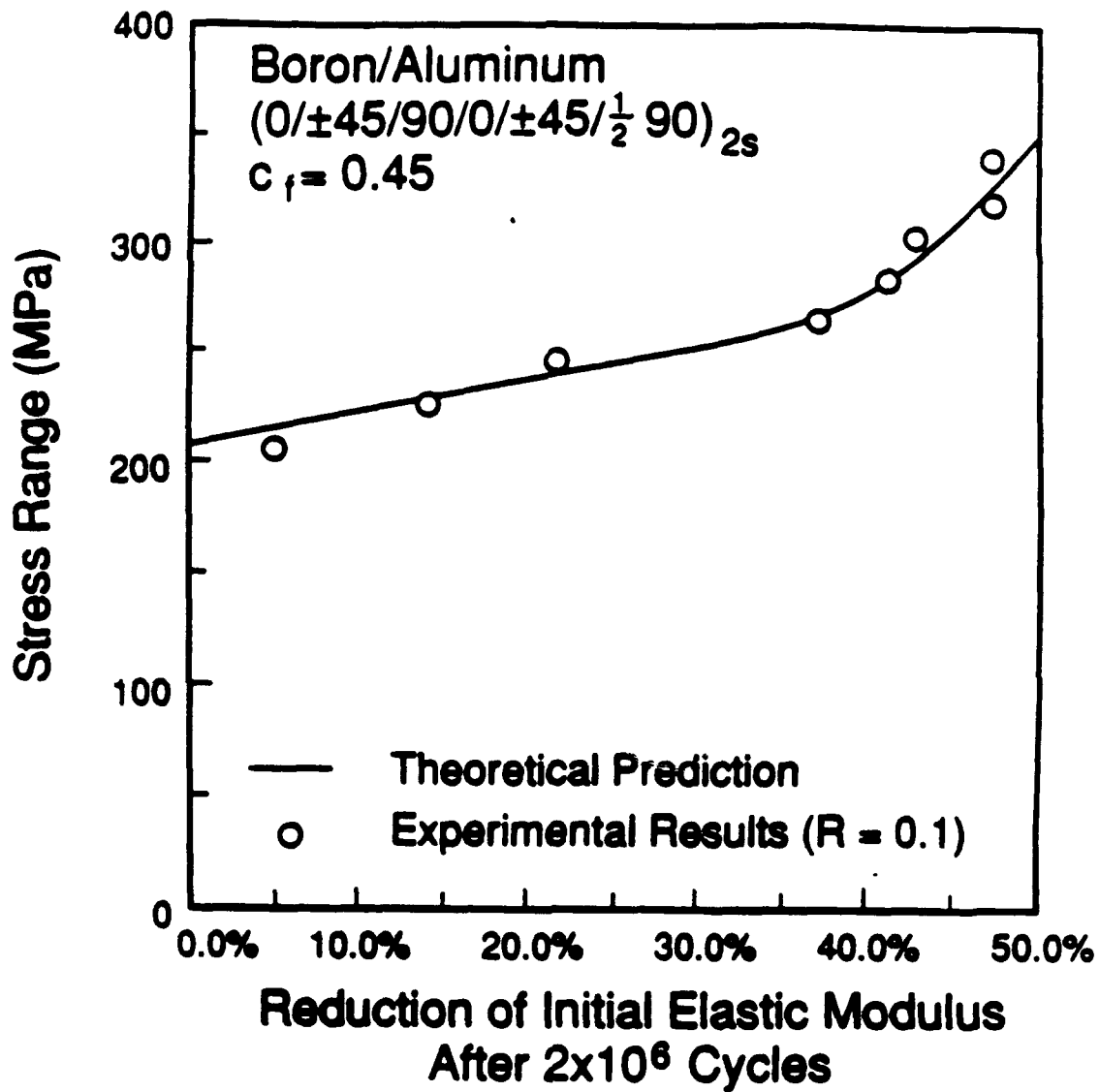
Fig. 16   Reduction in elastic stiffness of a $(0/90)_s$ laminate as a function of applied
stress amplitude. Experimental data by Dvorak and Johnson (1980)
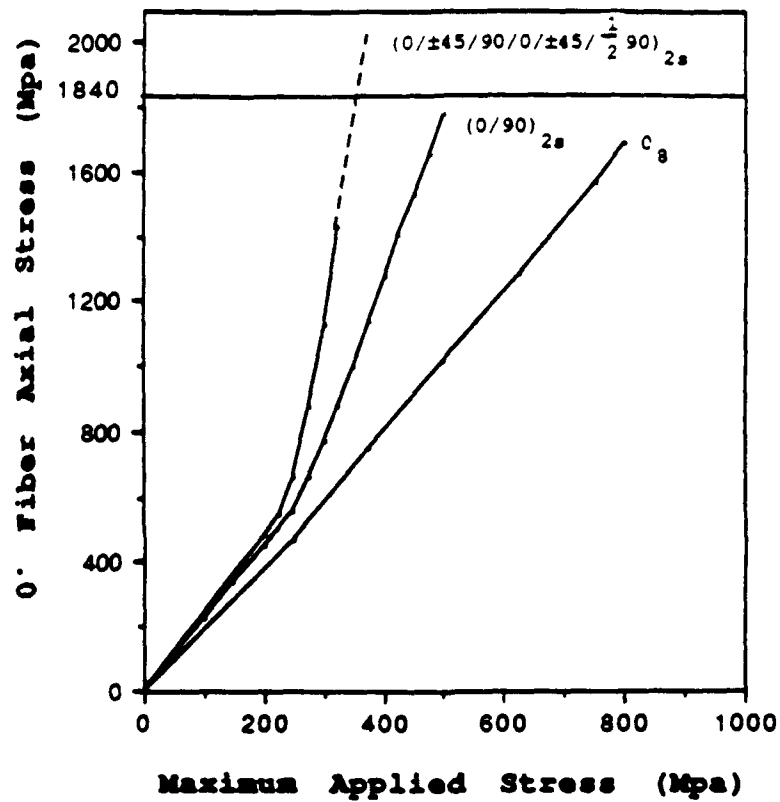compared with predictions by the damage optimization procedure.

Fig. 17   Reduction in elastic stiffness of a $(0/\pm45/90/0/\pm45/\frac{1}{4}90)_s$ laminate as a function of the applied stress amplitude. Experimental data by Dvorak and Johnson (1980) compared with predictions by the damage optimization procedure.

Fig. 18   Maximum fiber stress in the 0° plies as a function of the maximum overall applied stress up to the endurance limit for various layup configurations.

LIST OF PUBLICATIONS

G.J. Dvorak and E.C.J. Wung, (1988), "Fatigue Damage Mechanics of Metal Matrix Composite Laminates," Cracking and Damage Strain Localization and Size Effect, ed., J. Mazars and Z.P. Bazant, Elsevier Applied Science Publishers Limited, London.

G.J. Dvorak, D. Lagoudas and C. Huang, (1990), "Fatigue Damage of Metal Matrix Composites: Optimization and Shakedown Analysis," AMD – Vol. 111/MD – Vol. 22, American Society of Mechanical Engineers, New York, pp. 41–54.

G.J. Dvorak, (1990), "On Uniform Fields in Heterogeneous Media," Proc. Royal Soc. London, A 431, pp. 89–110.

Y. Benveniste and G.J. Dvorak, (1992), "On a Correspondence Between Mechanical and Thermal Fields in Composites with Slipping Interfaces," Inelastic Deformation of Composite Materials, G.J. Dvorak, Ed., Springer–Verlag, New York, pp. 75–91.

Y. Benveniste, G.J. Dvorak and T. Chen, (1991), "On Diagonal and Elastic Symmetry of the Approximate Effective Stiffness Tensor of Heterogeneous Media," Journal of the Mechanics and Physics of Solids, pp. 927–946.

G.J. Dvorak, (1991), "On Thermal Hardening and Uniform Fields in Two–phase Composite Materials," in Anisotropy and Localization of Plastic Deformation, ed. by J–P. Boehler and A. Khan, Elsevier Applied Science, London, pp. 19–22.

Y.A. Bahei–El–Din, R.S. Shah and G.J. Dvorak, (1991), "Numerical Analysis of the Rate–Dependent Behavior of High Temperature Fibrous Composites," AMD–Vol. 118, Mechanics of Composites at Elevated and Cryogenic Temperatures, edited by S.N. Singhal, W.F. Jones and C.T. Herakovich, pp. 67–78.

Y.A. Bahei–El–Din and G.J. Dvorak, (1991), "Local Fields in Uncoated and Coated High Temperature Fibrous Composite Systems," AD–Vol. 25–2, Damage and Oxidation Protection in High Temperature Composites – Vol. 2, ASME, pp. 21–34.

G.J. Dvorak, T. Chen and J. Teply (1992), "Thermomechanical Stress Fields in High–Temperature Fibrous Composites: I. Unidirectional Laminates," Composite Science and Technology, Vol. 43, pp. 347–358.

G.J. Dvorak, T. Chen and J. Teply (1992), "Thermomechanical Stress Fields in High–Temperature Fibrous Composites: II. Laminated Plates," Composite Science and Technology, Vol. 43, pp. 359–368.

G.J. Dvorak and Y. Benveniste, (1992), "On the Thermomechanics of Composites with Imperfectly Bonded Interfaces and Damage," to appear in International Journal of Solids and Structures.

LIST OF PRESENTATIONS

Presentations by Dr. Dvorak

ASME/WAM, "On a Correspondence Between Mechanical and Thermal Effects in Two-Phase Composites," San Francisco, CA, December 10–15, 1989.

Invited Lecture, Department of Applied Mechanics and Engineering Science, University of California, San Diego, March 5, 1990.

Short Course on "Metal Matrix Composites," (program co-director and lecturer), UCLA, March 6–8, 1990.

Invited Lecture, University of Illinois–Chicago, April 25, 1990.

Invited Lecture, Northwestern University, April 26, 1990.

IUTAM Symposium on Inelastic Deformation of Composite Materials, "Some Experimental Results in Plasticity of Fibrous Composites," Rensselaer Polytechnic Institute, Troy, NY, May 29–June 1, 1990.

United Technologies Engineering Coordination Activities Conference, "Fracture of Fibrous Composites," Stamford, Connecticut, May 14–18, 1990 (presented by J. Zarzour).

IST–SDIO/ONR Woods Hole IV Research Review, "Local Stresses in High Temperature Composites and Laminates," Woods Hole, Massachusetts, June 4, 1990.

Invited Lectures, Politecnico di Milan, Milan, Italy, June 11–12, 1990.

Invited Lecture, EniChem, Milan, Italy, June 13, 1990.

Invited Lecture, Institute of Theoretical and Applied Mechanics, Czechoslovak Academy of Sciences, Prague, Czechoslovakia, June 25, 1990.

Short Course on "Advanced Composite Materials and Structures," RPI, July 24, 1990.

KAPL corporate visit, RPI, August 3, 1990

Grumman Aircraft visit, RPI, August 8, 1990.

ASME/WAM, "On Uniform Fields in Heterogeneous Media," Dallas, Texas, November 27, 1990.

ASME/WAM, "Fatigue Damage of Metal Matrix Composites: Optimization and Shakedown Analysis," Dallas, Texas, November 27, 1990.

AFOSR, "Deformation and Damage Mechanisms in High Temperature Composites with Ductile Matrices," Bolling AFB, D.C., March 15, 1991.

AFOSR, "Static and Fatigue Damage in High Temperature Composites," Bolling AFB, D.C., March 15, 1991.

Presentations by Dr. Dvorak (continued)

DARPA HiTASC Program Review, "Thermomechanical Compatibility in High Temperature Composites," March 27, 1991.

First U.S. National Congress on Computational Mechanics, "A New Approach in Nonlinear Micromechanical Analysis of Heterogeneous Media," (with Y.A. Bahei–El–Din and A.M. Wafa), Chicago, Illinois, July 1991.

Invited Lecture at Plasticity '91 at The Third International Symposium of Plasticity and its Current Applications, Grenoble, France, August 12–16, 1991.

Invited Lecture in the Klokner Institute of the Czech Technical University in Prague, "Engineering Education in the United States," Czechoslovakia, August 29, 1991.

Invited Lecture at conference on "New Trends in Structural Mechanics," Institute of Theoretical Applied Mechanics, "Fatigue Damage and Shakedown in Metal Matrix Composite Laminates," Czechoslovak Academy of Science, Prague, September 2, 1991.

American Society of Composites Meeting, "Experimental Evaluation of Yield Surfaces and Plastic Strains in a Metal Matrix Composite," Albany, NY, October 6–9, 1991.

28th Annual Technical Meeting of the Society of Engineering Science, "Fatigue and Shakedown in Metal Matrix Composites," Gainesville, Florida, November 6–8, 1991.

Invited Lecture ASME/WAM, "On Some Exact Results in Thermoplasticity of Composite Material," Atlanta, GA, December 4, 1991.

Invited Lecture ASME/WAM, "Thermal Stresses in Elastic–Plastic Composites with Coated Fibers," Atlanta, GA, December 6, 1991.

Presentations by Dr. Bahei–El–Din

Invited Lecture, Mechanics of Materials Branch, NASA Langley Research Center, Hampton, VA, October 27, 1989.

Third Symposium on Composite Materials: Fatigue and Fracture, American Society for Testing and Materials, "Fracture of Fibrous Metal Matrix Composites Containing Discontinuities," Lake Buena Vista, FL, November 6–7, 1989.

Invited Lecture, Theoretical and Applied Mechanics Department, Cornell University, Ithaca, NY, April 25, 1990.

Invited Lecture, Mechanics of Materials Branch, NASA Langley Research Center, Hampton, VA, September 26, 1990.

AFOSR Program Review, Lt. Col. George Haritos, monitor, Rensselaer Polytechnic Institute, Troy, New York, December 12, 1990.

High Temperature Advanced Structural Composites Program, ONR/DARPA–HiTASC, Rensselaer Polytechnic Institute, Troy, New York, March 8, 1991.

AFOSR Program Review, Lt. Col. Steve Boyce, monitor, Directorate of Aerospace Science, Air Force Office of Scientific Research, Bolling Air Force Base, District of Columbia, March 15, 1991.

Symposium on the Mechanics of Composites at Elevated and Cryogenic Temperatures, ASME Applied Mechanics Division Meeting, Columbus, Ohio, June 16–19, 1991 (two presentations).

First U.S. National Congress on Computational Mechanics, on "Local Stresses in High Temperature Fibrous Composites," Chicago, Illinois, July 21–24, 1991 (two presentations).

Invited Lecture, Mechanics of Materials Branch, NASA Langley Research Center, Hampton, Virginia, January 21, 1992.

Invited Lecture, Aluminum Company of America, Alcoa Technical Center, Pennsylvania, January 22, 1992.

LIST OF PROFESSIONAL PERSONNEL

Dr. G.J. Dvorak – Principal Investigator
Dr. Y.A. Bahei–El–Din – Research Assistant Professor
Dr. H. Nigam – Research Associate
Mr. R.S. Shah – Graduate Student

APPENDIX

Fabrication of Metal Matrix Composite Tubes

for

Rensselaer Polytechnic Institute

Fabrication of Metal Matrix Composite Tubes
for
Rensselaer Polytechnic Institute

February 1992

W. P. Blankenship

F. L. Przywarty

FABRICATION OF METAL MATRIX COMPOSITE TUBES FOR RENSSELAER POLYTECHNIC INSTITUTE

Introduction

Westinghouse Advanced Energy Systems (AES) received an order (Purchase Order No. P31507) from The Department of Civil Engineering, Rensselaer Polytechnic Institute (RPI), on January 30, 1990 to fabricate tungsten-fiber-reinforced superalloy-matrix composite tubes for structural behavior studies. The original scope of work was defined as follows:

Specifications:

- o Matrix Material: Nickel base superalloy
- o Reinforcement Fiber: GE-3D* lamp filament, 0.006-inch dia.
- o Fiber Volume Fraction: 0.35
- o Tube O.D.: 1.25 ± .025 inches
- o Plies: 2 to 5 (as determined by degree of difficulty of assembly)
- o Tube Length: 15 inches
- o Fiber Orientation: Parallel to tube axis

Articles To Be Fabricated:

- o One short (4- to 6-inch) "prototype" composite tube to verify assembly and hot isostatic pressing (HIP) procedures. Evaluation to be via metallographic examination.

- o Two 15-inch long composite tubes, fabricated using the above procedures and examination as a guide. Inspection to be via metallographic examination of samples taken from tube ends. Nondestructive examination not included.

Basis of Supply: Product-of-best-effort.

----

* Changed to GE-218...see below.

Based on our existing experience in fabricating flat panels of tungsten-fiber-reinforced superalloy-matrix composites, the choice of matrix material was limited to the iron-base alloy Incoloy 907 and the nickel-base alloy Waspaloy. In telecon discussions between Mr. R. L. Ammon of AES and Dr. Y. A. Bahei-El-Din of RPI, Waspaloy[*] was selected as the material to be used for the composite tubes.

Upon attempting to purchase 0.006-inch diameter GE-3D lamp filament from General Electric, it was determined that this material was not available in the context of the project schedule. It was therefore agreed between Mr. Ammon and Dr. Bahei-El-Din that GE-218 filament would be used instead. It originally appeared as if the latter would only be available in 0.008-inch diameter, but eventually 0.006-inch diameter GE-218 filament was obtained.

Design and Fabrication of Prototype No. 1

Previously-fabricated Waspaloy matrix composite panels were assembled from monotapes in which matrix material was arc-sprayed on both sides of the fiber. Approximately 60 percent of the matrix material was sprayed on the first side and 40 percent on the opposite side. This produced a flat and stress-free monotape for layup into a composite panel. A monotape made in this manner is not flexible enough to be formed into a small diameter tube and would readily split. Through experience in removing from the deposition drum a monotape which had only the first side sprayed, it was known that (due to residual stresses) the monotape would curl into a tubular shape. To take advantage of this effect in the subject work, all monotapes used in fabricating composite tubes were arc sprayed on just one side of the tungsten fibers. The single problem that resulted was that the outer monotape forming the composite tube would have exposed fibers at its outer surface. The solution was to arc spray a Waspaloy foil (without reinforcement) and add this layer to form the outermost portion of the composite tube.

----

[*] Composition: Ni-19.5Cr-13.5Co-4.3Mo-3.0Ti-2.0(max)Fe-1.4Al

The proposed approach to fabricating the composite tubes was to build an assembly of concentric monotape and foil layers, encapsulate this assembly in a hermetically sealed annular package bounded by inner and outer stainless steel pipes or tubes, evacuate and seal off the package via an evacuation tube, and consolidate the assembly by hot isostatic pressing (HIP). To verify the adequacy of the detailed assembly method and HIP consolidation cycle, a sublength composite tube designated Prototype No. 1 was fabricated.

The first step in this fabrication was the production of monotapes and foils. To produce a monotape, the reinforcing fiber was wrapped at the required pitch on a 16-inch diameter x 20-inch long aluminum drum which was mounted in a custom-built wire wrapping lathe. Appropriate tension for the given reinforcing wire diameter was maintained by an electrically controlled clutch. Prior to wrapping, a release agent was applied to the drum surface to prevent adherence of arc-sprayed metal. A monotape of 35 volume percent reinforcement using 0.006-inch diameter wire requires a wrapping pitch of 0.009 inches. Typically, monotape widths of approximately 5 inches were wrapped which required wire spools containing about 765 yards (700 meters) of GE-218 lamp filament.

Upon completion of the wire wrapping operation, the drum was removed from the lathe and transferred to the arc spray chamber. The drum was mounted to the shaft of a rotational/translational positioning system which protrudes into the chamber through the center of its door. The door was closed, the chamber evacuated and backfilled with an argon - 5 percent hydrogen arc spray atmosphere, and a continuous gas purge initiated. The spray gun valve was opened and the gun inserted to the desired standoff distance from the drum. Arc spraying of the matrix alloy was then initiated, with the drum being rotated and translated under the stationary arc spray gun. Multiple passes (translations) were performed to produce monotape having the required amount of deposited matrix alloy.
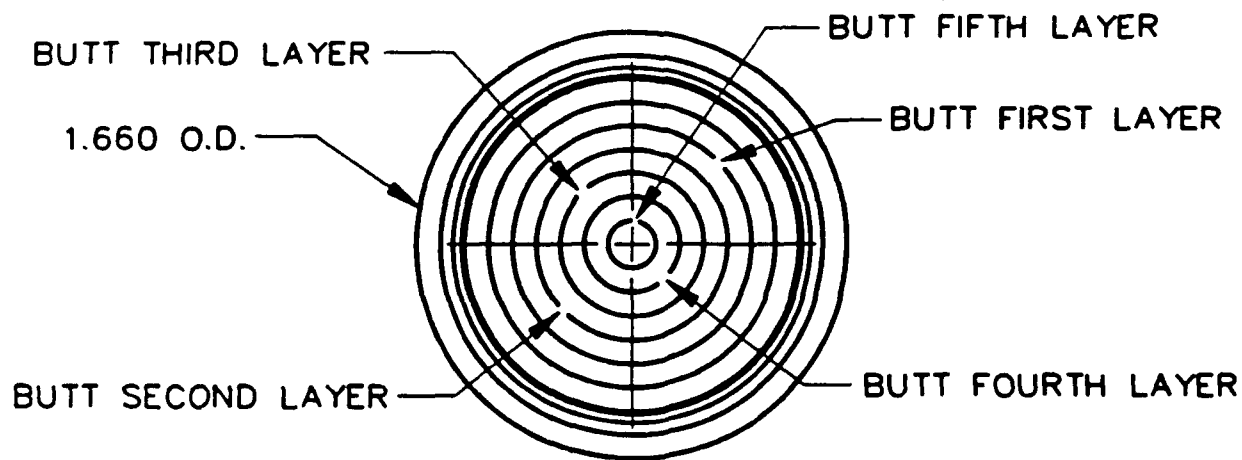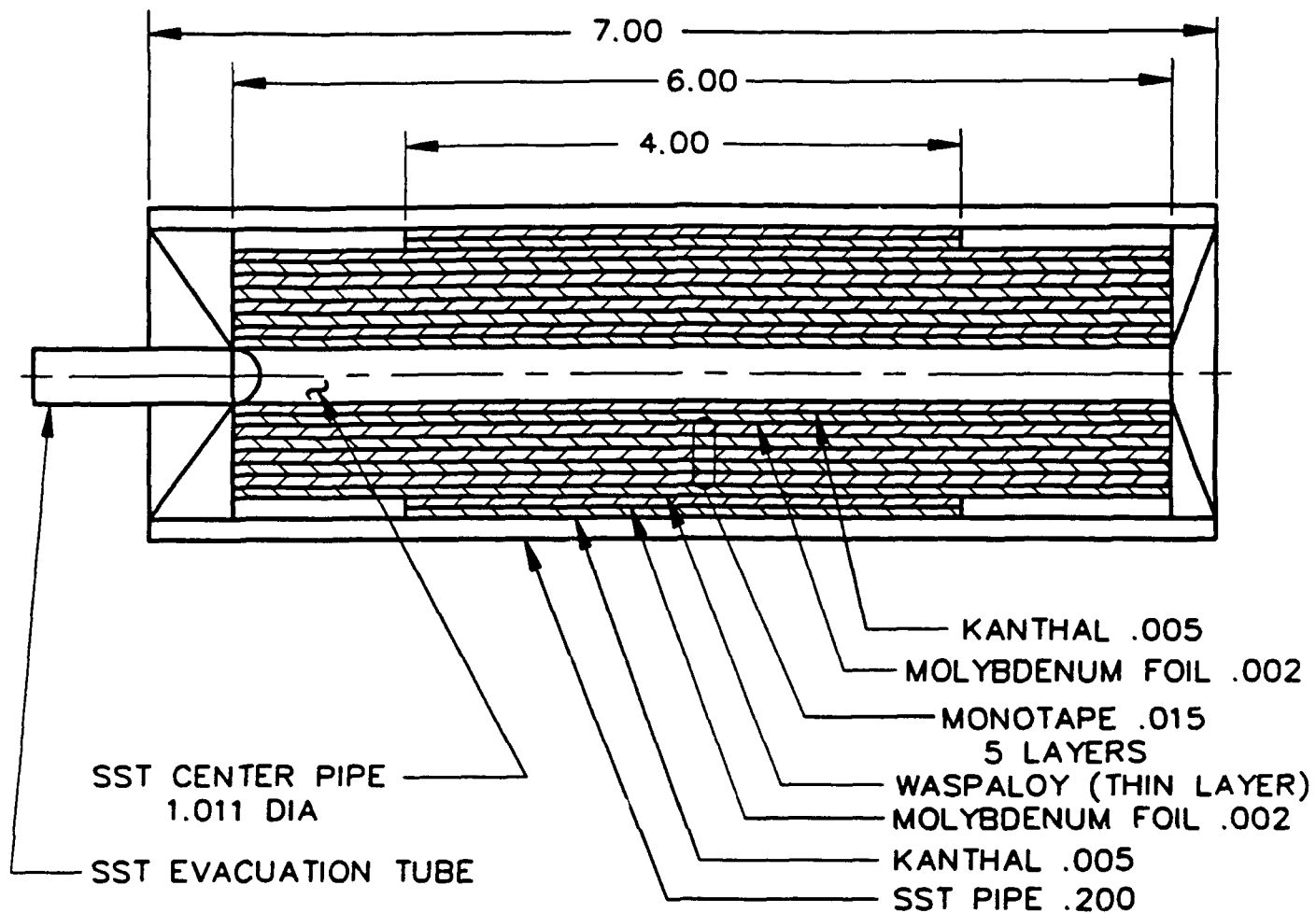
Production of Waspaloy foil layers was similar to that described above for monotape, except that no fiber was involved and the Waspaloy was sprayed directly onto a roughened, release-layer-coated carbon steel sheet wrapped around the circumference of the deposition drum.

Typical arc spray parameters used to produce the monotapes were:

o Matrix wire: 0.045-inch diameter Waspaloy
o Wire feed rate: 190 inches/minute
o Voltage: 38 volts
o Current: 120 amps
o Gun standoff distance: 5 inches
o Spray pressure: 60 psi
o Rotation speed: 60 rpm
o Translation speed: 10 inches/minute
o Gas: Argon - 5 percent hydrogen

Upon completion of arc spraying the material cooled, the chamber opened
and the monotape or foil surfaces vacuumed to remove any fine metal dust
particles. The drum was then removed from the chamber, and turnbuckles on
each side adjusted to contract its O.D., releasing the tension on the
deposited layer. The layer was then cut from the drum using an air driven
abrasive disc cutter. The product was then visually inspected, weighed,
dimensioned and its reinforcement volume fraction verified by calculation.

The design of the HIP package for fabrication of Prototype No. 1 is shown
schematically in Figure 1. The package was assembled using standard T304
stainless steel inner and outer pipe sizes. Layers of Fe-Cr-Al (oxidized
Kanthal A) and Mo foil were used to prevent bonding of the composite
layers to the stainless steel envelope. A subassembly consisting of the
outer Fe-Cr-Al, Mo and Waspaloy foil and outer monotape layers was
inserted into the I.D. of the outer pipe first, followed by successive
monotape layers filling toward the center. The five layers of monotape
were sized to form cylinders with butt joints; i.e, no overlapping was
employed. Inner Mo and Fe-Cr-Al foil layers were then added, and the O.D.
of the inner pipe was swaged to fit the remaining opening and inserted
last. The ends of this inner pipe were flared to meet the outer pipe and
seal welded together, along with an evacuation tube at one end. As was
shown in Figure 1, the outer Fe-Cr-Al and Mo layers were shortened to
allow one inch of composite/stainless steel contact at each end. This was
done to investigate whether diffusion bonding of the composite to the
outer pipe would permit the machining of strong, integrally bonded tensile
grips into the ends of the outer pipe after consolidation.

7.00

6.00

4.00

KANTHAL .005
MOLYBDENUM FOIL .002
MONOTAPE .015
5 LAYERS
WASPALOY (THIN LAYER)
MOLYBDENUM FOIL .002
KANTHAL .005
SST PIPE .200

SST CENTER PIPE
1.011 DIA

SST EVACUATION TUBE

BUTT THIRD LAYER

BUTT FIFTH LAYER

1.660 O.D.

BUTT FIRST LAYER

BUTT SECOND LAYER

BUTT FOURTH LAYER

FC20103-05

Figure 1.   Prototype No. 1, HIP Package Schematic.

-5-

The resultant HIP package was evacuated and internally outgassed at 550°F. It was then successfully leak tested using a mass spectrometer leak detector, and the evacuation tube sealed off by welding. The completed package is shown in Figure 2. It was then consolidated in a 2100°F - 30,000 psi - 20 minute HIP cycle. The parametric configuration of the HIP cycle is shown in Figures 3a and 3b, and the as-HIP'd Package is shown in Figure 4.

The consolidated HIP package was machined to remove the inner pipe and the center 4 inches of the outer pipe (down·to the composite surface), as shown in Figure 5. This left in place the one-inch end sections of the outer stainless steel pipe which were diffusion bonded to the composite tube. The I.D. and exposed 4-inch section on the O.D. of the composite tube were glass bead blasted and etched to remove any traces of adherent Mo foil. A 1.25-inch long end section was cut off and its ends surface ground parallel to one another and perpendicular to the tube axis. This section was then used to evaluate the strength of the composite/stainless steel diffusion bond. The data from this evaluation is shown in Table 1.

Table 1. Strength of Composite/Stainless Steel Diffusion Bond

Bond Region Dimensions: 1.22 inch diameter x 0.908 inch long

Bond Area: 3.48 in^2

Load (pounds)	Stress (psi)	Deflection (inches)
0	0	0.0000
5500	1580	0.0140
11000	3161	0.0296
16500	4741	0.0450
22000	6322	0.0604
27500	7902	0.0760
33000	9483	0.0920

(Note: Sample did not fail at 33,000 pounds)

Figure 2. Prototype No. 1 HIP Package, As-Fabricated.

-7-
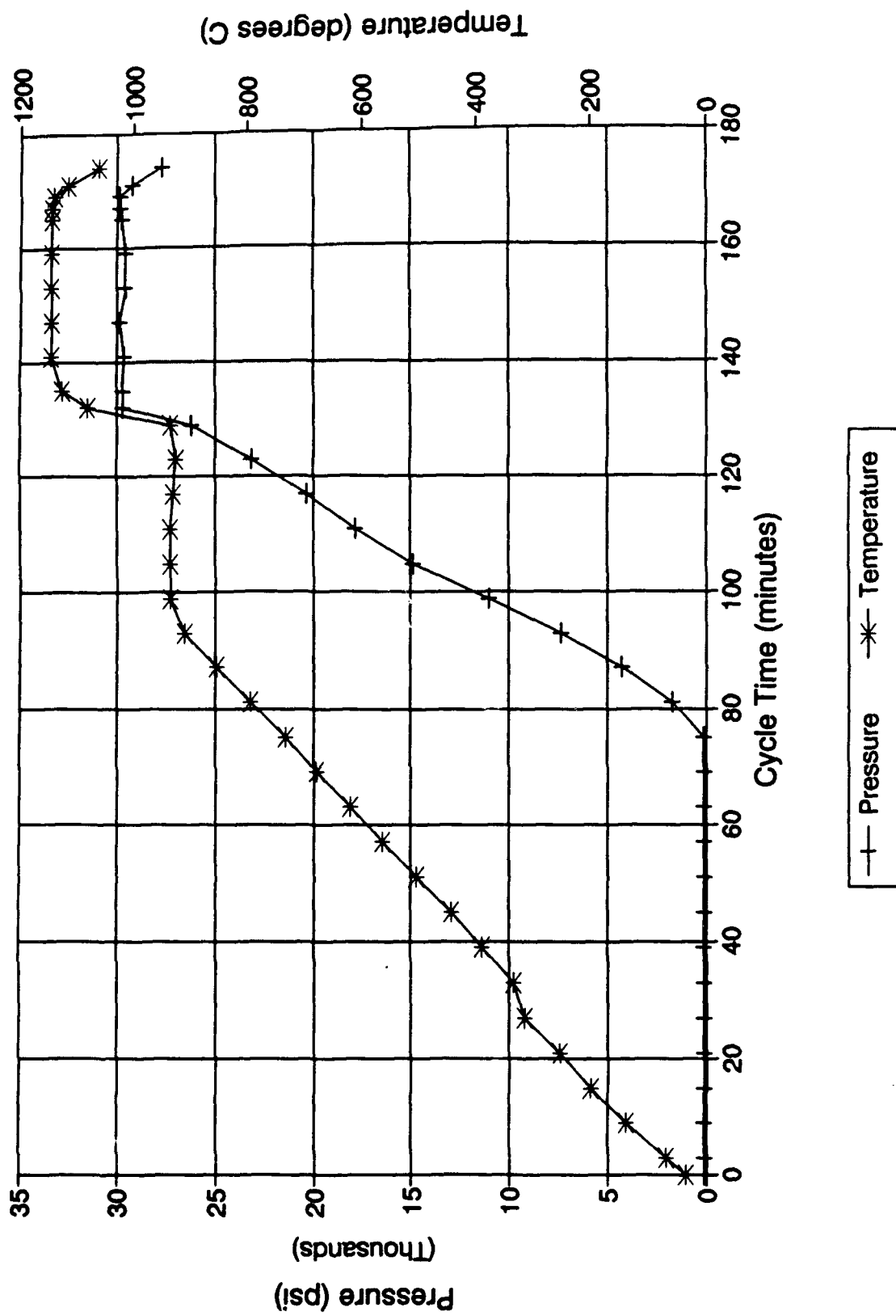
Figure 3a. Prototype No. 1, HIP Cycle Pressure/Temperature vs. Time.
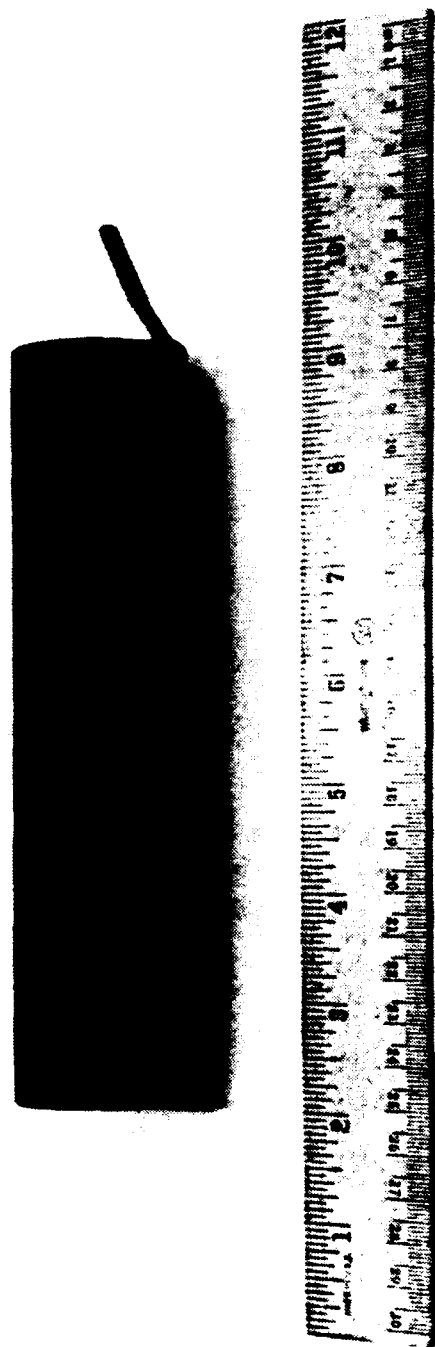
-8-

Figure 3b. Prototype No. 1, HIP Cycle Temperature vs. Pressure.
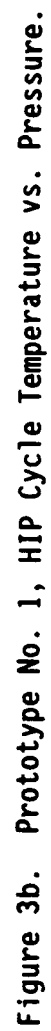
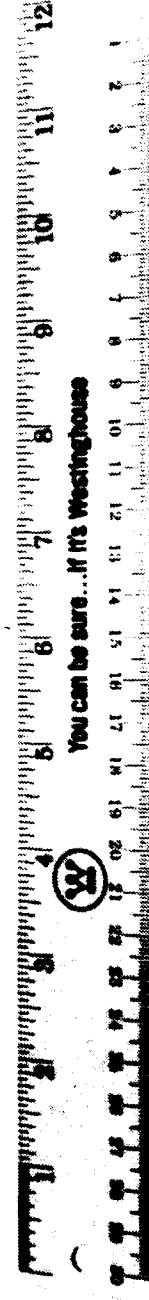Figure 4.   Prototype No. 1 HIP Package, As-Consolidated

-10-

Figure 5. Prototype No. 1, As-Machined.

The opposite face of the composite tube at the sectioning cut was metallographically prepared and polished. Photographs of the microstructure are shown in Figure 6. The cross section shows several areas in which serious anomalies exist in the composite structure. Areas are seen where fewer than the as-assembled five uniform rows of tungsten fibers are present, and severe localized tube wall thinning is present at two of these locations. These results were attributed to some combination of local yielding plus butt joint opening due to the HIP cycle pressure applied to the tube I.D., with adjacent layers filling in the voids in the latter case.

Dimensional measurements on the composite tube revealed it to be out-of-round. The O.D. ranged from 1.210 to 1.240 inches, while the I.D. range was 1.118 to 1.149 inches. (A check with the HIP vendor revealed that the tube had been loaded horizontally in the HIP unit, and its cross section may have sagged at temperature). The composite tube wall thickness was nominally 0.046 inches, representing an approximate 39 percent reduction of the original 0.075 inch thickness of the five monotape layers prior to consolidation.

Based on the above, the deficiencies in Prototype No. 1 are summarized below:

o   Cross section out-of-round.

o   Localized anomalies in reinforcement layers.

o   Localized tube wall thinning.

In view of these deficiencies, it was decided in telecons between W. P. Blankenship of Westinghouse and Dr. Bahei-El-Din that a second prototype should be designed and fabricated in order to verify the proposed approaches to their elimination. This is described in the following section.
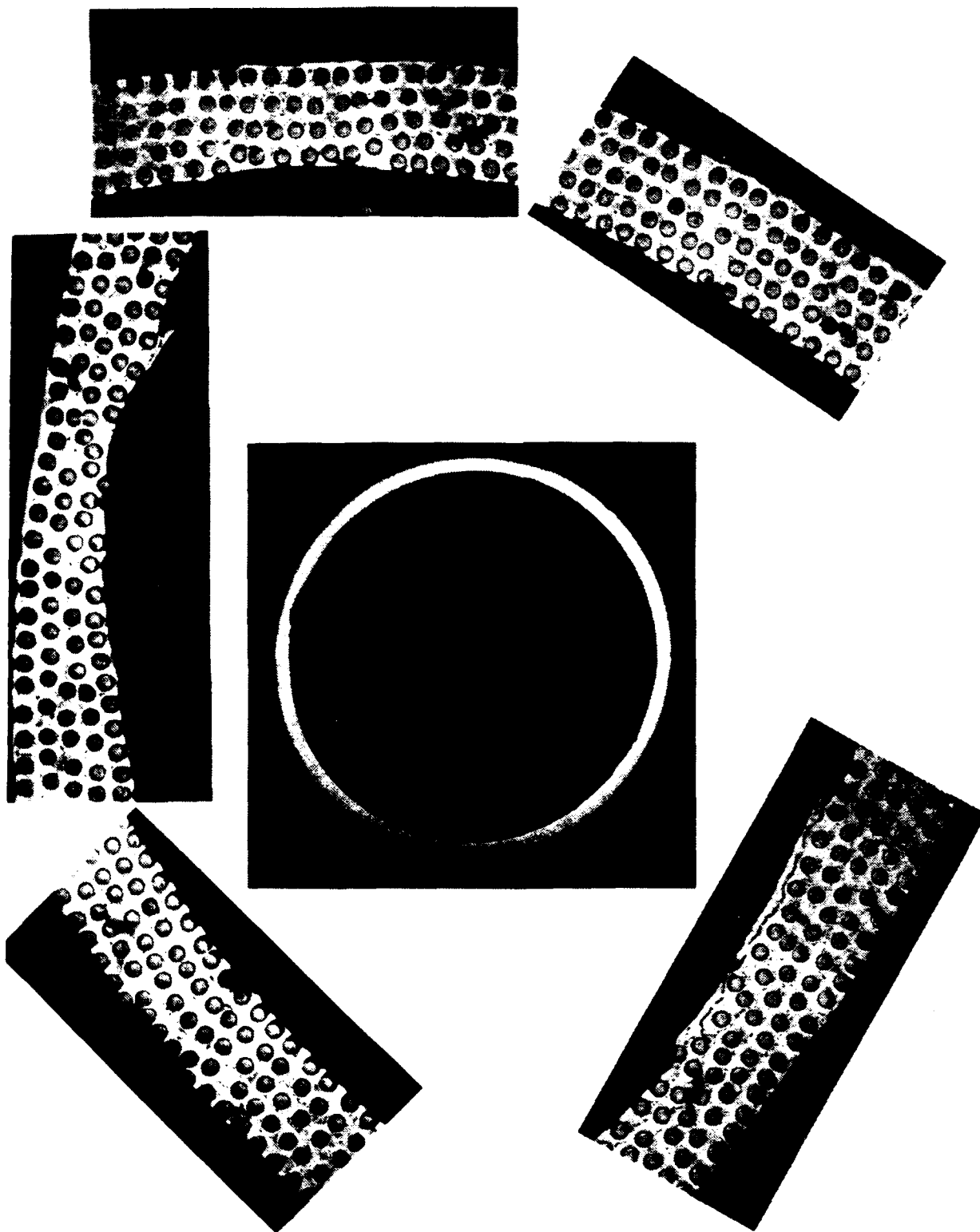
Figure 6. Prototype No. 1, Cross Section Microstructural Details.
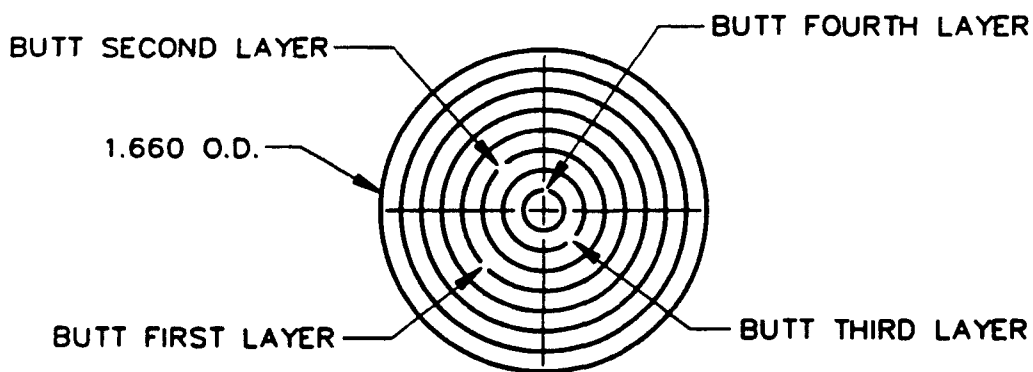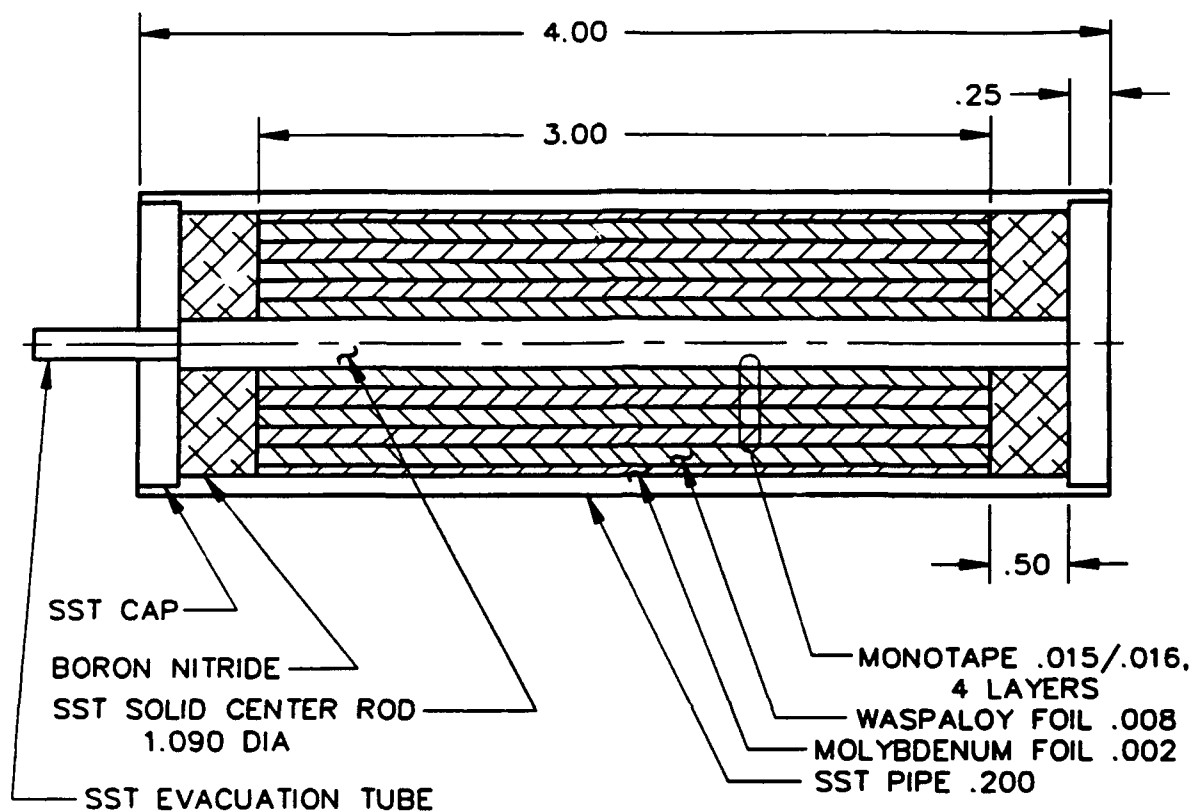
Design and Fabrication of Prototype No. 2

A second but smaller prototype was designed incorporating ideas for a simpler and more viable configuration. By careful layout, short 3-inch long sections were cut from the monotapes already produced for the fabrication of the 15-inch long deliverable tubes. In this manner a 4-ply prototype could be fabricated without incurring additional material or arc spraying costs. The configuration of the Prototype No. 2 HIP package is shown in Figure 7.

This new configuration utilized the same size outer stainless steel pipe used for Prototype No.1 but eliminates the inner and outer layers of Fe-Cr-Al foil and the inner layer of Mo foil. To permit modifying the consolidation process, the inner package member was changed to a solid stainless steel rod which was coated with a 0.0005-inch layer of Mo by electron beam vapor deposition. This would constrain the HIP cycle pressure to be applied only to the outer surface and ends of the package, thus ensuring inward consolidation. The rod and the outer 0.002-inch Mo foil were painted with a Y_2O_3 slurry to help prevent diffusion bonding. The ends of the outer pipe were counterbored to receive simple stainless steel discs as end closures. An evacuation tube was welded into the center of one end disc. The boron nitride rings were added to facilitate decladding of the composite tube after consolidation.

Assembly of the package was similar to that of Prototype No. 1, with the outer layers inserted into the envelope first and successive layers filling toward the center. The innermost monotape and center rod were inserted together to prevent scraping the Y_2O_3 coating off the rod. Inserting the boron nitride rings and stainless steel discs completed the assembly.

After welding the end closures, the package was evacuated and outgassed at 550°F, successfully leak tested and sealed off. It was then loaded vertically in the vendor's HIP unit and consolidated in a 2100°F - 29,000 psi - 20 minute HIP cycle. The detailed parametric configuration data for this cycle is not available.

4.00

3.00

.25

.50

SST CAP

BORON NITRIDE

SST SOLID CENTER ROD
1.090 DIA

SST EVACUATION TUBE

MONOTAPE .015/.016,
4 LAYERS
WASPALOY FOIL .008
MOLYBDENUM FOIL .002
SST PIPE .200

BUTT SECOND LAYER

BUTT FOURTH LAYER

1.660 O.D.

BUTT FIRST LAYER

BUTT THIRD LAYER

FC20103-04

Figure 7.   Prototype No. 2, HIP Package Schematic.

-15-

The consolidated package was machined to remove the stainless steel and boron nitride end rings and provide access to the center rod ends. Gripping the rod ends in a lathe collet permitted machining the outer surface concentric to the I.D. of the composite tube. All of the outer pipe was machined in this manner, and the center rod was then removed. Decladding was simple and straightforward, due to the utilization of the Y_2O_3 release coating. The resultant composite tube was glass bead blasted and etched in the same manner as Prototype No. 1. The tube is shown in the as-etched condition in Figure 8.

Dimensional measurements indicated the tube O.D. to range from 1.177 to 1.180 inches, with a uniform wall thickness of 0.040 inches. This represents a 43% reduction from the original 0.070 inch thickness of the four monotapes plus outer layer of Waspaloy foil.

Two 0.3-inch long samples were sliced from one end of Prototype #2. One was left unmounted and used for visual examination of the tube inner surface. No evidence of ply separation was seen, and the tube interior was smooth and continuous. The other section was mounted and polished for metallographic examination. A montage of macrophotographs of this section is shown in Figure 9. Localized perturbations in the tube wall are visible at the locations marked A, B, and C. Location A shows a perturbation in the butt joint of (outer) Ply No. 4, which is shown at higher magnification in Figure 10. Location B is the butt joint of Ply No. 3 which is deficient in fibers in this area. A higher magnification view of this area is shown in Figure 11. A similar condition in Ply No. 2 occurred at Location C. In general, the tube wall thickness is uniform and free of voids in the matrix. A high magnification photograph of a typical unperturbed region is shown in Figure 12.

Tungsten fiber splits that propogate into the Waspaloy matrix (or vice-versa) were seen at one location in Ply No. 1, as shown in Figure 13. This phenomenon, caused by differential thermal expansion between the tungsten fiber and Waspaloy matrix during cooldown in the HIP cycle, has been observed previously in flat composite panels of similar composition. A method for eliminating such splits has been developed for flat panel geometry, but an analogous method for tubular geometry does not exist at present.

2nd PROTOTYPE TUBE
4 Ply Waspaloy/Tungsten
35 v/o Wire Reinforcement

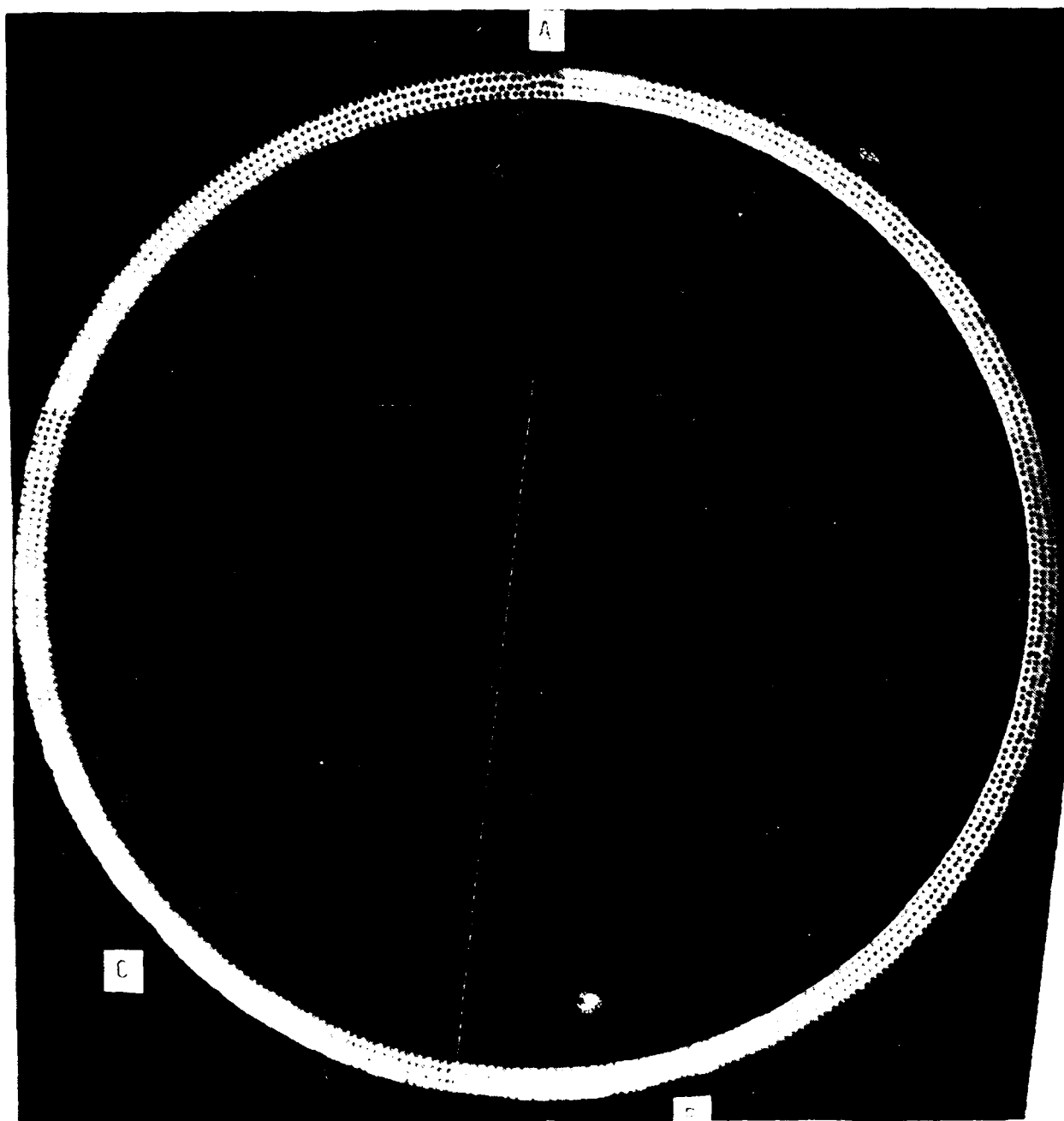Figure 8. Prototype No. 2, As-Decladded and Etched.

-17-

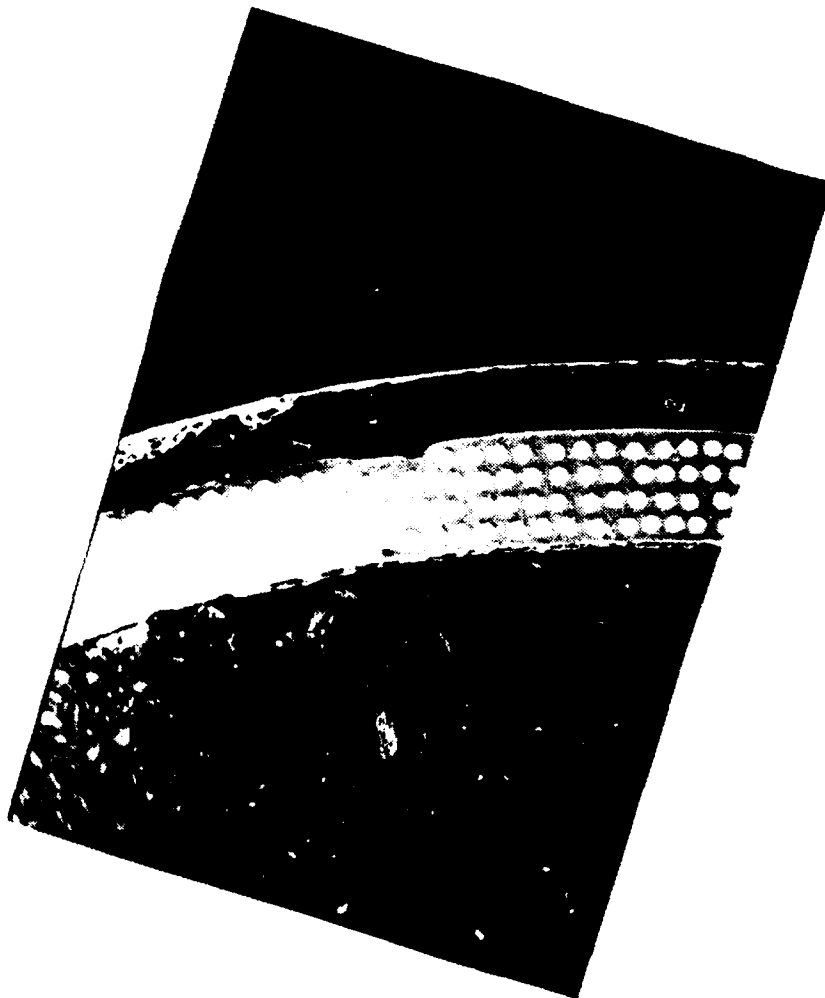Figure 9. Prototype No. 2. Cross Section Microstructure.

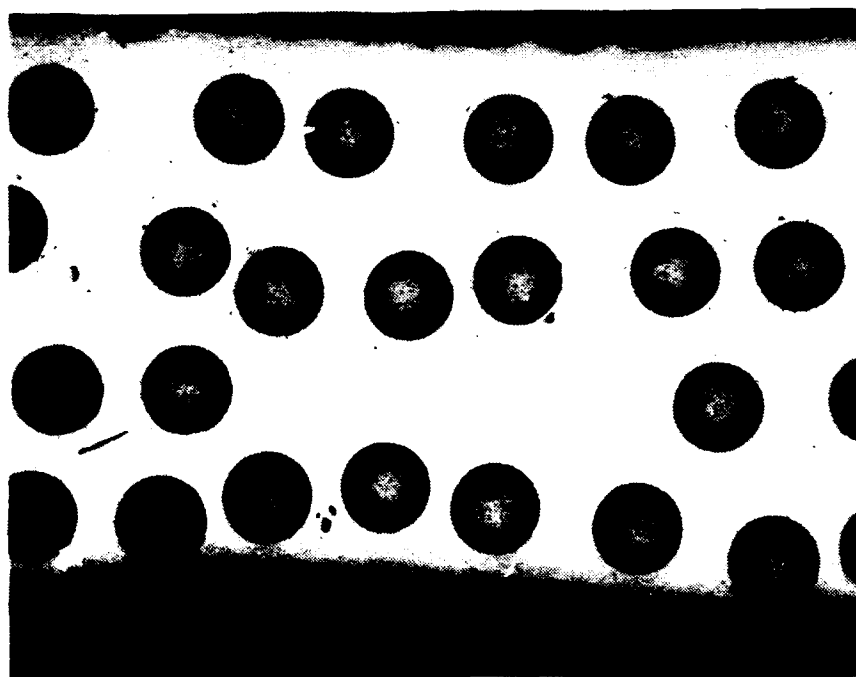Figure 10. Prototype No. 2, Microstructural Details at Location A (20X).

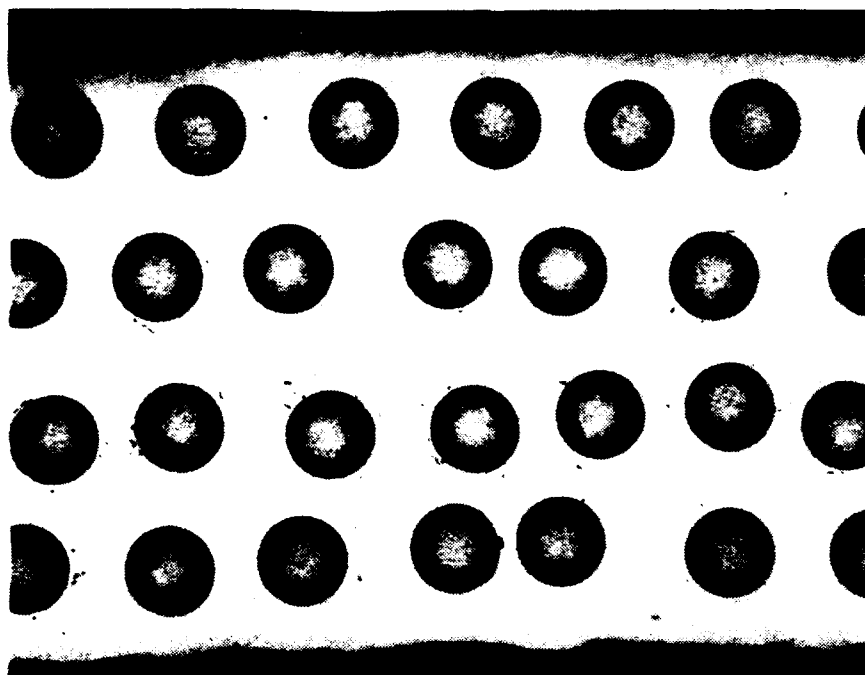Figure 11. Prototype No. 2, Microstructural Details at Location B (80X).

Figure 12. Prototype No. 2, Microstructural Details of
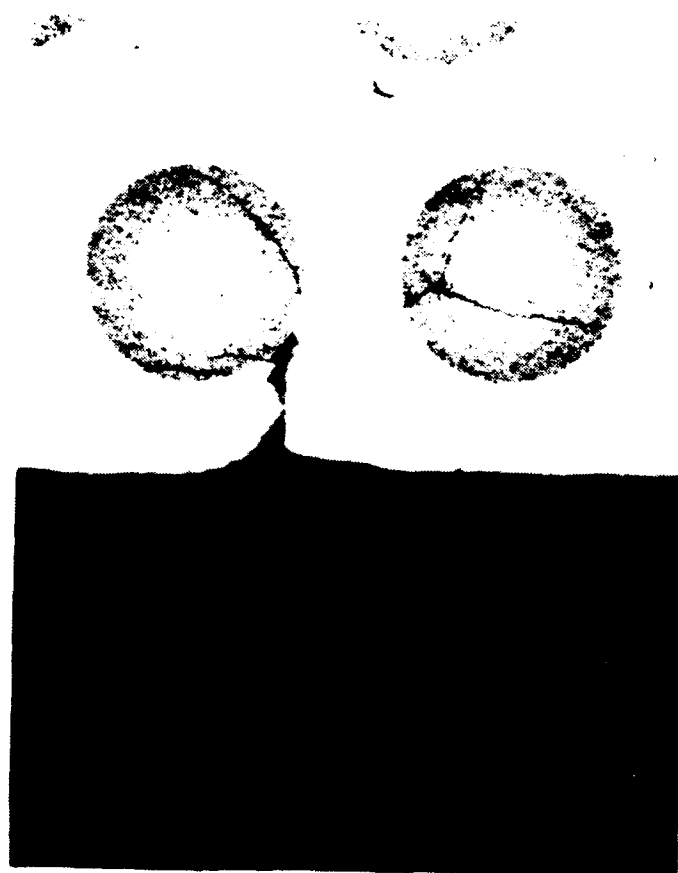Typical Unperturbed Region (80X).

Figure 13.   Prototype No. 2, Tungsten Fiber Splits in Ply No. 1 (200X).

The tungsten/Waspaloy interdiffusion reaction zone developed during HIP is seen for a typical fiber in Figure 14. The zone thickness, nominally 0.0001 inches, is within the range of acceptability for achieving good fiber/matrix bonding without developing brittle intermetallic characteristics.

From the above evaluation, it was concluded that a major improvement in composite tube structural uniformity and freedom from serious perturbations had been achieved with the Prototype No. 2 assembly and processing approach. However, it is doubtful that complete freedom from localized perturbations can ever be achieved with an assembly of individual butt-jointed plies. A multiple-ply spiral wrap assembly made from a single continuous width monotape might yield superior results, but fabricating a superalloy matrix monotape of such width is beyond the capability of our state-of-the-art methodology.

A meeting was held at RPI on December 12, 1990 to review the status of the project. A presentation was made detailing the results of the first two prototype tubes and noting the inescapable trial-and-error nature of this first-of-a-kind project. Agreement was reached on the approach to be taken in fabricating full length deliverable tubes, and that the scope would be modified to require delivery of only one 15-inch product. The key change to be implemented was to overlap the outer monotape a small amount (5 or 6 fibers) to eliminate the perturbation on the O.D. of the composite tube. At the same time, it was agreed that the scope of work would be expanded to include fabrication of a flat panel of Waspaloy foil to permit RPI to fabricate and test samples of unreinforced matrix material.
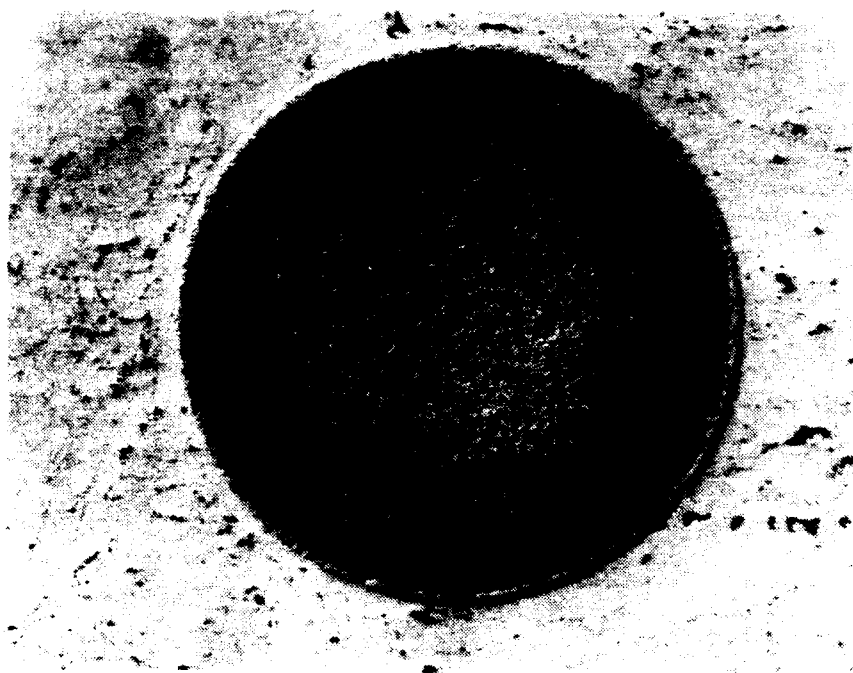
Figure 14. Prototype No. 2, Typical Tungsten Fiber/Waspaloy
Matrix Interdiffusion Reaction Zone (500X).

Design and Fabrication of Tube No. 1 and Waspaloy Panel

The design of (full length) Tube No. 1 was based on the results obtained with Prototype No. 2 and additional details specified by RPI in the sketch of Figure 15. The design of the HIP package is shown schematically in Figure 16. To promote diffusion bonding of the outer stainless steel pipe to the composite tube ends while precluding such bonding over the 6-inch center test section, a 6-inch long layer of 0.001-inch Mo foil, coated with Y_2O_3, was positioned as shown 4 inches from one end of the pre-cut outer Waspaloy foil layer, and the two inserted as a unit into the outer pipe. The outer monotape ply was cut to allow 0.050 to 0.060 inches of joint overlap to preclude development of a groove in the composite outer layer. All other monotapes were butt jointed with the joint locations staggered around the tube circumference. The inner stainless steel rod was turned to an O.D. of 1.054 inches and then plasma sprayed with a Mo release layer. The Mo was sanded back to a thickness of 0.001 inches and coated with Y_2O_3. The inner monotape layer and the center rod were then assembled together and inserted as a unit to prevent scraping the coating off the rod. Inserting the boron nitride rings and stainless steel discs completed the assembly. After welding the end closures, the package was evacuated and outgassed at 550°F, successfully leak tested and sealed off.

A sheet of 0.017-inch thick Waspaloy foil was arc sprayed using the parameters previously listed. It was cut into 5 x 8 inch sheets, 5 of which were stacked, sandwiched between Mo pressing platens and encapsulated by welding into a HIP package made of stainless steel sheet and an evacuation tube. The resultant package was evacuated and outgassed at 550°F, successfully leak tested and sealed off.

The tube and panel packages were loaded vertically in the vendor's HIP unit and consolidated in a 2100°F - 30,000 psi - 20 minute HIP cycle. The parametric configuration of this cycle is shown in Figures 17a and 17b, and the as-HIP'd packages are shown in Figure 18.

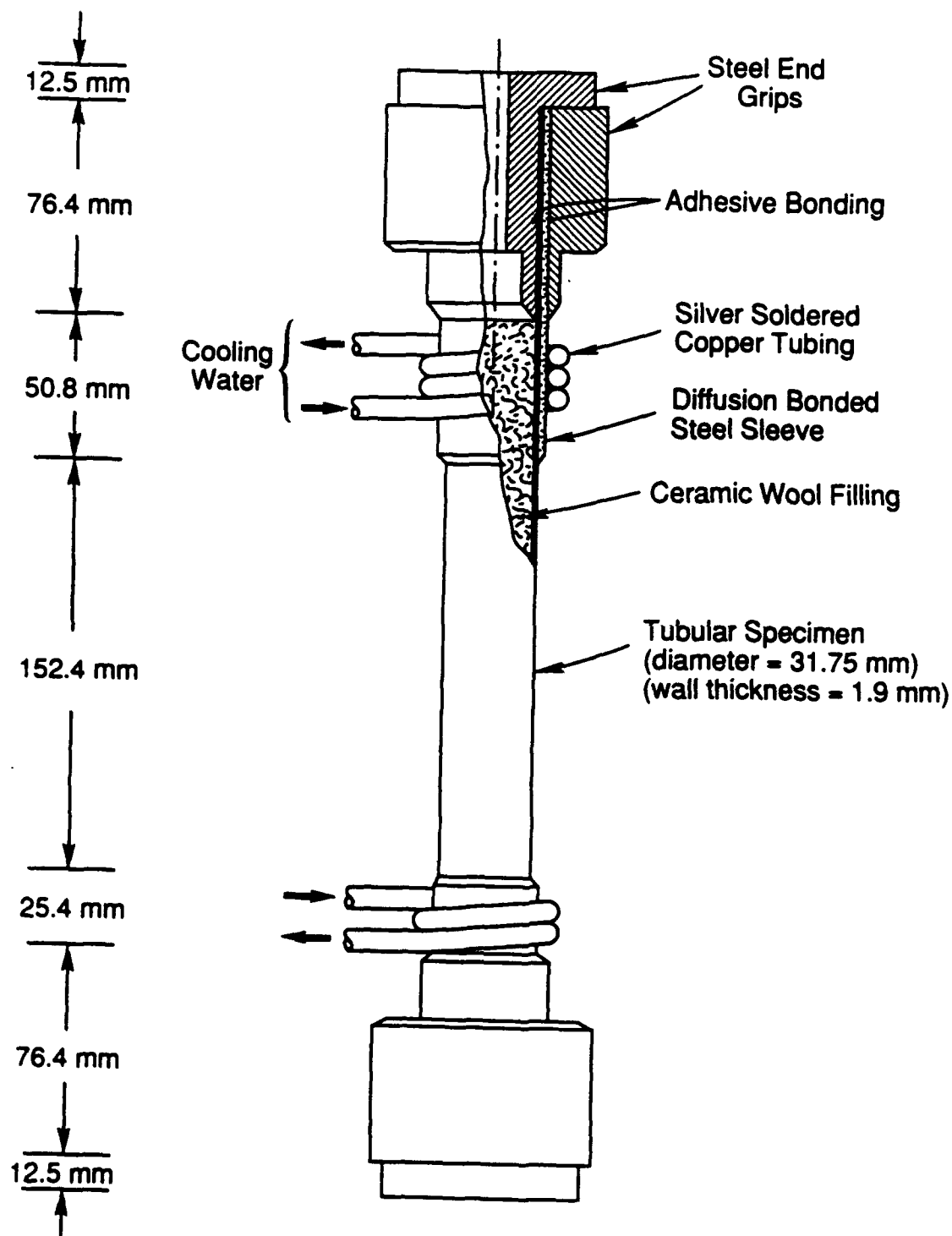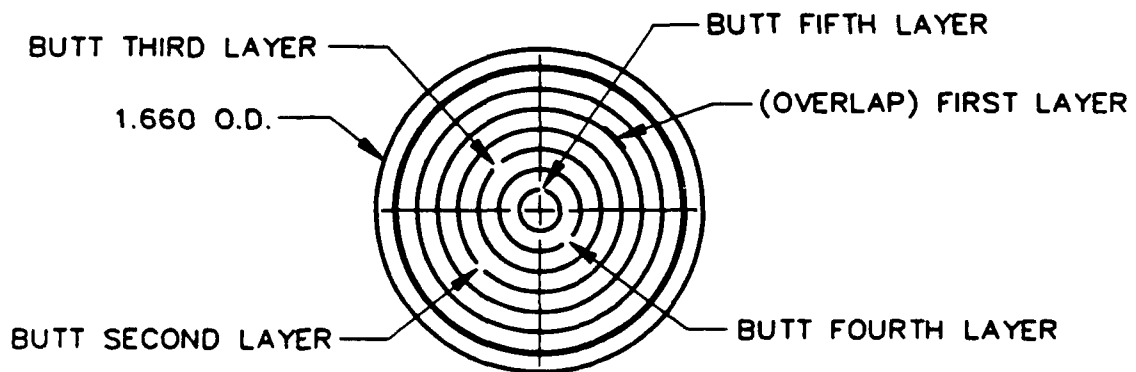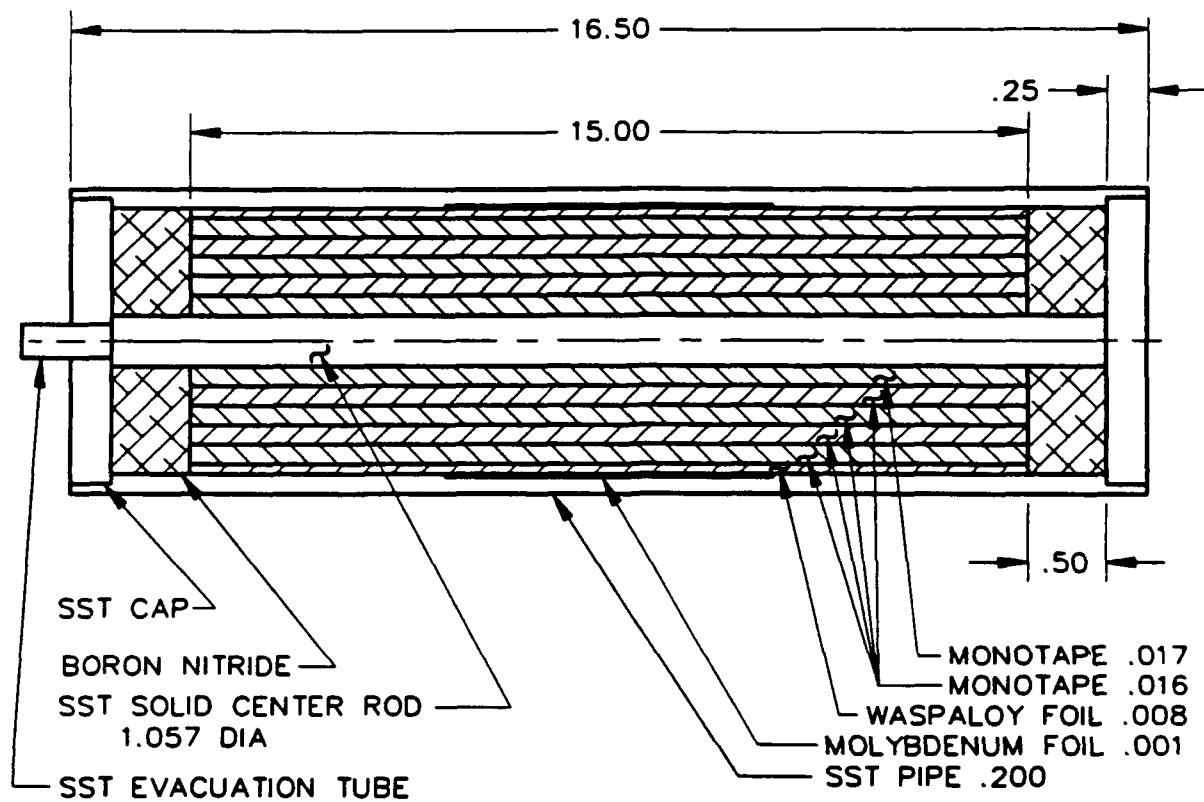# Geometry of the Waspaloy-Tungsten Composite Specimen with Grips and Cooling Arrangement

12.5 mm

76.4 mm

50.8 mm

152.4 mm

25.4 mm

76.4 mm

12.5 mm

Steel End Grips

Adhesive Bonding

Cooling Water

Silver Soldered Copper Tubing

Diffusion Bonded Steel Sleeve

Ceramic Wool Filling

Tubular Specimen
(diameter = 31.75 mm)
(wall thickness = 1.9 mm)

Figure 15.   Tube No. 1, Design Details and Test Arrangement.

16.50

15.00

.25

.50

SST CAP

BORON NITRIDE

SST SOLID CENTER ROD
1.057 DIA

SST EVACUATION TUBE

MONOTAPE .017
MONOTAPE .016
WASPALOY FOIL .008
MOLYBDENUM FOIL .001
SST PIPE .200

BUTT THIRD LAYER

BUTT FIFTH LAYER

1.660 O.D.

(OVERLAP) FIRST LAYER

BUTT SECOND LAYER

BUTT FOURTH LAYER

FC20103-01

Figure 16.   Tube No. 1, HIP Package Schematic.
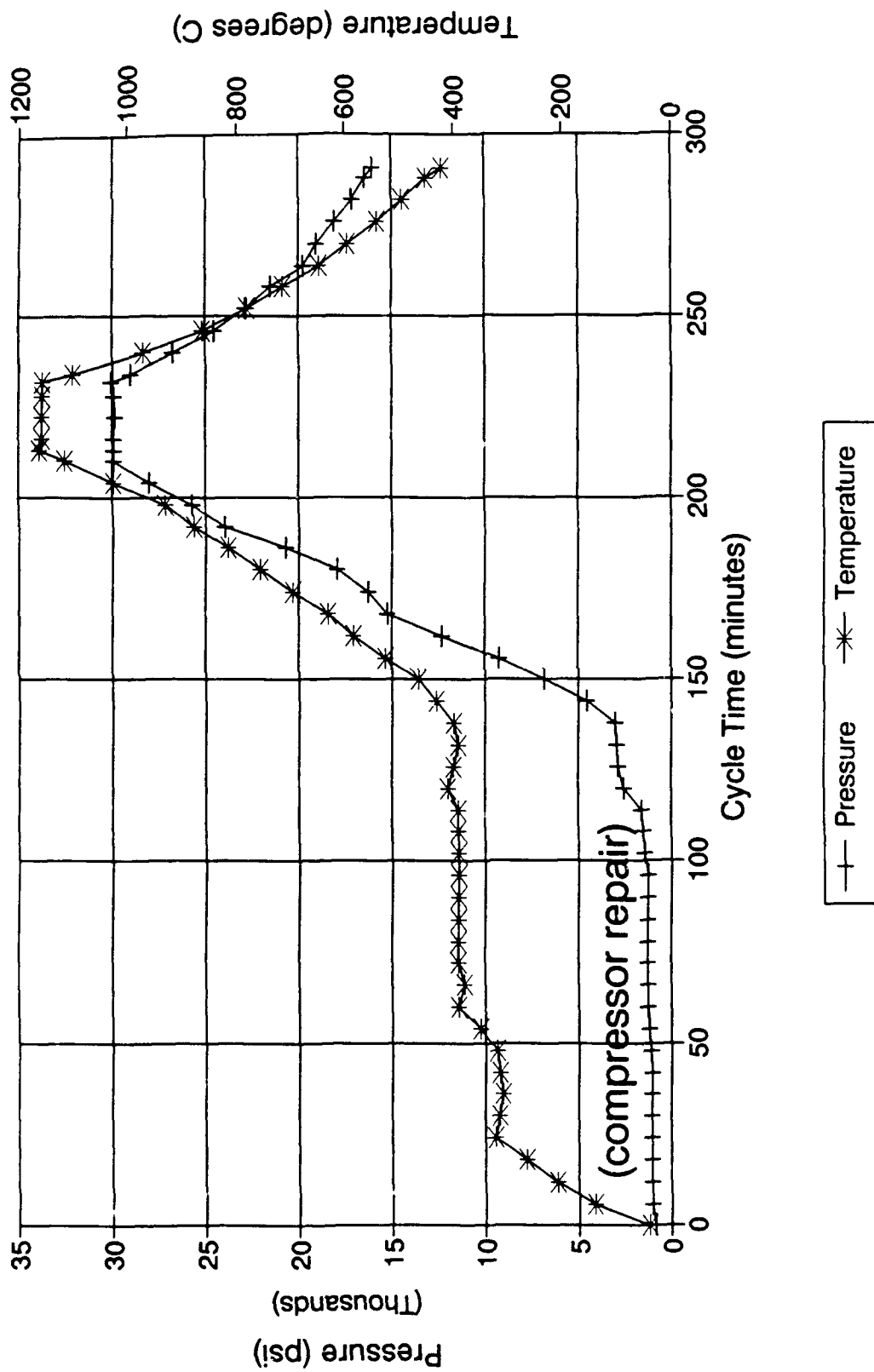
Figure 17a. Tube No. 1, HIP Cycle Pressure/Temperature vs. Time.
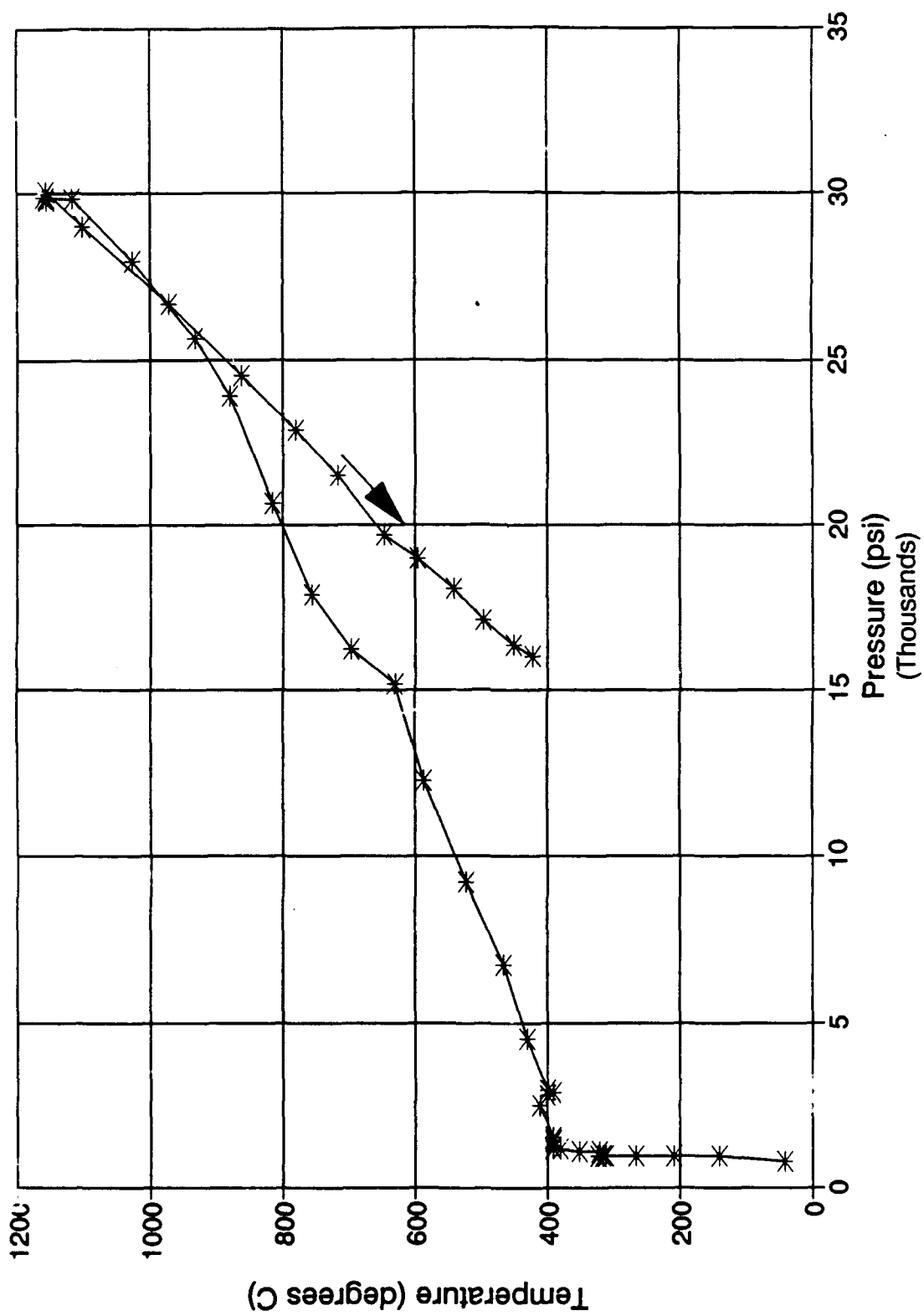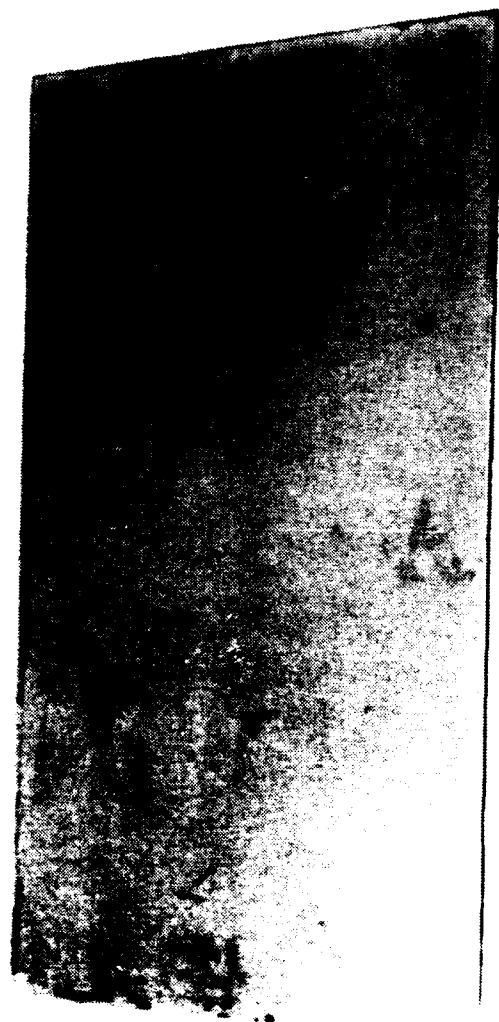
Figure 17b. Tube No. 1, HIP Cycle Temperature vs. Pressure.

-29-
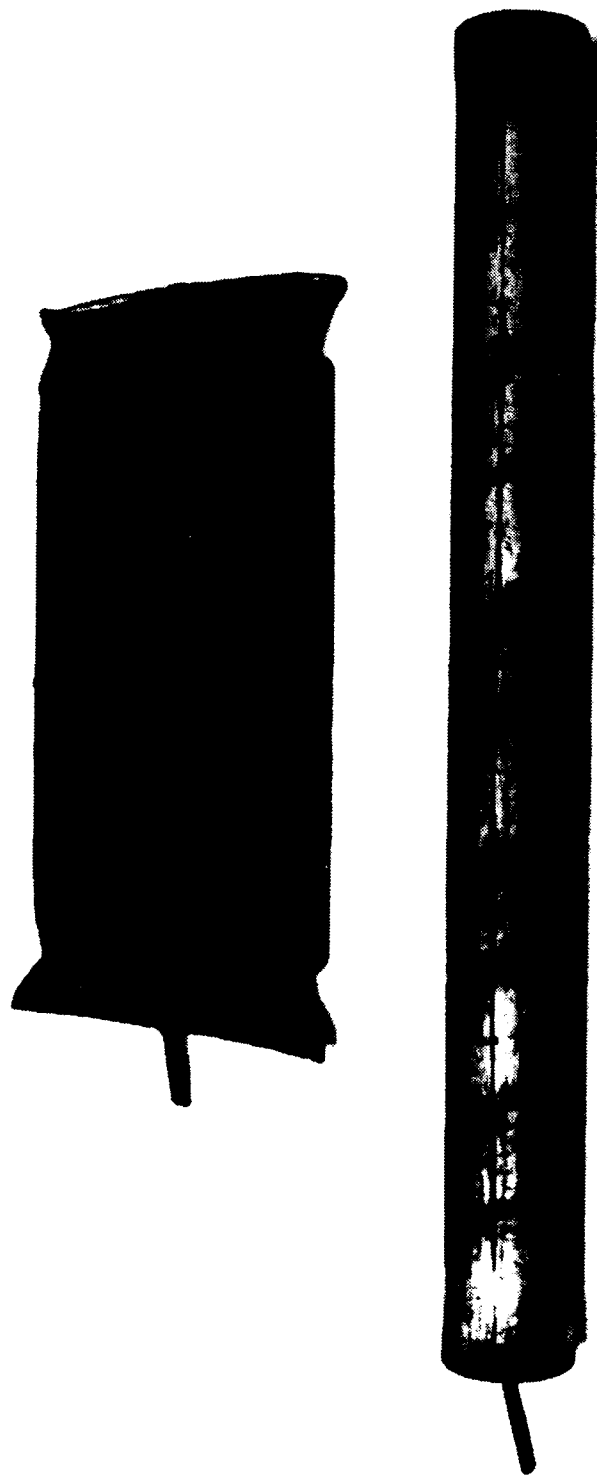
Figure 18. Tube No. 1 and Waspaloy Panel HIP Packages, As-Consolidated.

The panel package envelope was machined away in a straigtforward manner to yield the flat panel of unreinforced Waspaloy. The surfaces were glass bead blasted and etched to remove any traces of the Mo foil release layers. The completed panel is shown in Figure 19. Its thickness was 0.056 inches thick, representing a 34 percent reduction from the as-sprayed foil thickness.

The tube package was machined to the configuration specified in the RPI sketch of Figure 20, and the center rod removed to yield the composite tube with diffusion bonded stainless steel grip sections at each end. The stainless steel end sections were masked with a stop-off lacquer, and the outer surface of the center section was glass bead blasted and etched. The completed tube is shown in Figure 21. The as-HIP'd tube I.D. was quite uniform, with all measurements in the range 1.056 to 1.057 inches. The as-machined O.D. of the stainless steel grip sections was 1.350 inches, and that of the composite center section approximately 1.175 inches. The outer layer of Waspaloy matrix material was irregular in texture and contained several shallow, extended grooves. It appeared that the outer Mo foil release layer had wrinkled during the HIP consolidation, and that the texture of the wrinkles was reproduced in the Waspaloy surface layer. A thin slice was cut from the longer grip end of the tube and prepared for metallographic examination. The microstructure is shown in Figure 22. The fiber distribution and ply-to-ply relationship are reasonably uniform. The 0.060-inch wide localized void seen in the matrix between fiber layers 2 and 3 is an anomaly related to the fact that the section was taken at the very end of the monotape layers. These ends are somewhat ragged and the occurance of a void or inclusion of some sort is not surprising. In subsequent processing, this void disappeared after removing less than 0.050 inches of the tube end.

After discussing the unexpected Waspaloy surface condition in a telecon with Dr. Bahei-El-Din, this first-of-a-kind composite tube (together with the completed panel) was shipped to RPI for their examination. In a subsequent telecon discussion between W. P. Blankenship and Dr. G. J. Dvorak of RPI, Dr. Dvorak expressed concern that some of the outer surface layer irregularities might act as crack initiation sites during mechanical testing. It was agreed that the tube would be returned to AES for evaluation of approaches to removing the subject irregularities.

Figure 19. Unreinforced Waspaloy Panel.

-32-

Design of the steel sleeve around the specimen

45° chamfer

specimen (1.25″ φ)

steel sleeve
(wall thickness = 0.05″)
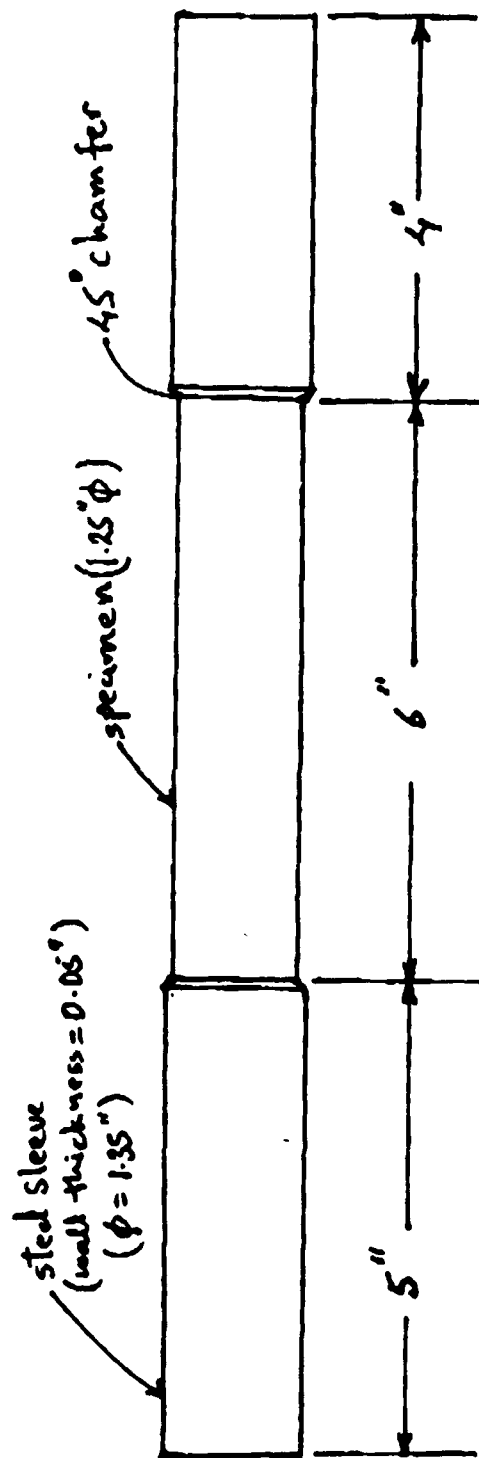(φ = 1.35″)

5″   6″   4″

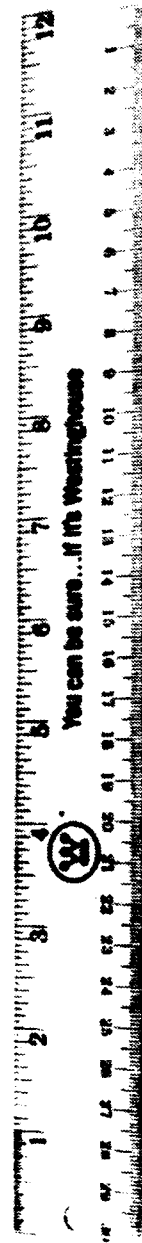Figure 20. Tube No. 1, Machining Specifications.
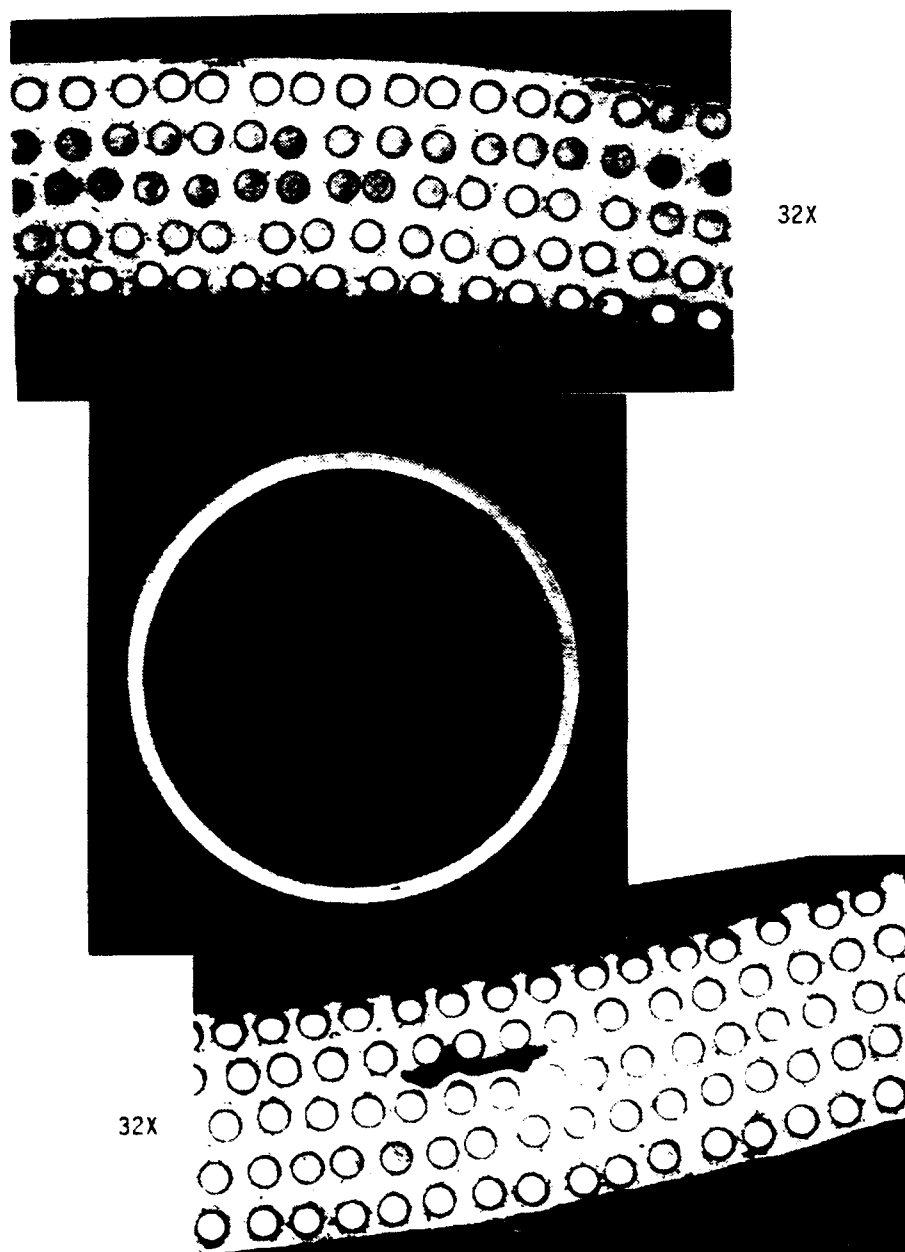
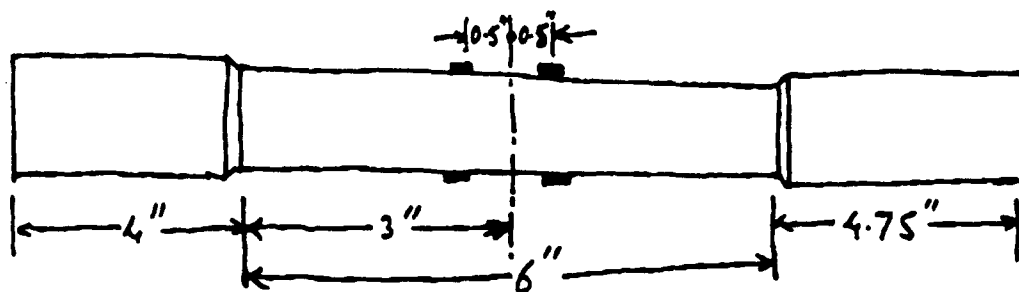Figure 21. Tube No. 1, As-Machined and Etched.

-34-

32X

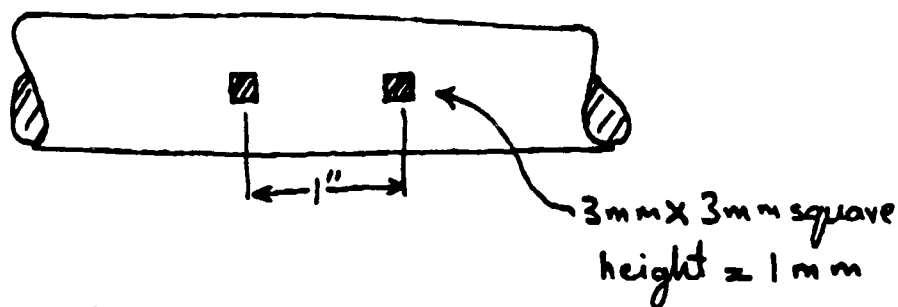32X

Figure 22.   Tube No. 1, Cross Section Microstructure.

-35-

Various ideas regarding the situation were discussed in telecons between
W. P. Blankenship and Drs. Bahei-El-Din and Himanshu Nigam of RPI. The
first implemented modification was the removal of the extended grooves in
the outer Waspaloy layer. This was accomplished by careful precision
machining to a uniform O.D. of 1.160 inches. The irregularities were
successfully removed, but nothing remained of the outer Waspaloy layer at
completion. This was judged by RPI to be unacceptable due to the risk of
crack initiation at the fiber/surface intersection during testing.
Various approaches were then explored for adding a new surface layer of
Waspaloy matrix material to the 6-inch long center section. In addition,
RPI asked that we propose a method of adding precisely located, integrally
bonded extensometer socket pads to the tube outer surface. The final
definition of these pads is shown in the RPI sketch of Figure 23.

A meeting was held at RPI between W. P. Blankenship and Dr. Bahei-El-Din
on May 24, 1991 to discuss options for reprocessing the tube. An approach
was agreed upon as described next. A multiple layer spiral wrap of
Waspaloy foil would be assembled onto the center section of the tube. The
thickness of the layers would be such that, after reencapsulation and a
second HIP cycle to consolidate this foil and diffusion bond it to the
existing tube surface, the socket pads could be machined directly into the
consolidated Waspaloy. A modified HIP cycle configuration would be used
in which, after the 20 minute hold at $2100^{\circ}F$ and 30,000 psi, the
pressure would be maintained at (or as close as possible to) the 30,000
psi level while the package was cooled. Depressurization would then be
performed at room temperature. (Theoretical considerations indicate that
this type of cycle configuration will result in minimizing the residual
internal stresses in the consolidated composite assembly.) Dr.
Bahei-El-Din agreed to consider the alternatives of whether the HIP cycle
pressure should be applied to both inner and outer package surfaces or to
the outer surface only. (In a later telecon, he advised us of his
preference for the inner/outer surface alternative.) It was also agreed
that the order scope would be expanded to include a second full length
tube, designed and constructed with incorporation of "lessons learned"
from the above experience. In this second tube, the additional outer
Waspaloy layers would be an integral part of the initial package assembly
and would extend over the full length of the composite tube.

Size of Tabs:

TOP VIEW

3mm x 3mm square
height ≈ 1mm

Side view

defect should
be placed away
from the tabs.

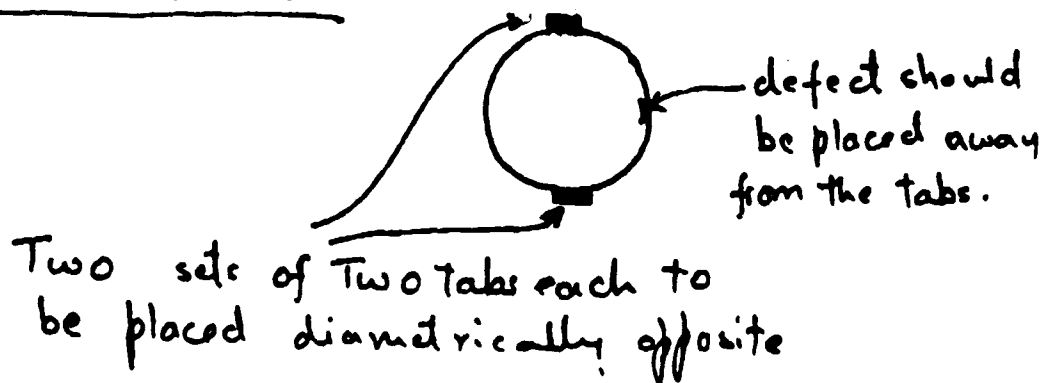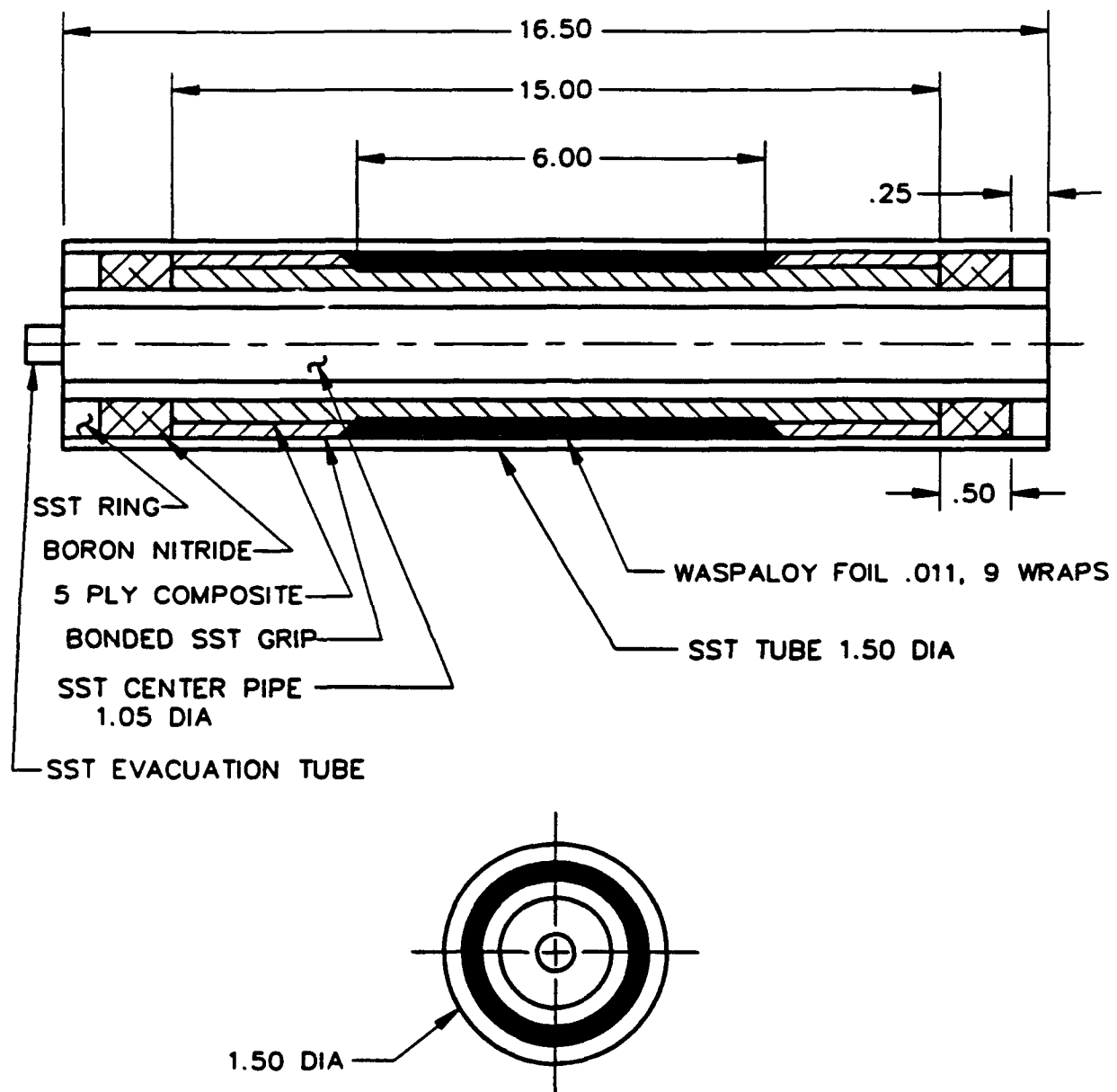Two side of Two Tabs each to
be placed diametrically opposite

Figure 23.   Tube No. 1, Extensometer Socket Pad Specifications.

The design of the HIP package for reprocessing Tube No. 1 is shown in Figure 24. The intent was that, following assembly and HIP consolidation, precision machining would remove the encapsulation and provide a consolidated outer layer of defect-free Waspaloy at least 0.005 inches thick, plus two sets of integral extensometer pads.

To supply matrix material for reprocessing Tube No. 1, a 0.011-inch thick sheet of Waspaloy foil was successfully arc sprayed and removed from the drum. This sheet was cut to a 37-inch length, with a width tapering from 6.000 inches at the starting end to 6.176 inches at the opposite end. It was assembled onto the composite tube as a 9-layer spiral wrap positioned between the stainless steel end grips. A few small resistance spot welds were used to keep the wraps tight and prevent unraveling. The final diameter of the wrapped section was 1.365 inches. This assembly fitted snugly into the 1.370 inch I.D. of the outer stainless steel tube of the HIP package. The inner stainless steel pipe was machined to a 1.045 inch O.D. and then sent to a vendor for plasma spraying its outer surface with a Mo release layer. After coating with Y_2O_3, the final O.D. was 1.051 inches. The inner tube was then inserted into the 1.056 inch I.D. of the composite tube. Installation of boron nitride and stainless steel end rings and the evacuation tube completed the HIP package assembly.

After welding the end closures, the package was evacuated and outgassed at 550°F. It was successfully leak tested and the evacuation tube sealed off. The package was loaded vertically in the vendor's HIP unit (together with Tube No. 2, as described in the next section) and consolidated in the special 2100°F - 30,00 psi - 20 minute HIP cycle. The parametric configuration of this special cycle is shown in Figures 25a and 25b, and the as-HIP'd package is shown in Figure 26. As seen in the photograph, the outer stainless steel tube was severely buckled along the length of the center section. (A similar but less severe buckling had occurred on the opposite side from that shown.) It was immediately obvious from this buckled condition that the amount of compaction required to consolidate the nine-layer wrap of unreinforced Waspaloy had been more than this HIP package design could tolerate.

16.50

15.00

6.00

.25

.50

SST RING
BORON NITRIDE
5 PLY COMPOSITE
BONDED SST GRIP
SST CENTER PIPE
1.05 DIA
SST EVACUATION TUBE

WASPALOY FOIL .011, 9 WRAPS

SST TUBE 1.50 DIA

1.50 DIA

FC20103-02
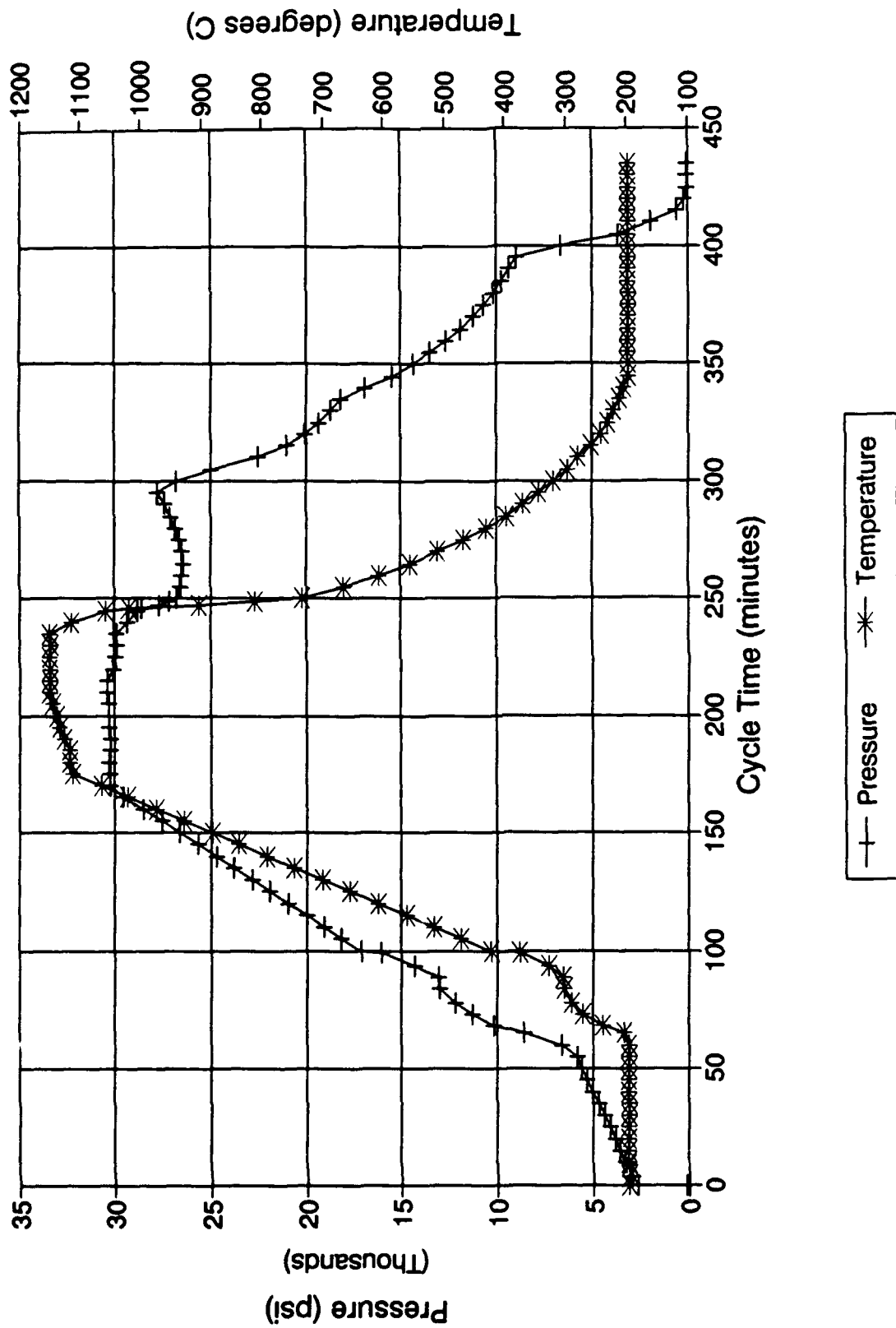
Figure 24.   Tube No. 1, Second HIP Package Schematic.

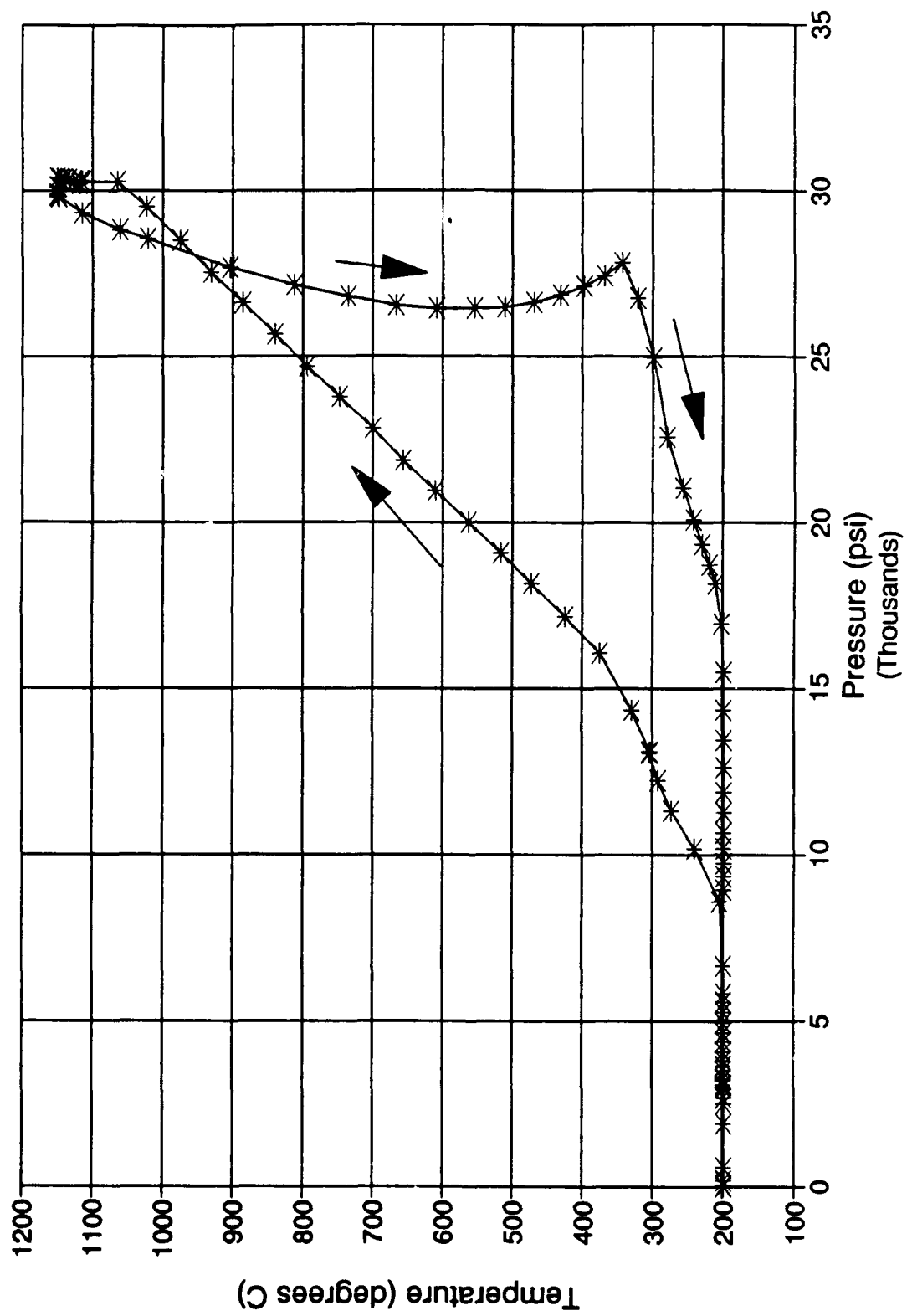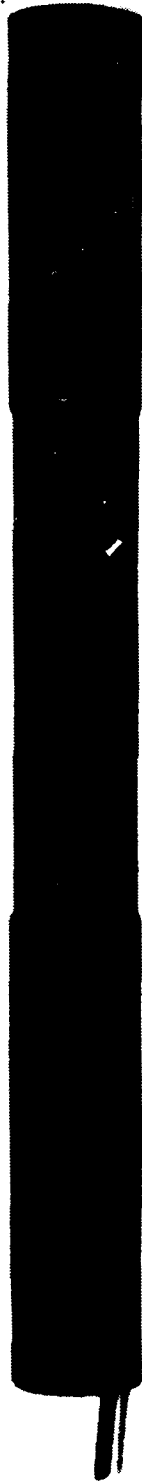Figure 25a. Tube No. 1, Second HIP Cycle Pressure/Temperature vs. Time.

-40-

Figure 25b. Tube No. 1, Second HIP Cycle Temperature vs. Pressure.

-41-

Figure 26.   Tube No. 1 Second HIP Package, As-Consolidated.

Machining was initiated to bring the tube to the configuration shown previously in Figure 23. The O.D. was turned to 1.350 inches to reestablish the stainless steel grip dimension. Then the locations of the extensometer socket pads and the grip section inboard end chamfers were layed out, and machining of these features initiated. Machining proceeded in 0.005-inch diametral increments, with a target diameter of 1.170 inches; based on the as-assembled diameter of 1.160 inches, this would provide a 0.005-inch thick outer layer of Waspaloy covering the outermost layer of fibers. However, when machining the region between the short grip end and the adjacent pad precursor ring, reinforcing fiber was exposed at a diameter of 1.182 inches. Similarly, in the region between the two pad precursor rings, fiber was exposed at a diameter of 1.206 inches. Machining was terminated at this point. The overall package appearance at this stage is shown in Figure 27, and a closeup of one exposed fiber region is shown in Figure 28. The application of HIP pressure to the package I.D. had obviously expanded the composite outward along the center section between the original grips, with the amount of expansion increasing toward the midpoint of this section. This is illustrated more quantitatively in Figure 29. It was concluded with hindsight that a better approach to reprocessing Tube No. 1 would have been to apply HIP pressure to the outer surfaces only.

It was decided that the tube would be reworked by plasma spraying a layer of nickel base superalloy onto the regions between the pad precursor rings and the grips, and then machining the plasma-sprayed layer to a conservative final diameter. Dr. Nigam was advised of this decision in a telecon with W. P. Blankenship. Waspaloy is not commercially available as a plasma spray powder, so METCO 461, a standard plasma spray alloy of composition $Ni-17.5Cr-5.5Al-2.5Co-0.5Y_2O_3$, was selected. This alloy is a good thermal expansion match with Waspaloy (coefficient of thermal expansion of 13×10^{-6} $°C^{-1}$, cf. 12.2×10^{-6} for Waspaloy), and has good oxidation resistance to 1800°F. The grips, pad precursor rings and tube center section were masked off, and spraying performed by a local vendor. The plasma sprayed regions were then machined to a diameter of 1.220 inches, and the pads milled to their final 3mm x 3mm x 1mm high dimensions. The center stainless steel tube was then removed, completing the fabrication process. The final appearance of Tube No. 1 is shown in Figure 30, and a closeup of the center section is shown in Figure 31.
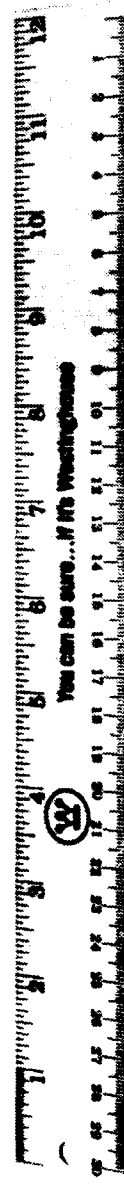
Figure 27. Tube No. 1 HIP Package, Partially Machined.

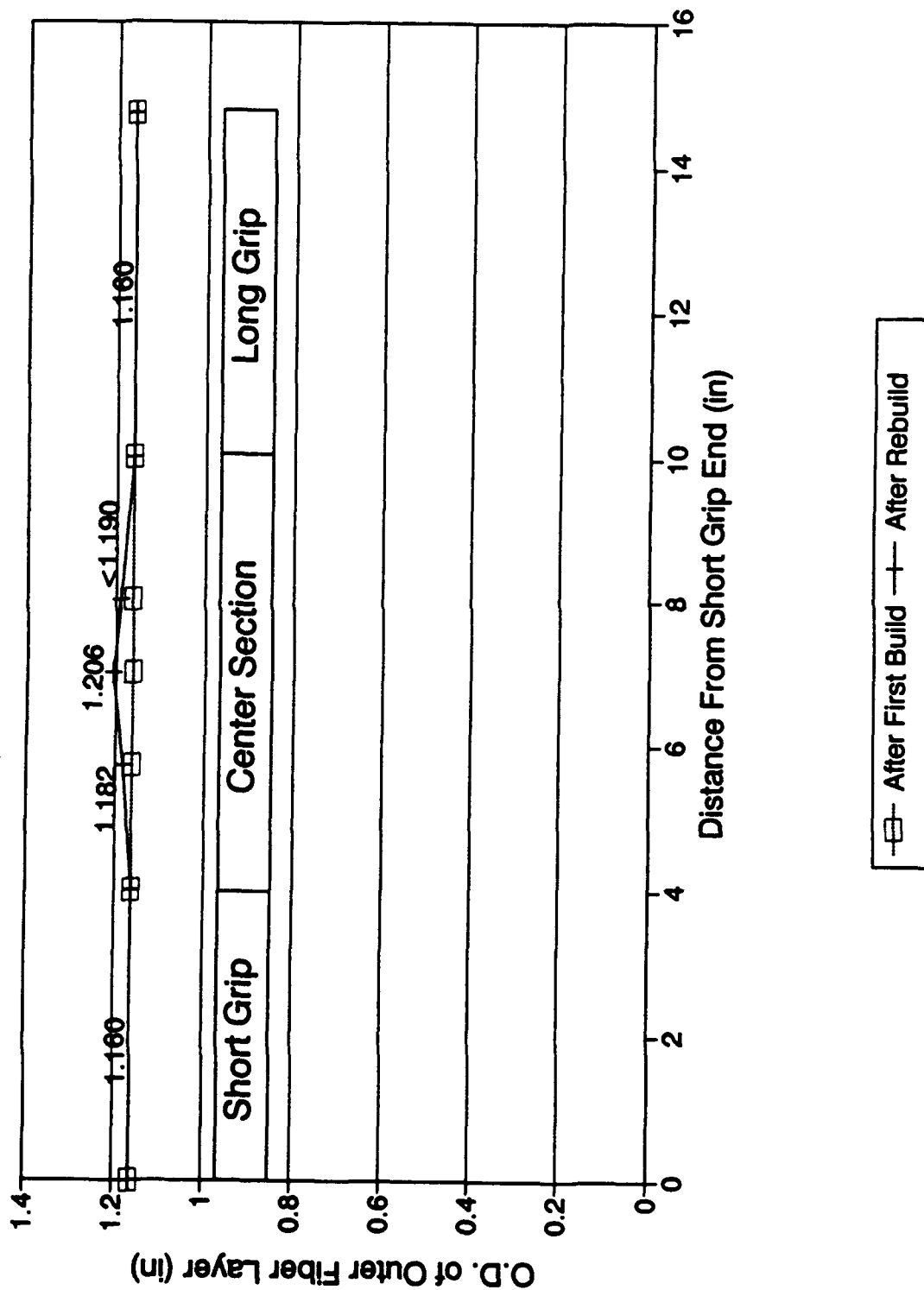Figure 28. Tube No. 1, Reinforcing Fibers Exposed During Machining.

-45-

Figure 29. Tube No. 1, Outer Diameter Profile of Outer Fiber Layer Before and After Second HIP Cycle.
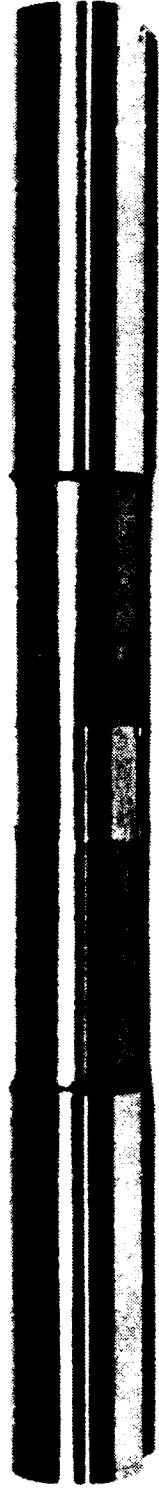
Figure 30. Tube No. 1, After Final Machining.

-47-

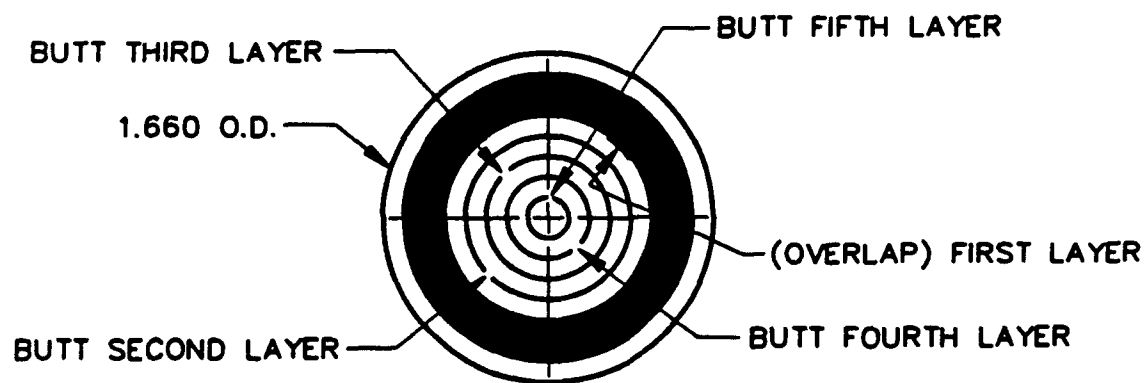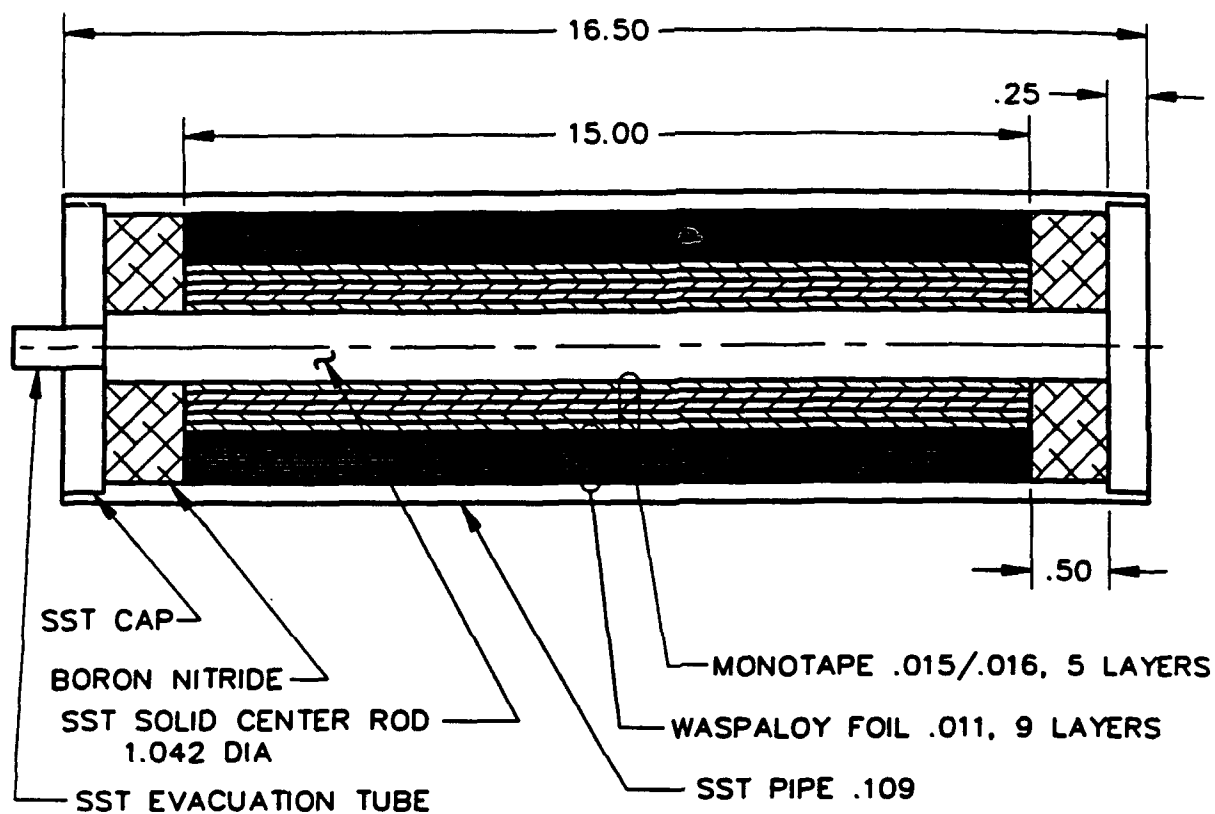Figure 31. Tube No. 1, Center Section After Final Machining.

The completed tube was shipped to RPI on July 30, 1991. A meeting was held at RPI on August 6, 1991 between W. P. Blankenship and Drs. Bahei-El-Din and Nigam, in which the reprocessing of Tube No. 1 was discussed in some detail. It was agreed that machining of Tube No. 2, discussed in the next section, would not be initiated until Dr. Dvorak had been briefed on the status of the work.

Design and Fabrication of Tube No. 2

The design of the HIP package for Tube No. 2 is shown in Figure 32. In addition to the 5 monotape layers, 9 outer layers of 0.011-inch Waspaloy foil were incorporated to provide material for the extensometer socket pads. Since O.D. machining of the entire tube length would inevitably be required, no release layer was used between the Waspaloy foil and the outer stainless steel pipe. As before, the package was assembled from the outer layer inward. The stainless steel center rod O.D. was machined to fit the assembly, plasma sprayed with Mo, turned to a final O.D. of 1.042 inches and coated with Y_2O_3. It was mated with the innermost monotape layer and the two inserted as a subassembly to avoid scraping off the Y_2O_3 coating. Installation of the boron nitride rings, stainless steel end discs and the evacuation tube completed the assembly. After welding the end closures, the package was evacuated and outgassed at 550°F. It was then successfully leak tested and sealed off.

The package was loaded (together with that for Tube No. 1, described in the previous section) vertically in a vendor's autoclave and processed in a specially configured 2100°F - 30,000 psi - 20 minute HIP cycle. The parametric configuration of this cycle was shown previously in Figures 25a and 25b. The as-HIP'd package is shown in Figure 33. As seen in this figure, the outer pipe was severely buckled along the entire length of the package.

Figure 32. Tube No. 2, HIP Package Schematic.

16.50

15.00

.25

.50

SST CAP

BORON NITRIDE

SST SOLID CENTER ROD
1.042 DIA

SST EVACUATION TUBE

MONOTAPE .015/.016, 5 LAYERS

WASPALOY FOIL .011, 9 LAYERS

SST PIPE .109

BUTT THIRD LAYER

BUTT FIFTH LAYER

1.660 O.D.

(OVERLAP) FIRST LAYER

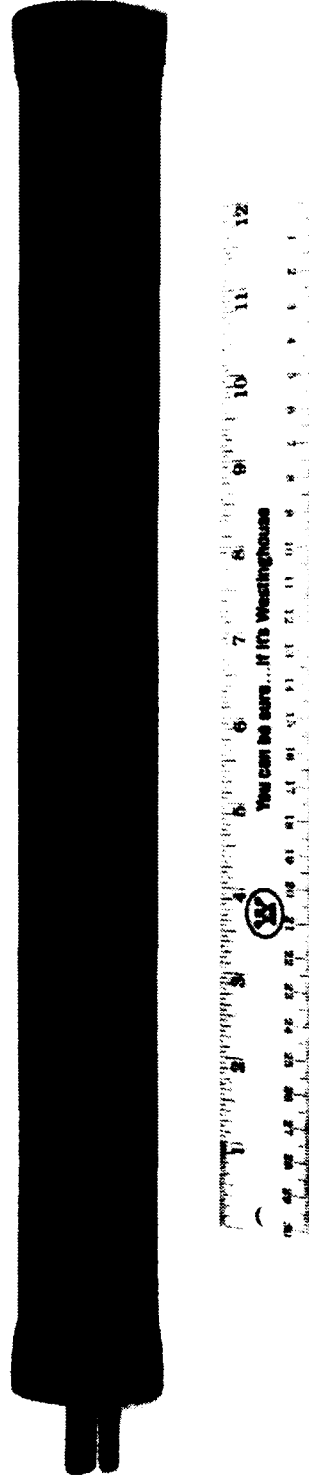BUTT SECOND LAYER

BUTT FOURTH LAYER

FC20103-03

Figure 33. Tube No. 2 HIP Package, As-Consolidated.

In a telecon between W. P. Blankenship and Dr. Nigam, approval was given to machine Tube No. 2 to essentially the same configuration as Tube No. 1. Machining of the package was initiated by turning to the 1.350-inch grip diameter over its entire length. Machining inboard of the grips then proceeded with the removal of 0.005-inch layers, with a target final diameter of 1.170 inches. However, localized exposure of the outer layer of fibers occurred at a diameter of 1.182 inches on the short grip end and 1.178 inches on the long grip end of the center section. Machining of the tube O.D. was terminated at this point. After completion of milling of the extensometer socket pads, the center rod was removed to complete the composite tube decladding process. A thin slice was removed from one end of the tube, mounted and polished for metallographic examination. The microstructure is shown in Figure 34. It is obvious from this photograph that the HIP package buckling produced severe distortion of the composite structure at Locations A and C. Some less severe distortion is also seen at Locations B and D. The area at which some outer fibers were exposed during the final machining pass undoubtedly corresponds to either Location A or C. As was the case with Tube No. 1, it is obvious from the buckled condition of the HIP package and resultant distortion of the composite structure that the amount of compaction required to consolidate the nine-layer wrap of unreinforced Waspaloy was more than this HIP package design could tolerate.

The appearance of Tube No. 2 was discussed in a telecon between W. P. Blankenship and Dr. Nigam, and it was agreed that the tube would be shipped to RPI for examination. This was done, and resulted in a request from RPI that the tube be plasma sprayed with a thin layer of METCO 461 to cover the exposed fibers. The tube was returned to AES and the plasma spraying performed by a local vendor. After spraying, it was found that a slight bend had developed near one end of the center section. Most of this effect was removed by adjusting the setup of the tube in the lathe prior to final machining. The as-sprayed appearance of the tube center section is shown in Figure 35. Final machining and polishing was then performed to yield a 0.010-inch METCO 461 layer thickness and a final center section O.D. of 1.190 inches. The completed tube is shown in Figure 36. Tube No. 2 was shipped to RPI on September 23, 1991, completing the requirements of the original order and subsequent modifications.
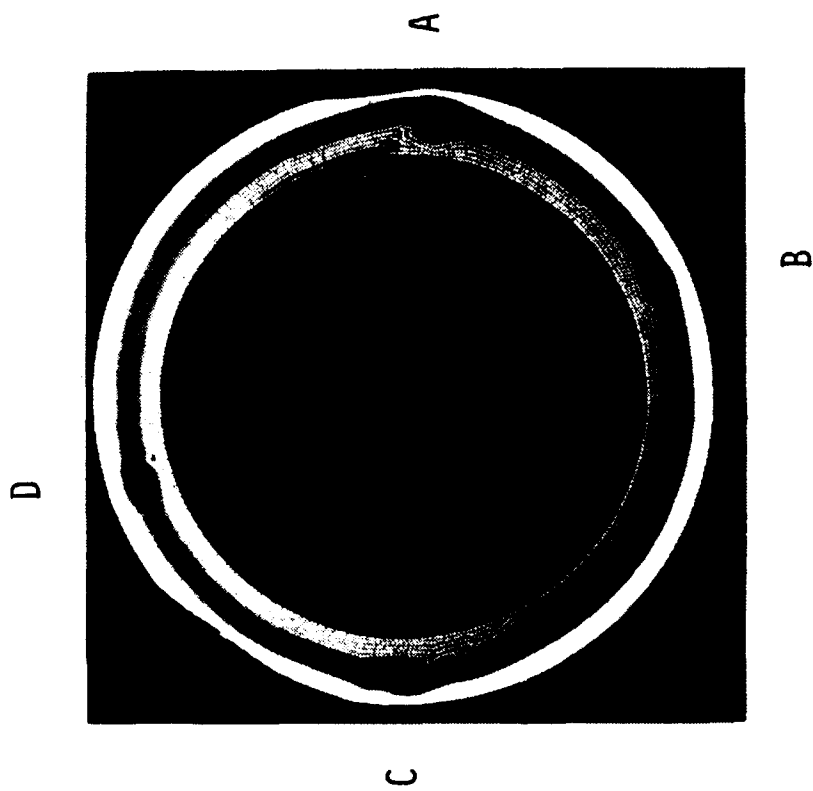
Figure 34. Tube No. 2, Cross Section Microstructural Details.

-53-

Figure 35. Tube No. 2, As Sprayed with METCO 461 Alloy

-54-

Figure 36. Tube No. 2, After Final Machining.

-55-

Conclusions

1. A method was developed for fabricating 4- or 5-ply tungsten-fiber-reinforced Waspaloy-matrix tubes up to 15 inches in length. A fiber diameter of 0.006 inches and fiber volume fraction of 0.35 were successfully incorporated. Key features of the method include:

   o Using a solid rod as the center member of the HIP package, thus constraining application of the HIP cycle pressure to the package outer surfaces only.

   o Using sprayed coatings of HIP package release layers rather than separate layers of foil.

   o Limiting the thickness of the unreinforced outer layer of Waspaloy matrix material in the HIP package to 0.010 inches or less.

2. While a reasonably uniform composite structure was obtained using a multilayer assembly of butt-jointed plies, some perturbations in the structure at the butt joint locations are probably inevitable.

3. Serious difficulties were encountered in attempting to add integrally consolidated and bonded Waspaloy extensometer socket pads to the outer surfaces of the composite tubes. Both of the approaches attempted resulted in moderate to severe distortion of the composite structure and/or the tube geometry.

4. Some of the problems resulting from the above distortions were successfully mitigated by plasma spraying the composite tube with a layer of the oxidation resistant superalloy METCO 461.

5. One 4-ply and one 5-ply sublength prototype and two 15-inch long 5-ply tubes were fabricated, together with a flat panel of unreinforced Waspaloy, and delivered to RPI.

Recommendations

1. Order at least one additional 15-inch tube to be fabricated without the additional outer layers of Waspaloy foil.

2. Investigate alternative approaches to adding extensometer socket pads to the tube outer surface. Possibilities include machining the pads from a diffusion bonded HIP package outer pipe, attaching separately machined pads by resistance spot welding, and machining the pads from METCO 461 (or similar) alloy plasma sprayed onto the tube surface after tube fabrication is complete. These approaches should be investigated on relatively inexpensive subscale models prior to committing one of them to a full size composite tube.

3. If possible, make future composite tubes longer than the final required size to permit sectioning for metallographic examination well inboard of the ends of the composite plies.